The Pennsylvania State University

The Graduate School

RESONANT ULTRASOUND SPECTROSCOPY FOR QUALITY CONTROL OF GEOMETRICALLY COMPLEX ADDITIVELY MANUFACTURED COMPONENTS

A Thesis in

Engineering Science and Mechanics

by

Samantha McGuigan

Submitted in Partial Fulfillment

of the Requirements

for the Degree of

Master of Science

August 2020

The thesis of Samantha McGuigan was reviewed and approved by the following:

Andrea P. Arguelles
Professor of Engineering Science and Mechanics
Thesis Co-Adviser

Parisa Shokouhi
Professor of Engineering Science and Mechanics
Thesis Co-Adviser

Jacques Riviere
Professor of Engineering Science and Mechanics

Judith B. Todd
P.B. Breneman Department Chair
Head of the Department of Engineering Science and Mechanics

ABSTRACT

Metal additive manufacturing (AM) has started to overshadow traditional manufacturing practices thanks to its ability to produce complex, high-performance and application-customized components. However, AM process parameters have not been optimized, leading to inconsistencies and imperfections such as cracks and pores in parts, as well as deviations from the original design. Nondestructive evaluation (NDE) methods used for part qualification such as x-ray computed tomography (CT) and conventional ultrasonic testing (UT) have limitations in their abilities. X-ray CT is costly, hazardous, and offers limited resolution for larger components while many UT methods have limited applicability for inspection of parts with complex geometries or rough surfaces. Here, we conduct an integrated numerical and experimental study to investigate the feasibility of resonance ultrasound spectroscopy (RUS) as an alternative NDE method to inspect complex AM lattice structures with a varying number of missing struts. The most encouraging results are obtained when test samples have traction-free boundary conditions. The results of numerical simulations including *eigenfrequency* and *frequency domain* analyses are promising, indicating that the pristine and defective lattice samples should theoretically be distinguishable. In addition, given a reference intact sample, characterizing the extent of the defect in terms of the number of missing struts appears feasible. We introduce a similarity metric to compare the spectra after being locally normalized. However, the experimental results are not as conclusive. Although pristine and defective lattices may be distinguished for some cases, the number of missing struts cannot be inferred. The discrepancies between the numerical and experimental results are likely due to our simplified assumptions about material properties in numerical simulations and/or the presence of other unaccounted defects and heterogeneities in test samples.

TABLE OF CONTENTS

LIST OF FIGURES

LIST OF TABLES

ACKNOWLEDGEMENTS

I would first like to thank my advisers, Dr. Arguelles and Dr. Shokouhi, for all the encouragement and support that they have provided for me during my time as a graduate student. I would also like to the students and faculty of PennSUL for everything that they have provided on a day-to-day basis. I appreciate the small things that you have all done for me, especially when it was time consuming or something that was not necessarily at the top of your to-do list. I finally want to thank my family and friends. All your love and encouragement has not gone unnoticed, and without all of you, I do not know if I would have been able to complete this degree. Without all of the people who have been a part of my life during these two years, I would not have learned or experienced all the challenges that have made me the person that I am today, and so I thank you all.

Thank you to the National Institute of Standards and Technology (NIST) for providing funding for this study (Award No. 70NANB19H091), as well as the samples used. The work presented here does not necessarily represent the views of NIST.

DEDICATION

Although you do not want any recognition at all for your love and support, I want to dedicate this thesis to you, Andrew. You sacrificed so much for me while I was in graduate school, and I truly will never be able to repay you.

CHAPTER 1 INTRODUCTION

Metal additive manufacturing (AM) is becoming increasingly popular because of providing the possibility to produce complex, high-performance, and application-customized components that could not be made using traditional manufacturing. However, as-built properties may deviate from the design values due to variations in feedstock material, processing parameters, and post-processing techniques limiting the adoption of additively manufactured parts in many industries [1-2]. Inconsistencies in properties may lead to premature failure if they are not identified during the quality control stage. The recognized uncertainty in the quality of AM parts [3] has led to an increased interest in nondestructive testing (NDT) methods for part qualification.

Generally speaking, the choice of NDT technique and acceptance criteria depends on part size and complexity, surface roughness, type and length scale of the expected defects as well as access to inspection surfaces [1]. For example, x-ray computed tomography (CT) is primarily used to detect voids/porosity in AM parts, but the detectability of these defects is highly dependent on the size of the specimen and the specs of the test apparatus. Therefore, radiography and CT techniques do not always reveal small pores or microcracks [4]. Penetrant testing can detect surface-breaking flaws, but relies on a relatively smooth sample surface, which for most AM processes would require additional post-process machining [5-6]. Similarly, Eddy current testing can be used to identify small and shallow surface cracks, but careful calibration is required which challenges widespread implementation [4-6]. Magnetic testing is also sensitive to surface discontinuities, as well as near-surface grain size and structure, but must be combined with visual inspection to locate defects [4,7]. Thermography is relatively fast, non-contact, and able to inspect large surface areas, but can only detect geometric and material discontinuities within depths of a few millimeters [5,8]. Ultrasonic testing (UT) is sensitive to localized defects and material

properties at depths reaching a few centimeters [5,6]. However, more technological advances are necessary to overcome UT shortcomings related to material anisotropy and complex geometries [4,6,8].

Here, we investigate the feasibility of resonance ultrasound spectroscopy (RUS) for inspection of AM components having very complex geometries. RUS is an attractive technique for inspecting AM parts because it is inexpensive and provides rapid results. This method relies on measuring the fundamental (resonance or modal) frequencies of a sample following a mechanical excitation; because the entire sample is probed in a single measurement at lower frequencies, this technique is suitable for parts of complex geometries, independent of surface finish. However, the sensitivity of this method to the presence of localized defects is not well studied.

Traditionally, RUS is used for materials characterization i.e., to nondestructively measure the elastic tensor of a sample [9,10]. When using RUS to extract elastic constants, mode identification is a crucial step which involves accounting for missing or overlapping resonance frequency peaks [11]. With simple geometries, the experimental response can be compared to analytical formulation to accurately identify the modal frequencies [12]. As geometric complexity increases, more advanced approaches are necessary. Liu and Maynard [13] propose using the finite element method (FEM) to determine resonance frequencies of arbitrarily shaped samples. Chen et al. [14] report a data fusion method based on Bayesian formulation and the Reversible-jump Markov chain Monte Carlo (RJ-MCMC) algorithm to identify missing, overlapping, and/or shifting frequencies. A second factor that influences the ability to accurately identify resonant peaks is material damping. Attenuative materials having low Q-factors result in broad and overlapping resonant peaks [15]. Although difficult, elastic constants have successfully been

identified for materials such as enamel (a biological tissue material) [16,17], wood [18], saturated porous ceramic [19], $(GeTe)_mSb_2Te_3$ alloys [20], SiC-SiC composite tubular specimen [21], high density U_3Si_2 [22], materials for super conductors like Sr_2RuO_4 [23], rare-earth scandates ($SmScO_3$, $TbScO_3$, and $DyScO_3$) [24], and relaxor-based single crystals [25]. Techniques such as Empirical Mode Decomposition (EMD) by Zhang et al. [15] have been used to identify resonance peaks in cortical bone (a low Q-factor material) with improved repeatability. Finally, for heterogeneous materials, it can be difficult to relate anisotropic elastic properties to the microstructure of the material [26]. Latypov et al. [26] propose a framework for multiscale forward modeling of RUS for heterogeneous materials.

Once the eigenfrequencies are adequately identified, an inverse problem must be solved to find the elastic constants. Modified optimization procedures such as the fixed point iteration method can be used to solve the inverse problem in a timely manner by requiring that only the few lowest eigenfrequencies to be known [27].

For specimens of known geometry and elastic constants, RUS can be used in tandem with FEM to detect and localize defects [11]. Flynn and Radovic [28] compare the spectra of undamaged and damaged samples to identify trends in the frequency shifts with respect to defect depth and location. They compare the spectra for 12 samples before and after adding notches at prescribed locations. Their method combines a numerical and experimental approach that yields defect locations with an average error about 5% of specimen length and gives defect depths with an average error around 2% of specimen thickness [28]. However, the defects characterized in their study were on the order of 0.67 – 2.35 mm, which is significantly larger than AM relevant defects, such as pores, which are typically on the order of 100 microns [30].

In the AM realm, Ibrahim et al. [31] perform impact-based acoustic resonance (AR) testing, quasi-static compression tests, and three-point bend tests together with FEM on AM lattice structures and compare the *effective* [32] elastic moduli from each testing modality to test the applicability of AR testing for characterizing the lattice samples. The elastic moduli attained from the experimental AR testing calculated following ASTM E 1876-99 are found to be higher than those from the FEM simulations. They attribute this discrepancy to the presence of loosely bonded powder increasing the stiffness of the lattices [31]. Garlea et al.[33] study the effect of porosity on the resonant response of samples manufactured using powder bed fusion. They report the experimental results for two different samples, a disk and a cylinder, within the same build and built using the same parameters. RUS is performed on the disk to determine the elastic moduli and x-ray computer micro-tomography is performed on the cylinder to estimate the porosity. They correlate an increase in porosity from 0.106% to 0.476% with a 15% drop in the elastic moduli. In addition, they report resonance peak splitting and separation when porosity is unevenly distributed [33]. Although the results are promising, the validation relies on comparisons of results obtained from different samples from the same build plate; however, literature [34–38] suggests two samples from the same build plate may have different porosities undermining the validity of the reported results.

In another study, Todd et al. [39] investigate whether the shift in resonance frequencies can be utilized to predict the mechanical properties of Ti-6Al-4V AM parts. Resonant frequency measurements are performed on the as-built part, and then repeated after the parts are annealed. Afterwards, 15 of the samples are machined and tensile tested according to ASTM E8 by an outside company. The mechanical properties of interest are estimated from the resonance frequencies using different types of linear regression models. They conclude that the models predicting the

ultimate tensile strength (UTS) have the least error of all the multiple linear regressions, however, the models are less accurate in predicting Young's modulus [39]. They found little or no correlations between resonance frequencies measurements and yield strength, elongation or reduction in an area at failure [39].

Despite the potential advantages of RUS as an NDT tool, there are limited published efforts using RUS for AM part qualification. The aforementioned studies are limited in the geometries used [12–14,28,31] and in the validation strategies [31,33]. The objective of this work is to investigate the feasibility of RUS as a reliable technique for detecting macroscopic defects in AM parts of complex geometries, namely, lattice structures. Defects are introduced by removing strut elements from the lattice one at a time in order to establish a threshold for minimum detectable damage. Our approach combines experimental testing with systematic FEM simulation using COMSOL Multiphysics® 5.4 and 5.5 commercial FEA software. The novelty of this study lies in quantifying the defect detectability threshold when RUS is applied to AM samples with complex geometries. The long-term goal is to establish RUS as an economic quality control/assurance tool for AM parts.

CHAPTER 2 THEORETICAL FOUNDATION

Resonance ultrasound spectroscopy (RUS) is a resonance-based ultrasonic technique typically used to characterize elastic properties of solids. This method relies on measuring resonance frequencies and Q-factors of a sample corresponding to a number of free vibrational modes. Given the dependency of resonance frequencies on geometry, size, and material properties, a single measurement may be sufficient to calculate the elastic constants of the material [40]. In this section, we provide a brief theoretical description of RUS.

Recall the linearized strain-displacement relationship for a three-dimensional elastic solid:

$$\epsilon_{ij} \equiv \frac{1}{2}\left(\frac{\partial \psi_i}{\partial x_j} + \frac{\partial \psi_j}{\partial x_i}\right) \tag{1}$$

with ϵ_{ij} being the infinitesimal strain tensor and ψ being the displacement vector [40,41]. In this notation, indices I = 1,2,3 indicate the three orthogonal coordinate directions, respectively. RUS assumes a linear elastic constitutive relation (Hooke's law) for the constituent material written as,

$$\sigma_{ij} = c_{ijkl}\,\epsilon_{kl} \tag{2}$$

where σ_{ij} denotes the stress tensor and c_{ijkl} defines the elastic tensor. Although the elastic tensor can have as many as 81 elastic constants, only 21 are independent considering the symmetries of stress and strain tensor as well as energy considerations. Newton's second law of motion can be written as:

$$\frac{\partial \sigma_{ij}}{\partial x_j} = \rho \frac{\partial^2 \psi_i}{\partial t^2}. \tag{3}$$

which represents the elastic wave equation, where ρ is the mass density and t is time.

The *forward problem* (calculating the resonance frequencies based on elastic constants) involves finding the solutions to equations (2) and (3) assuming traction-free boundary conditions on the surface of the sample:

$$\sigma_{ij} n_j = 0 \tag{4}$$

where n_j are the components of the normal unit vector. A harmonic solution in the form of $\cos(\omega t + \phi)$ yields separate and distinct ω_n, which are the resonance frequencies.

The displacement field ψ_i that satisfies equations (2), (3), and (4) should also minimize the integral:

$$L = \int\int\int \left(\rho\omega^2 \psi_i \psi_i - c_{ijkl}\, \epsilon_{ij}\, \epsilon_{kl}\right) dV. \tag{5}$$

The Rayleigh-Ritz method is often used to find solutions that minimize L. In this method, the displacement field in (4) is expanded in some basis such as:

$$\psi_i = \sum_{p=1}^{N} a_{pi} \Phi_p. \tag{6}$$

Where a_{pi} are the expansion coefficients and Φ_p are the basis functions chosen based upon the shape of the sample [41]. Substituting (6) into equation (5), L can be rewritten as:

$$L = \left(\omega^2 E_{piqj} - \Gamma_{piqj}\right) a_{pi} a_{qi}. \tag{7}$$

E_{piqj} is a tensor corresponding to the kinetic energy terms [42], defined as:

$$E_{piqj} = \delta_{ij} \int\int\int \left(\rho \Phi_p \Phi_q\right) dV \tag{8}$$

With δ_{ij} being the Kronecker delta, and Γ_{piqj} is a tensor corresponding to the elastic energy terms [42] defined as:

$$\Gamma_{piqj} = \int\int\int c_{ijkl} \frac{\partial \Phi_p}{\partial x_k} \frac{\partial \Phi_q}{\partial x_l} \, dV \tag{9}$$

Minimizing L with respect to a_{pi} results in the following eigenvalue problem:

$$\Gamma_{piqj} a_{qj} = \omega^2 E_{piqj} a_{qj} \tag{10}$$

The solution to this eigenvalue problem in 3D will give 3N eigenvalues ${\omega_n}^2$ (equivalent to 3N resonance frequencies $f_n = \omega_n/2\pi$) and 3N eigenvectors $\left(a_{qj}\right)_n$, where N is the number of basis functions.

To find the elastic constants for a sample of a given geometry from the measured resonance frequencies, the *inverse problem* needs to be solved. In other words, one needs to find a set of independent elastic constants that best fit the measured vibrational response including the resonance frequencies and Q-factors. Formally, an optimization problem needs to be solved to minimize the following function [43] that describe the "distance" between the calculated and measured resonance frequencies:

$$F = \sum_{i=1}^{N} w_i (f_i - g_i)^2 \tag{11}$$

where f_i and g_i are the calculated and measured resonance frequencies, respectively, and w_i correspond to the weighting factors. The weighting factor is dependent on the confidence of the measured frequencies [42]. To ensure fast convergence, the initial values for elastic constants should be as close to the actual elastic constants as possible.

To solve the optimization problem, an iterative approach utilizing the Levenberg-Marquardt scheme [44] has been developed [43]. To implement this method, the function in equation (11) $F(x)$ is first expanded in a Taylor series of the general form:

$$F(x) = F(x_0) + (x - x_0)_\alpha F_{,\alpha}(x_0) + \frac{1}{2}(x - x_0)_\alpha F_{,\alpha\beta}(x - x_0)_\beta + \cdots \tag{12}$$

where x is the vector whose components $\{x_\alpha\}$ ($\alpha = 1,2, \ldots M$) are the parameters that need to be estimated; in this case, the elastic constants. For $F(x)$ to have a minimum at x, the derivative of equation (12) with respect to each set of parameters x_α should be set to zero, arriving at a set of M equations:

$$F_{,\alpha}(x_0) + F_{,\alpha\beta}(x_0)(x - x_0)_\beta = 0. \tag{13}$$

In this equation, comma indicates a (partial) derivative. Solving for x_α leads to

$$x_\alpha = x_{0\alpha} - {A_{\alpha\beta}}^{-1} B_\beta \tag{14}$$

where A and B are matrices whose elements are the derivatives found in equation (13). Given a set of current parameters, solving equation (14) gives an updated set of parameters, which will give a better fit between the measured and calculated frequencies [41]. The new parameters are then plugged into equation (8) to iteratively solve the inverse problem. One of the main sources of error that can occur when solving the inverse problem is not identifying one or more resonance modes in the measured vibrational response. To minimize the likelihood of missing a mode, it is useful to measure resonance frequencies while holding the sample at different orientations during testing [41].

The work presented in this thesis is entirely based around the forward problem and does not include solving the related inverse problem. Samples of known geometries with built-in defects (in the form of missing struts) are used for both experiments and numerical simulations. The goal

of this research is to identify how defect-induced differences in geometry will affect the resonance frequencies from the calculated (numerically simulated) and measure resonance frequencies. We assume a set of material constants for numerical simulations and also assume the only differences between the physical samples is the number and location of missing struts and engravings.

CHAPTER 3 FREE-FREE RESONANCE ULTRASOUND SPECTROSCOPY

This chapter investigates the suitability of an experimental configuration that employs a free-free boundary condition (BC) to identify the eigenfrequencies of lattices with a varying number of missing struts. Samples are first numerically simulated to determine the effects of missing lattice struts and engravings on resonance frequencies. The physical samples are then tested five times to determine repeatability and to validate numerical simulations. Finally, results are interpreted to determine whether a free-free BC is suitable for resonance frequency testing of lattice samples.

3.2 NUMERICAL SIMULATIONS

A series of numerical simulations are carried out to investigate the feasibility of RUS for identifying defects in complex lattice structures. To that end, the multi-modal vibrational response of a pristine lattice is simulated and compared against the responses of lattices with an increasing number of missing struts. In addition, we evaluate how numbers engraved on the lattices - used by the manufacturer for sample tracking - influence the vibrational response. The simulation results are used to guide the test configuration and parameter selection for RUS experiments.

3.2.1 NUMERICAL MODEL AND ANALYSES

The numerical simulations are conducted using COMSOL Multiphysics® [45] 5.4 and 5.5, a finite element software. For each simulation, the sample geometry is imported from a SolidWorks model into COMSOL. The CAD models are provided by the sample manufacturer (NIST) and adjusted to match the dimensions of the physical sample. More specifically, the total height is reduced to account for the machining of the sample off the build plate after printing. A discontinuity in the SolidWorks files is also corrected prior to generating the finite element mesh. Geometries with missing struts are created by manually removing the strut(s) from the reference pristine lattice

geometry in SolidWorks. We consider seven basic models with zero (pristine), one, two, four, six, eight, and twelve *external* missing struts, each with and without the engraved sample number. The CAD models differ only from the physical lattices with eight and twelve missing struts, which contain both *external* and *internal* missing struts, as shown in Sec. 3.3.1. The pristine sample is modeled with three different engravings corresponding to the three intact physical specimens.

The mesh is automatically generated using the 'physics-controlled mesh' option in COMSOL. The 'fine' mesh option is chosen after completing a sensitivity analysis comparing the resonance frequencies for decreasingly small mesh sizes. Errors in resonance frequencies when using the 'fine' mesh (shown in Figure 1) are within 2% of the convergent values obtained using much finer meshes, which require prohibitively long computation times. Mesh element sizes range from 0.33 mm to 2.61 mm. The largest element is about 6 times smaller than the smallest wavelength observed in the frequency range of interest (1 – 310 kHz), which is about 15.0 mm. The lattice struts have approximately nine elements over the length. The simulations are conducted using COMSOL's *Solid Mechanics* module assuming a homogenous and linear elastic constituent material with the properties given in Table 1, which correspond to the CoCrMo alloy used for the physical samples [46,47]. Traction-free BCs are applied to all external surfaces in accordance with the experimental configuration of RUS (Section 4.3.2).

Table 1: The material properties used for numerical simulations of the lattice samples.

Modulus of Elasticity	Poisson's Ratio	Density
190 GPa	0.30	8.3 g/cm^3

Two simulation modalities are employed: *eigenfrequency* and *frequency domain. Eigenfrequency* analysis provides the resonance frequencies and mode shapes corresponding to the free vibration of the sample with high computational efficiency. Here, *eigenfrequency* analysis is used to compute the first 225 eigenmodes of each sample. A *frequency domain* analysis provides

the full spectral response of the sample subjected to a series of applied harmonic forces with frequencies in a given range; therefore, it more closely emulates the experimental condition. Experimentally, the sample is held at its corners between point-sized transmitting and receiving transducers that excite the sample and record the response, respectively (see Figure 21(a) in Sec. 3.3.2). In the simulation environment, depicted in Figure 2, a point-load with three equal components in the x, y, and z directions is applied at one corner of the sample to simulate the excitation. The total displacement history is recorded at the opposite corner, where the sensor is positioned during experimental testing. The output recording position is placed 1.93 mm to the right of the midline for all numerical simulations, which is the approximate location used during experimental testing. Note that in this analysis, the direction and location of the excitation force influence what modes are excited. Also, the recorded spectrum will depend on the sensor (i.e., recording point) location and the direction, along which the displacement is recorded.

Post processing is conducted in MATLAB 2020a. The *eigenfrequency* analysis consists of calculating frequency differences of the corresponding modes when comparing the pristine and defective samples. The spectra obtained using the *frequency domain* analysis are first globally normalized to have a unit maximum amplitude. Frequency peaks are found using *peakfinder* - a function available through the MATLAB file exchange – after setting a normalized amplitude threshold of 0.0002 a.u. Subsequently, the amplitudes of the found peaks in each individual frequency spectrum are locally normalized. Local normalization minimizes the effect of relative peak amplitudes by setting all resonance frequency amplitudes to unity. The local normalization is accomplished by first defining a series of 'frequency bins' around the identified peaks. The start and end of each bin are chosen halfway in between successive frequency peaks. For example, if there are three successive peaks at 10 kHz, 13 kHz, and 25 kHz, the frequency bin around the peak

at 13 kHz would extend from 11.5 to 19 kHz. Next, the portion of the spectrum falling within each bin is linearly scaled such that the corresponding peak's amplitude is normalized to unity while the bin's start and end amplitudes are preserved. This is to prevent big jumps at transitions between adjacent bins and ensure the continuity of the locally normalized spectrum. Examples of locally normalized spectra are provided in Figure 17 in Sec. 3.2.3.

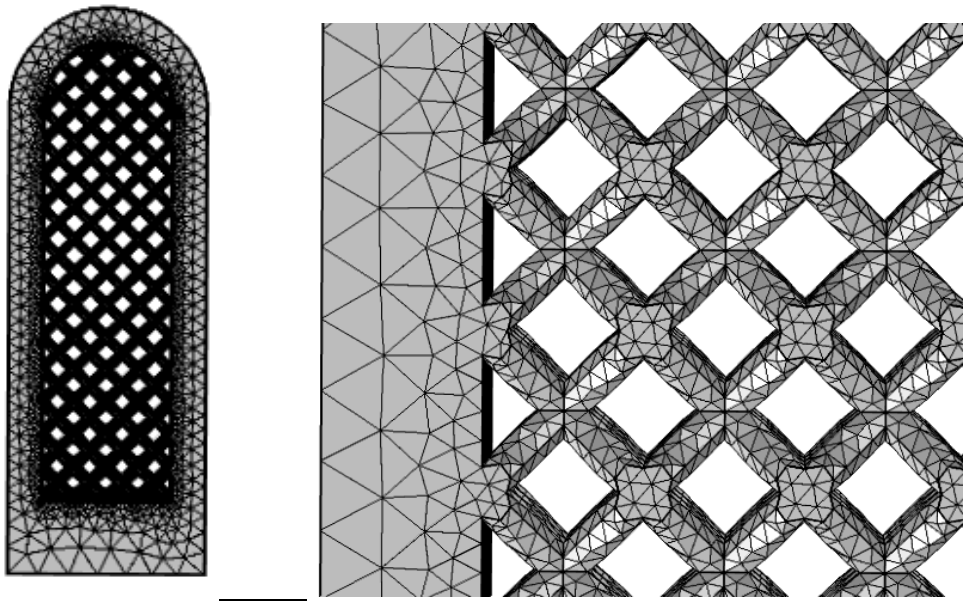

Figure 1: The 'fine' sized elements are used for generating the finite elements mesh.

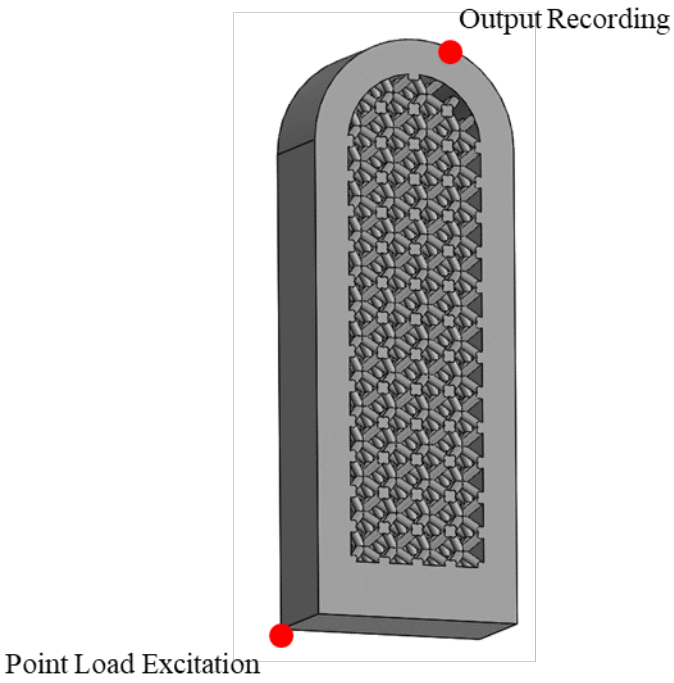

Figure 2: The locations of the point load excitation and the output recording used in the frequency domain simulations shown on a pristine lattice.

3.2.2 CHANGES IN RESONANCE FREQUENCIES OF LATTICE STRUCTURES DUE TO MISSING STRUTS

A series of *eigenfrequency* analyses are conducted to compare the resonance frequencies of a pristine lattice and six defective lattices with one or more *external* missing struts. Resonance frequencies of the corresponding modes in the range 0-~300 kHz are compared to evaluate the frequency differences caused by the missing struts. The difference is calculated by subtracting the eigenfrequencies from the defective lattice from that of the pristine lattice. The results presented in this section pertain to simulated lattices with no engraving. For each of the six defect conditions corresponding to the number of missing struts, struts are sequentially removed. For example, for a lattice with two missing struts, the location of one of the struts corresponds to that in the one missing strut condition and so forth. In order to evaluate the influence of missing strut locations, we analyze five different cases for each condition by varying the locations of the missing strut(s). Case 1 for each condition corresponds to the locations of the missing struts in the physical lattices,

except for the lattices with eight and twelve missing struts, where the physical lattices feature both internal and external missing struts.

Figure 3(a) depicts the differences in the first 225 resonance frequencies for the five different cases of one missing strut condition when compared to a pristine lattice. Figure 3(b-f) provide the locations of the missing strut for each case. These results demonstrate that even a single missing strut can shift the resonance frequencies of a pristine sample, given the resulting change in effective properties [28]. Additionally, we observe that the maximum shift in resonance frequency and at what frequency it occurs depend on the location of the missing strut, the reason behind which becomes apparent by a close inspection of the corresponding mode shapes. For example, the 95th mode for Case 2 displays the largest frequency difference (2.17 kHz). The corresponding mode shapes for the pristine and defective lattices are given in Figure 4(a) and (b), respectively. These are comparable to the mode shape pair shown in Figure 5(a) and (b) corresponding to the 31st mode, for which the frequency difference is minimum. Comparing the two pairs of mode shapes, we observed that when the frequency difference is maximum, the location of the largest modal displacement coincides with the missing strut location. Also, when the frequency difference is minimum, the pristine and defective samples exhibit fairly similar mode shapes. We can interpret that as the missing strut not having a strong influence on the vibrational response. Similar observations are made for Case 1, for which, the maximum frequency difference of 1.43 kHz occurs at the 203rd mode. The 203rd mode of the lattice with one missing strut is compared to the 203rd mode of a pristine lattice in Figure 6(b) and (a), respectively. In both Cases 1 and 2, the modes corresponding to maximum frequency differences exhibit the largest displacement amplitudes at or about the location of the missing strut. Although the lattice with one missing strut and the pristine lattice do not have the same mode shapes, the highest displacement

amplitude on the pristine lattice may also be adjacent to the locations of the one missing strut. Most likely, this is due to the proximity of the geometries and thus the mode shapes between the pristine lattice and the lattice with one missing strut. These results suggest that, it could be possible to predict the location of a single missing strut in a defective lattice based on the mode shapes of the pristine lattice. However, we do not expect that this would be the case for defective lattices with a large number of missing struts due to the larger influence of the missing elements on the geometry and mode shapes. For example, we consider the twelve missing struts condition. Figure 8(a) depicts the differences in the first 225 resonance frequencies for the five cases with Figure 8(b-f) providing the locations of the twelve missing struts for each case. Figure 9 and Figure 10 depict two mode shapes that correspond to the maximum and minimum frequency differences observed for Case 3. For Case 3, the 203rd mode exhibits a frequency difference of 4.84 kHz. Figure 9(b) shows that similar to what was observed for the sample with one missing strut, the displacement amplitude for the defective sample is largest around the locations of missing struts. As expected, the modal displacement distribution is quite different for the pristine lattice as depicted in Figure 9(a). Similarly, Figure 10 confirms our earlier observation that the mode shapes of the pristine and defective lattices are fairly similar, when the frequency difference is minimal. A somewhat exceptional case is Case 5 having a series of aligned missing struts exhibiting a maximum frequency difference of 6.94 kHz for the 147th mode. As shown in Figure 11(a) and (b), the displacement amplitudes for this mode for both the pristine lattice and the defective lattice with twelve missing struts are largest along or adjacent to the line of missing struts, although the mode shapes are quite different. This observation is surprising given that we expect the aligned missing struts to collectively behave like a large defect resulting in a significant deviation of the mode shape and modal displacement field from those for the pristine sample. This is possibly the reason

why Case 5 displays an overall larger frequency difference compared to the other four cases, especially at higher modes. Interestingly, this also holds for the other defective lattices with four or more missing struts i.e., Case 5 having the missing struts in a row shows the largest frequency differences. Figure 12(a) and (b) show that when the frequency difference is minimal, the mode shapes of the pristine and the defective lattices are again similar.

Although the maximum frequency difference is impacted by the location of the missing struts for both conditions presented above, the average frequency difference remains nearly constant across the five cases considered (see Figure 3(a) and 8(a)). For all cases considered, lattices with twelve missing struts display a larger average frequency difference than those with one missing strut. Figure 13 shows that similar conclusions can be drawn for intermediate conditions namely, two, four, six, and eight missing struts. By aggregating the data from all five cases of each defect condition, we systematically evaluate the impact of increasing the number of missing struts on the simulated eigenfrequencies. Table 2 provides an overview of the mean frequency differences for the five cases of lattices with a varying number of missing struts. It is evident that as the number of missing struts increases, the mean frequency difference also increases. Notably, the standard deviation of the frequency differences also increases, which is evident considering the observed increased spread of the data in Figure 13. The spread of frequency differences for each condition is further quantified using the five-number summaries illustrated in Figure 14(a). Three parameters are shown to increase with the increasing number of missing struts, namely: the range between maximum and minimum frequency differences (depicted in black), the median frequency difference (depicted in red), and the interquartile range (depicted in blue). The sensitivity of each metric to the number of missing struts is depicted in Figure 14(b), which shows that the range as a function of number of missing struts has the largest slope.

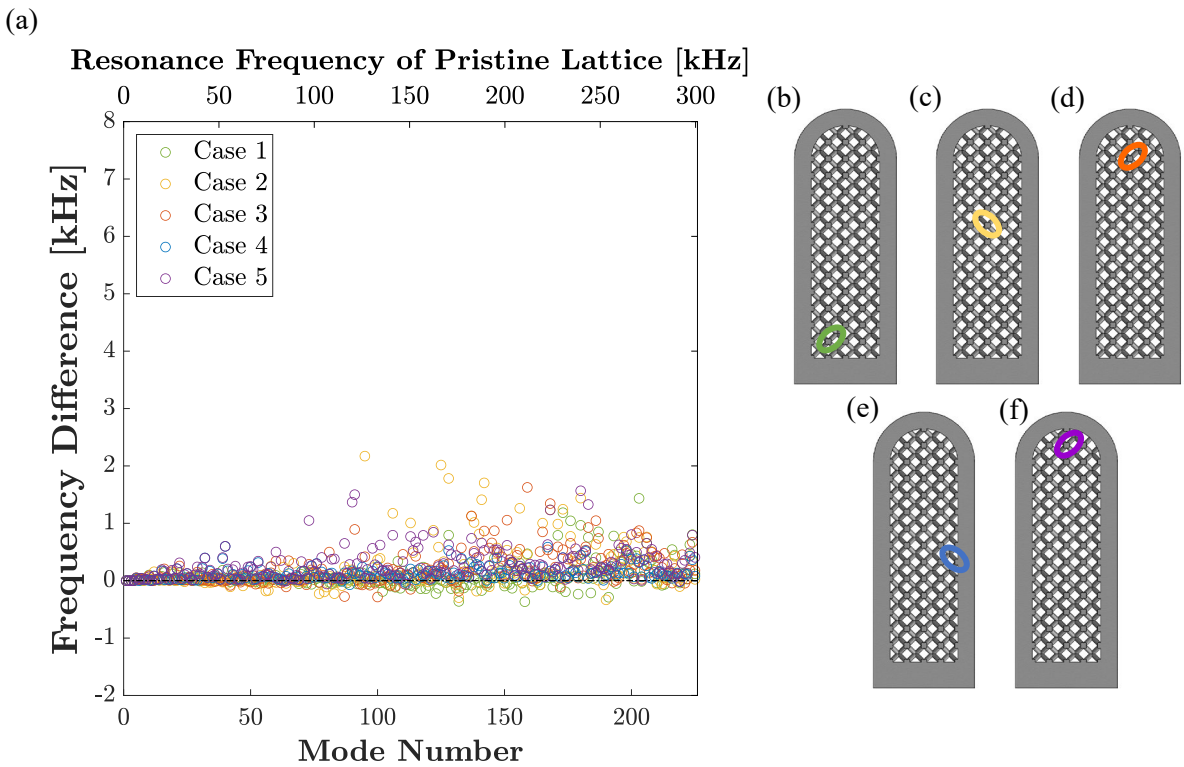

Figure 3: Simulation results (*eigenfrequency* analysis): (a) Resonance frequency differences between a pristine lattice and a lattice with one missing strut at locations depicted in (b)-(f) sequentially labeled Case 1-5. The missing struts are located on the outer layer of the lattice structure for all cases.

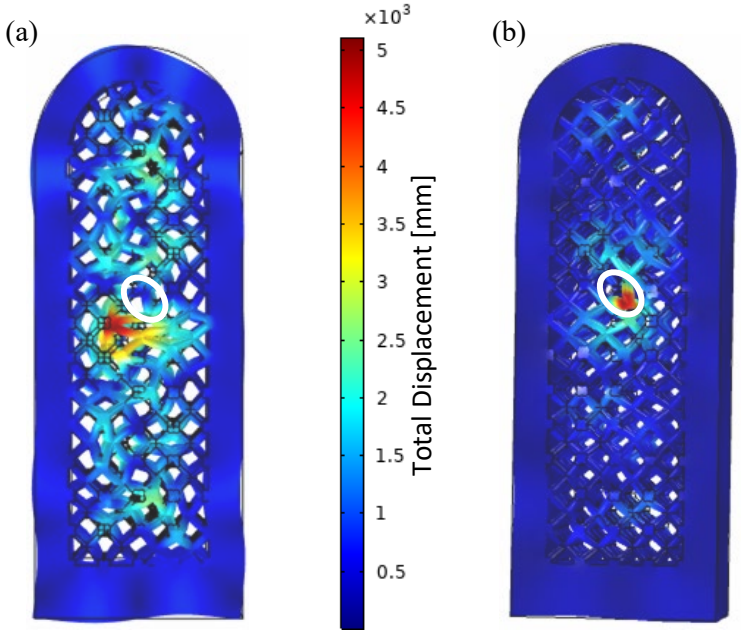

Figure 4: The modal shapes of the 95th resonance modes of (a) the pristine lattice with a corresponding resonance frequency of 213.48 kHz and (b) Case 2 of the lattice with one missing strut with a corresponding resonance frequency of 211.31 kHz. The white ovals depict the locations of the missing element in Case 2.

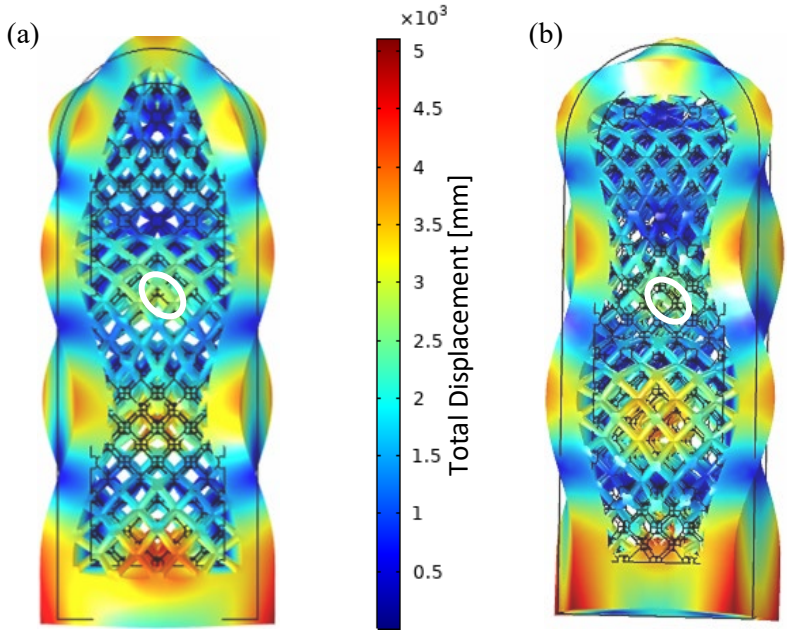

Figure 5: The modal shapes of the 31st resonance modes of (a) the pristine lattice with a corresponding resonance frequency of 119.23 kHz and (b) Case 2 of the lattice with one missing strut with a corresponding resonance frequency of 119.23 kHz. The white ovals depict the locations of the missing element in Case 2.

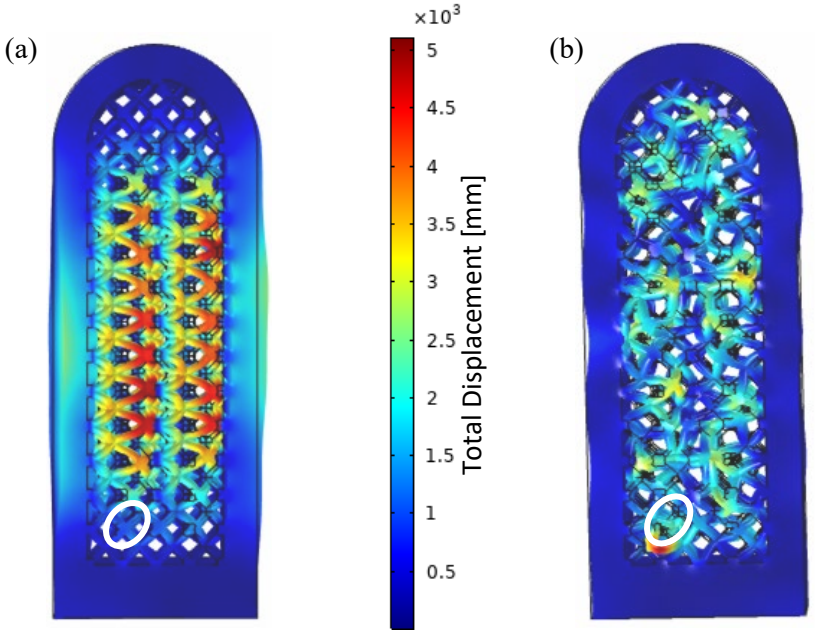

Figure 6: The modal shapes of the 203rd resonance modes of (a) the pristine lattice with a corresponding resonance frequency of 291.15 kHz and (b) Case 1 of the lattice with one missing strut with a corresponding resonance frequency of 289.72 kHz. The white ovals depict the locations of the missing element in Case 1.

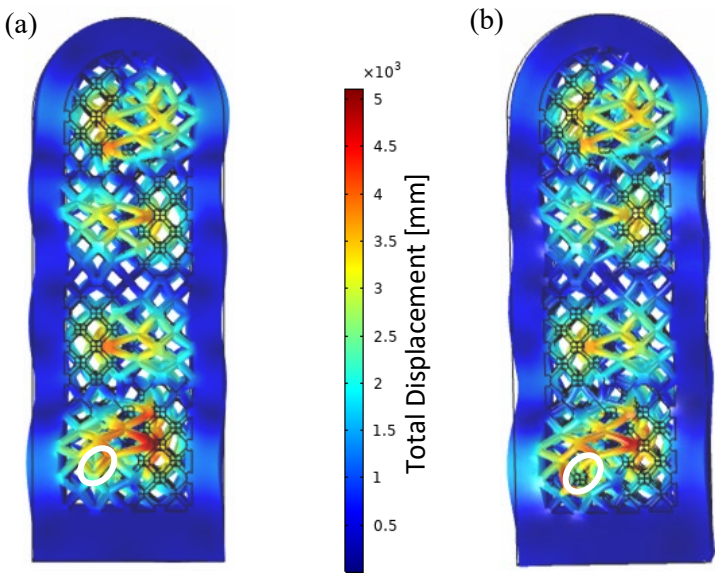

Figure 7: The modal shapes of the 84th resonance modes of (a) the pristine lattice with a corresponding resonance frequency of 200.25 kHz and (b) Case 1 of the lattice with one missing strut with a corresponding resonance frequency of 200.25 kHz. The white ovals depict the locations of the missing element in Case 1.

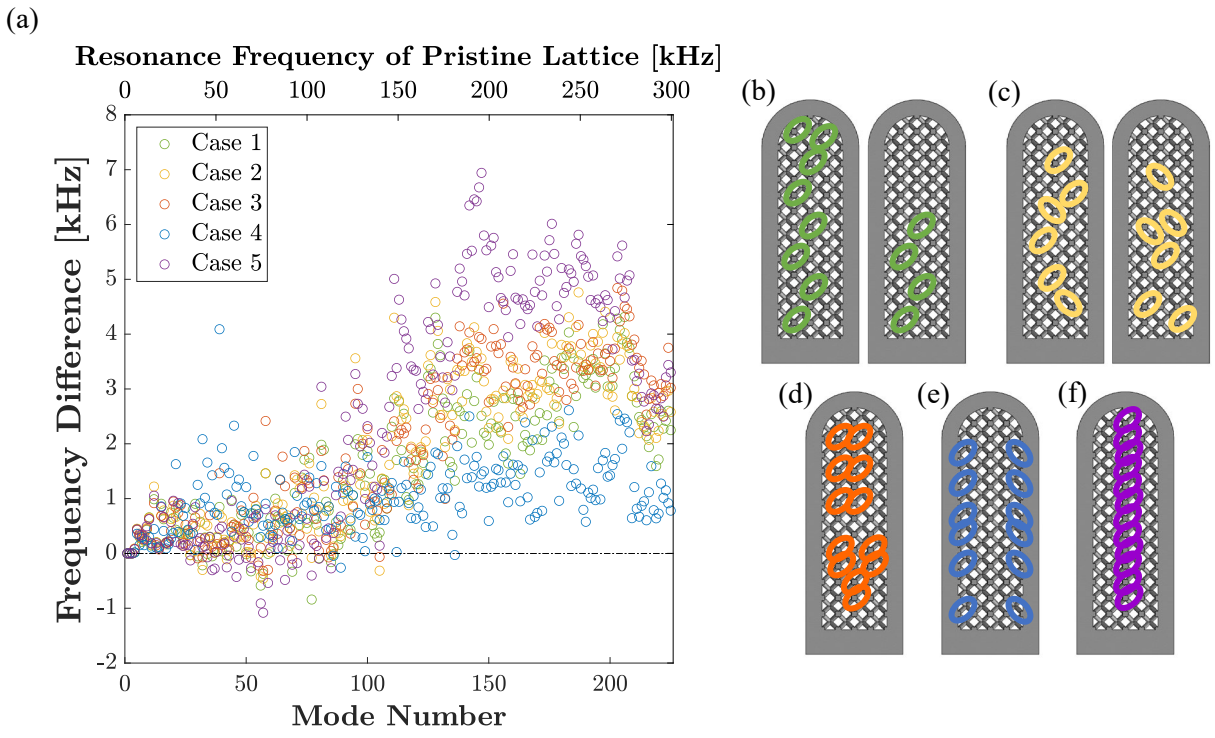

Figure 8: Simulation results (*eigenfrequency* analysis): (a) Resonance frequency differences between a pristine lattice and a lattice with twelve missing struts at locations depicted in (b)-(f) sequentially labeled Case 1-5. Missing struts are located on the outer layer of the lattice structure for all cases. Note that the lattice in Case 1 shown in (b) has eight missing struts on one side and four on the other side and that the lattice in Case 2 shown in (c) has six missing struts on one side and six on the other side.

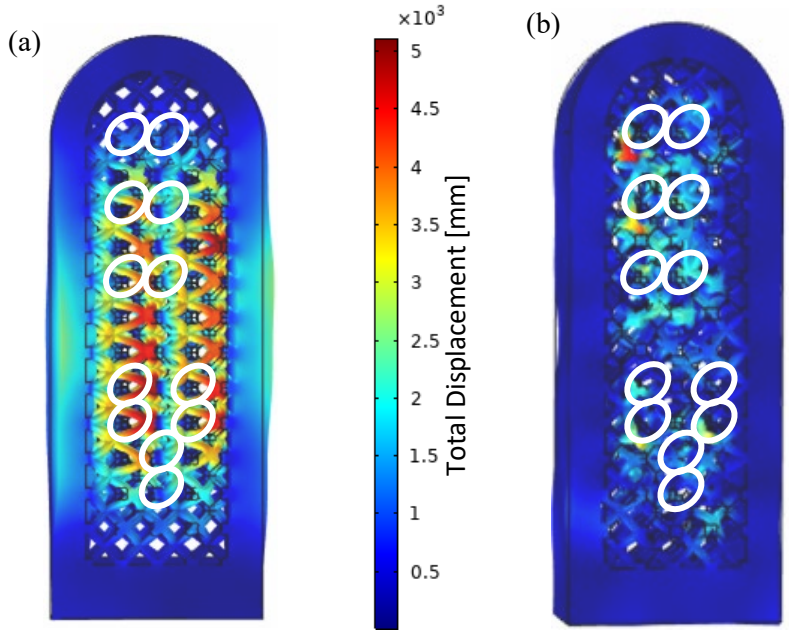

Figure 9: The modal shapes of the 203rd resonance modes of (a) the pristine lattice with a corresponding resonance frequency of 291.15 kHz and (b) Case 3 of the lattice with twelve missing struts with a corresponding resonance frequency of 286.31 kHz. The white ovals depict the locations of the missing elements in Case 3.

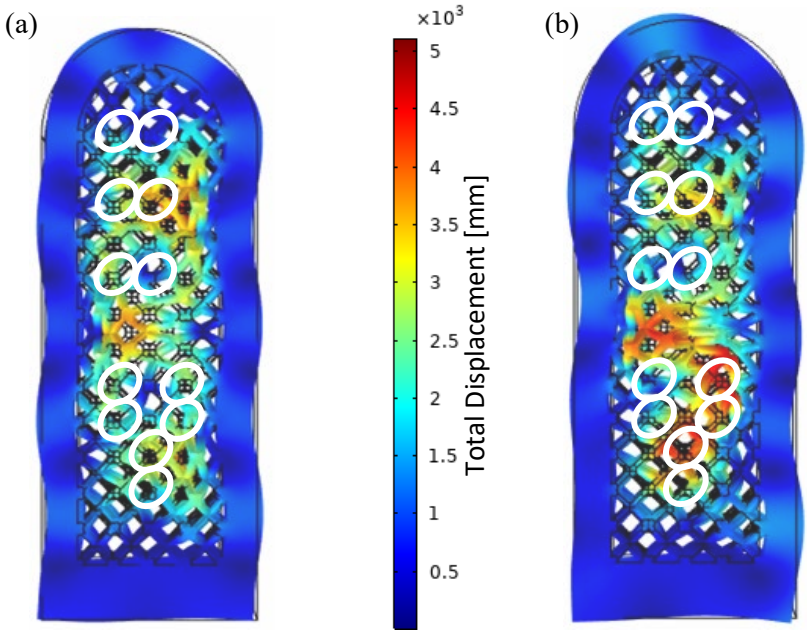

Figure 10: The modal shapes of the 37th resonance modes of (a) the pristine lattice with a corresponding resonance frequency of 128.94 kHz and (b) Case 3 of the lattice with twelve missing struts with a corresponding resonance frequency of 128.92 kHz. The white ovals depict the locations of the missing elements in Case 3.

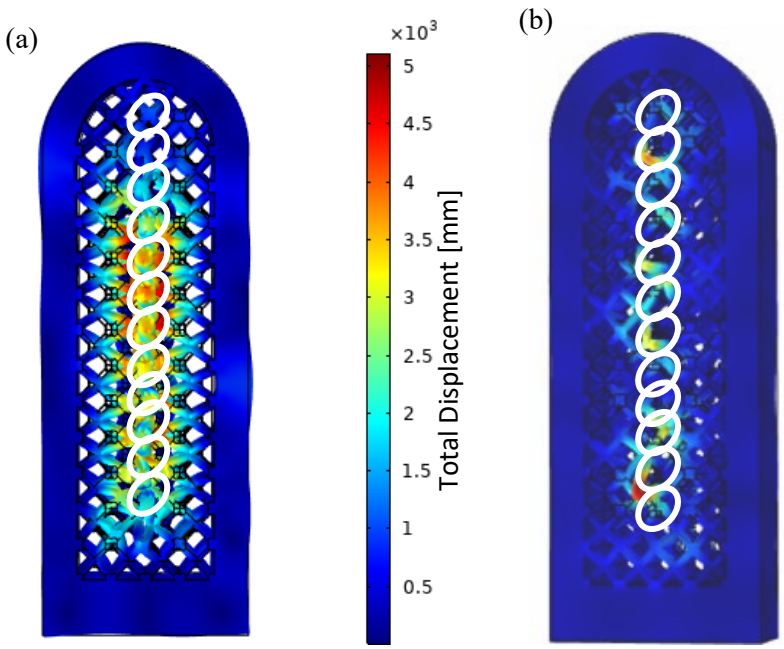

Figure 11: The modal shapes of the 147th resonance modes of (a) the pristine lattice with a corresponding resonance frequency of 255.93 kHz and (b) Case 5 of the lattice with twelve missing struts with a corresponding resonance frequency of 248.99 kHz. The white ovals depict the locations of the missing elements in Case 5.

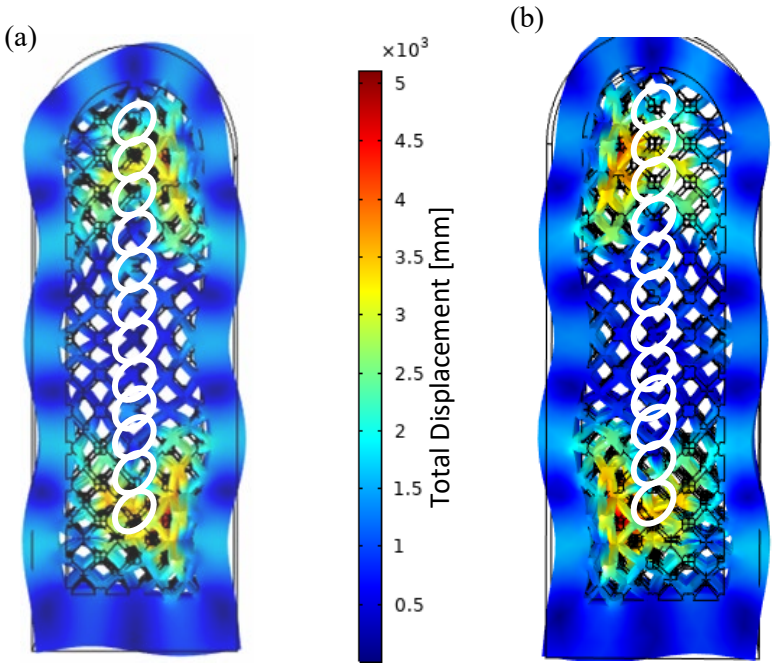

Figure 12: The modal shapes of the 38th resonance modes of (a) the pristine lattice with a corresponding resonance frequency of 130.91 kHz and (b) Case 5 of the lattice with twelve missing struts with a corresponding resonance frequency of 130.88 kHz. The white ovals depict the locations of the missing elements in Case 5.

(a)

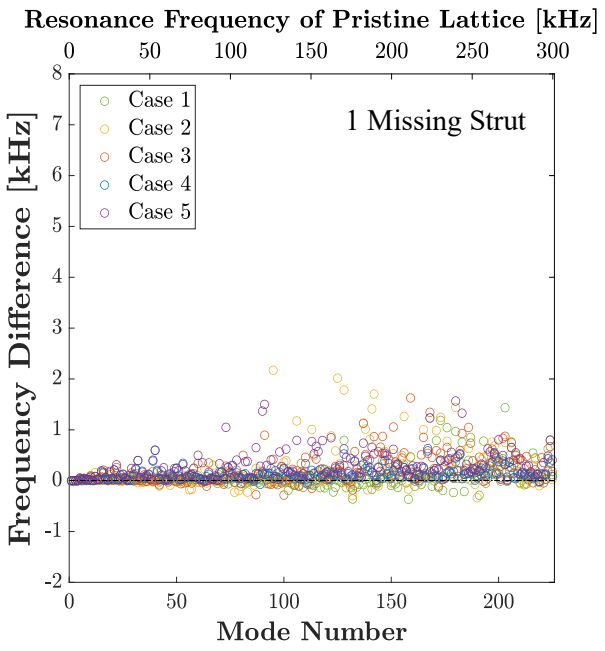
Resonance Frequency of Pristine Lattice [kHz]
Frequency Difference [kHz]
Mode Number
Case 1
Case 2
Case 3
Case 4
Case 5
1 Missing Strut

(b)

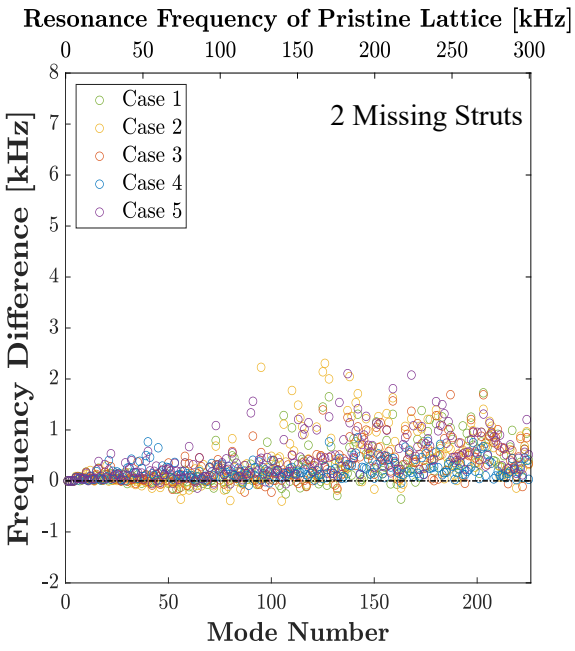
Resonance Frequency of Pristine Lattice [kHz]
Frequency Difference [kHz]
Mode Number
Case 1
Case 2
Case 3
Case 4
Case 5
2 Missing Struts

(c)

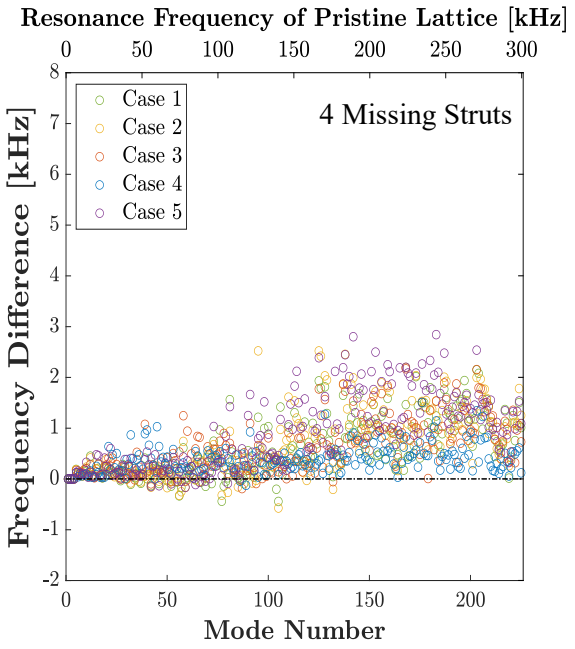
Resonance Frequency of Pristine Lattice [kHz]
Frequency Difference [kHz]
Mode Number
Case 1
Case 2
Case 3
Case 4
Case 5
4 Missing Struts

(d)

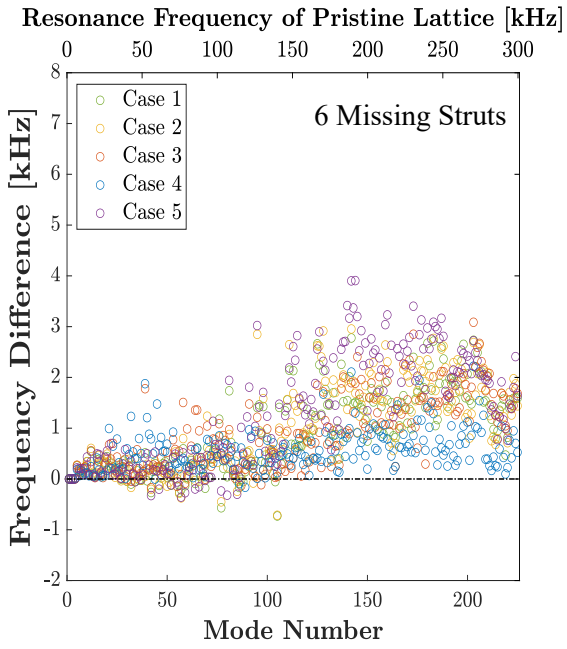
Resonance Frequency of Pristine Lattice [kHz]
Frequency Difference [kHz]
Mode Number
Case 1
Case 2
Case 3
Case 4
Case 5
6 Missing Struts

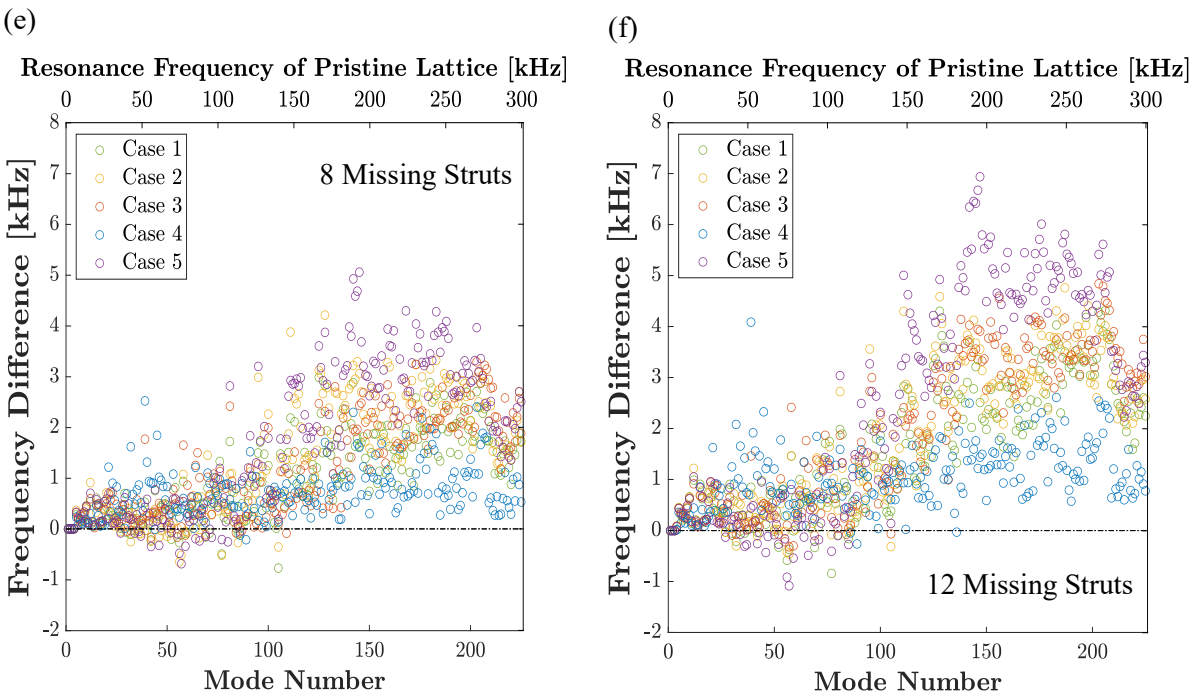

Figure 13: Simulation results (*eigenfrequency* analysis): Resonance frequency differences between a pristine lattice and a lattice with (a) one, (b) two, (c) four, (d) six, (e) eight, and (f) 12 missing strut(s). The schematics showing the missing strut locations for each condition are included in the Appendix.

Table 2: Summary statistics of the frequency difference between the pristine sample and five cases of samples with a varying number of missing struts. The bounds for the mean and mean of maximum frequency differences correspond to the standard deviations for the five individual cases.

Number of Missing Strut(s)	Mean Frequency Differences [kHz]	Mean of Maximum Frequency Differences [kHz]	Standard Deviation of Aggregate Frequency Differences
1	0.1714±0.0712	1.4789±0.5672	0.2794
2	0.3281±0.0947	1.7357±0.5593	0.3997
4	0.6286±0.1757	2.2375±0.4988	0.5953
6	0.9270±0.2600	2.9889±0.6102	0.8356
8	1.2140±0.3660	3.6141±1.0153	1.0656
12	1.8162±0.5459	4.9893±1.1350	1.5351

(a)

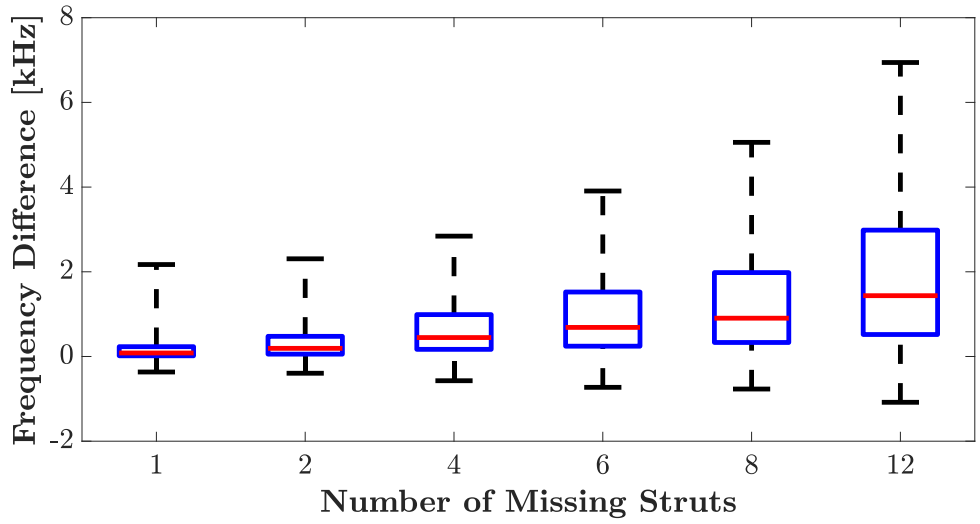

(b)

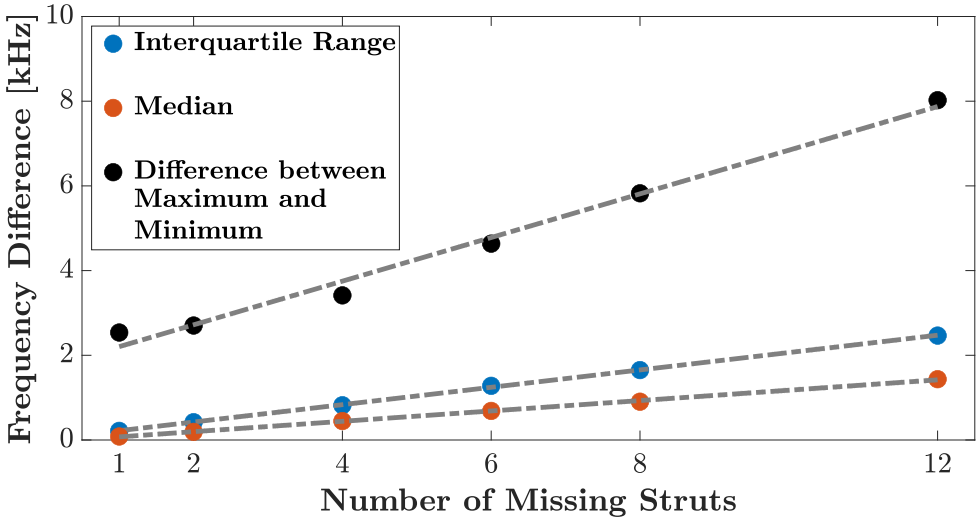

Figure 14: (a) Five-number summaries from aggregate data for five cases of resonance frequency differences between pristine lattices and lattices with an increasing number of missing struts. (b) The interquartile range (middle 50%), median, and range between the maximum and minimum frequency differences scale linearly with the number of missing struts with range having the largest slope.

In addition, Figure 13 suggests a systematic trend in the calculated frequency difference vs. mode number plots. Specifically, the frequency difference between the defective and pristine lattices appears to be significant over a certain range of modes. In other words, the deviation from the

pristine sample response starts to grow beyond a first "critical" mode and will eventually decrease for modes higher than a second "critical" mode. A close examination of the plots for individual cases reveal that both the location and number of missing struts affect these two critical modes. Generally speaking, the frequency differences for the cases and conditions analyzed here become significant for a range of modes between the 50^{th} and 200^{th} (equivalent to the resonance frequency range of about 154.0-288.5 kHz for the pristine sample) with the range being generally wider for the lattices with a larger number of missing struts. This information is useful in informing the frequency range in the experimental investigation.

The findings presented in this section show that a sample with even a single missing strut exhibits different resonance frequencies than a pristine sample. As the number of missing struts increases, the differences in resonance frequencies of the defective and pristine lattices become increasingly large and appear at relatively lower modes. Our analysis shows that for the same number of missing struts, the location of the missing strut does not strongly influence the eigenfrequency differences unless they are aligned or located near the edges. In the next section, an analysis of the influence of the different engraved numbers on the response of the lattices is discussed.

3.2.3 INFLUENCE OF ENGRAVING ON RESONANCE FREQUENCIES

We evaluate the influence of sample engraving by first comparing the resonance frequencies of three pristine lattices with different numbers corresponding to the physical samples, as shown in Figure 15. Each engraved number has a depth of 0.75 mm, in accordance with the manufacturer's CAD models. The resonance frequency differences between a lattice with a "037" engraving and samples with "024" and "061" engravings are given in the plot of Figure 15. The largest frequency difference is 0.53 kHz observed between "037" and "061" at the 210^{th} mode: 293.54 kHz vs.

294.08 kHz. On average, the frequency differences due to engraving are negligible compared to those incurred by missing struts.

To better simulate the impact of engraving on the experimental spectra, a *frequency domain* analysis is conducted. The spectra corresponding to the pristine sample with three different engraved numbers are shown in Figure 16(a) and the mean and standard deviation of the frequency and amplitude of similar peaks are given in Figure 16(b). A total of 211 peaks are identified across the three spectra, 23 of which (10.9%) appear in only two of the spectra. None of the 211 peaks appear in only one spectrum. Comparing the three spectra, we observe that the error bars for frequencies are smaller than the markers, indicating little variations in resonance frequencies; however, there are occasional large variations in normalized amplitudes. The largest standard deviation in frequency of similar peaks is 0.173 kHz occurring in the frequency range 290.4 – 290.7 kHz. This is different from the largest standard deviation observed in the *eigenfrequency* analysis because the 210^{th} mode of "061" appears not having been excited in the *frequency domain* study. The normalized amplitudes of similar peaks from the three pristine samples vary, with the largest standard deviation being 0.55. These amplitude variations complicate the comparison of spectra as only frequency differences seem to be pertinent in differentiating different samples while the amplitude may vary due to engravings, and as will be shown later, due to slight differences in placement of the sample when conducting the experiments. This necessitates further normalization of the spectra to neutralize the impact of amplitude variations. Having compared the three pristine lattices, we compare engraved samples with a varying number of missing struts corresponding to the physical samples in the next section.

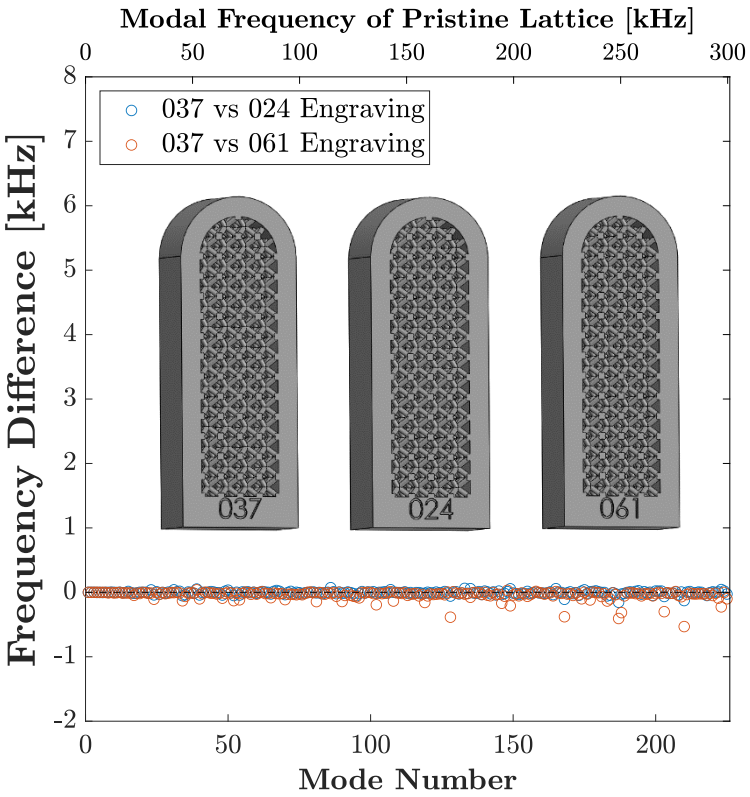

Figure 15: The influence of engraved sample numbers on the eigenfrequencies of a pristine lattice. The frequency difference between Sample “037” and “024” or “061” shown in the inset.

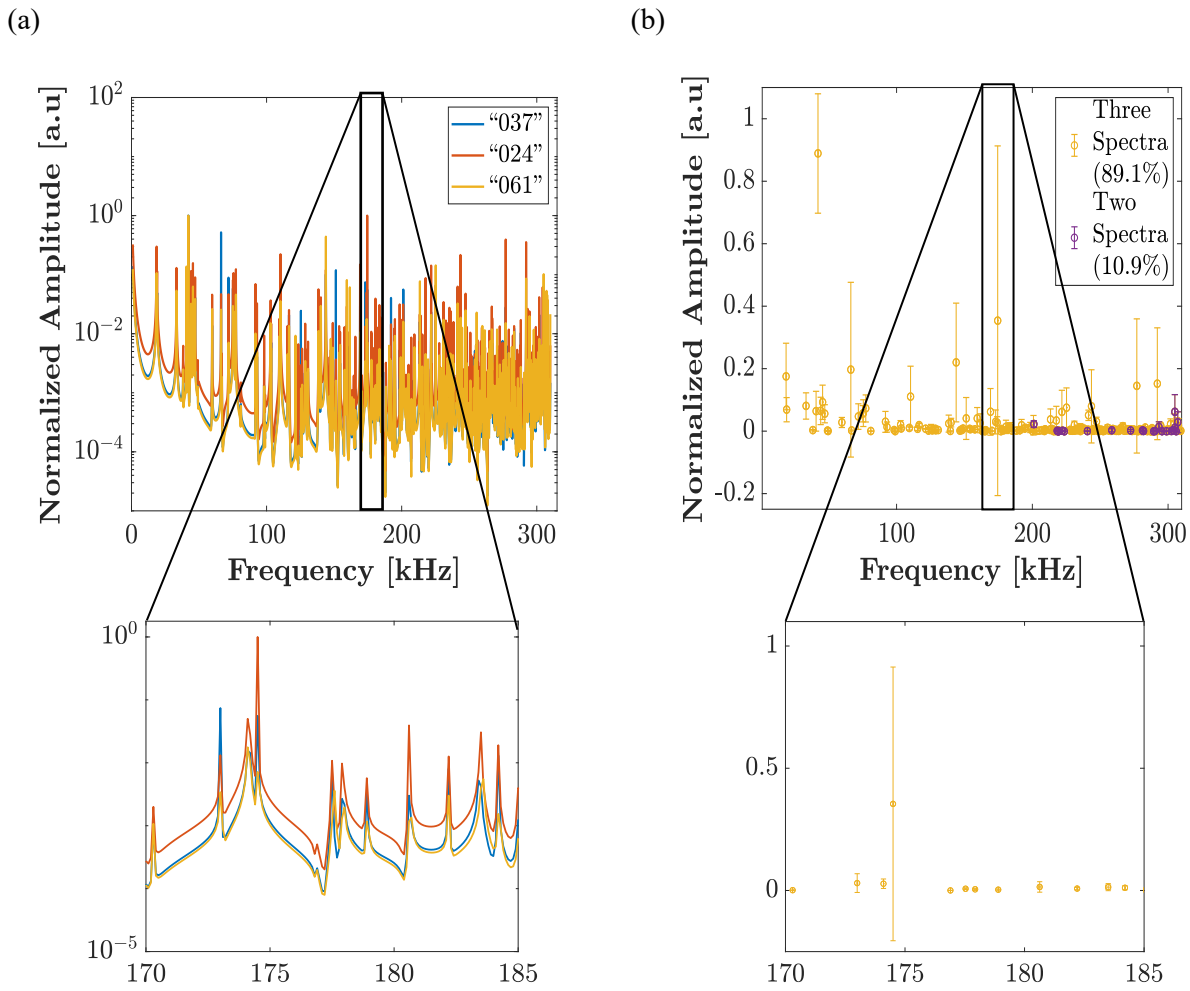

Figure 16: (a) A comparison of the simulated spectra of pristine lattices "037", "024", and "061" from the *frequency domain* study; (b) The mean and standard deviation for the frequency and amplitude of similar resonance peaks of the three engraved pristine samples as compared to the spectrum of "037".

Samples with a different number of missing struts are engraved in accordance with the physical engravings as noted in Table 5 in Sec. 3.3.1. Figure 17(a) compares the frequency spectra of pristine sample "037" and sample "140" having twelve missing struts with the spectral amplitudes for each sample globally normalized. As previously noted, a method that reduces the influence of spectral amplitudes deems necessary. Here, a local normalization procedure is used to equate the amplitude of resonance peaks in each spectrum while adjusting the spectral amplitudes in their

vicinities to preserve the shape of the peak and continuity of the spectrum. Figure 17(b) shows the locally normalized spectra of Samples “037” and “140” superimposed.

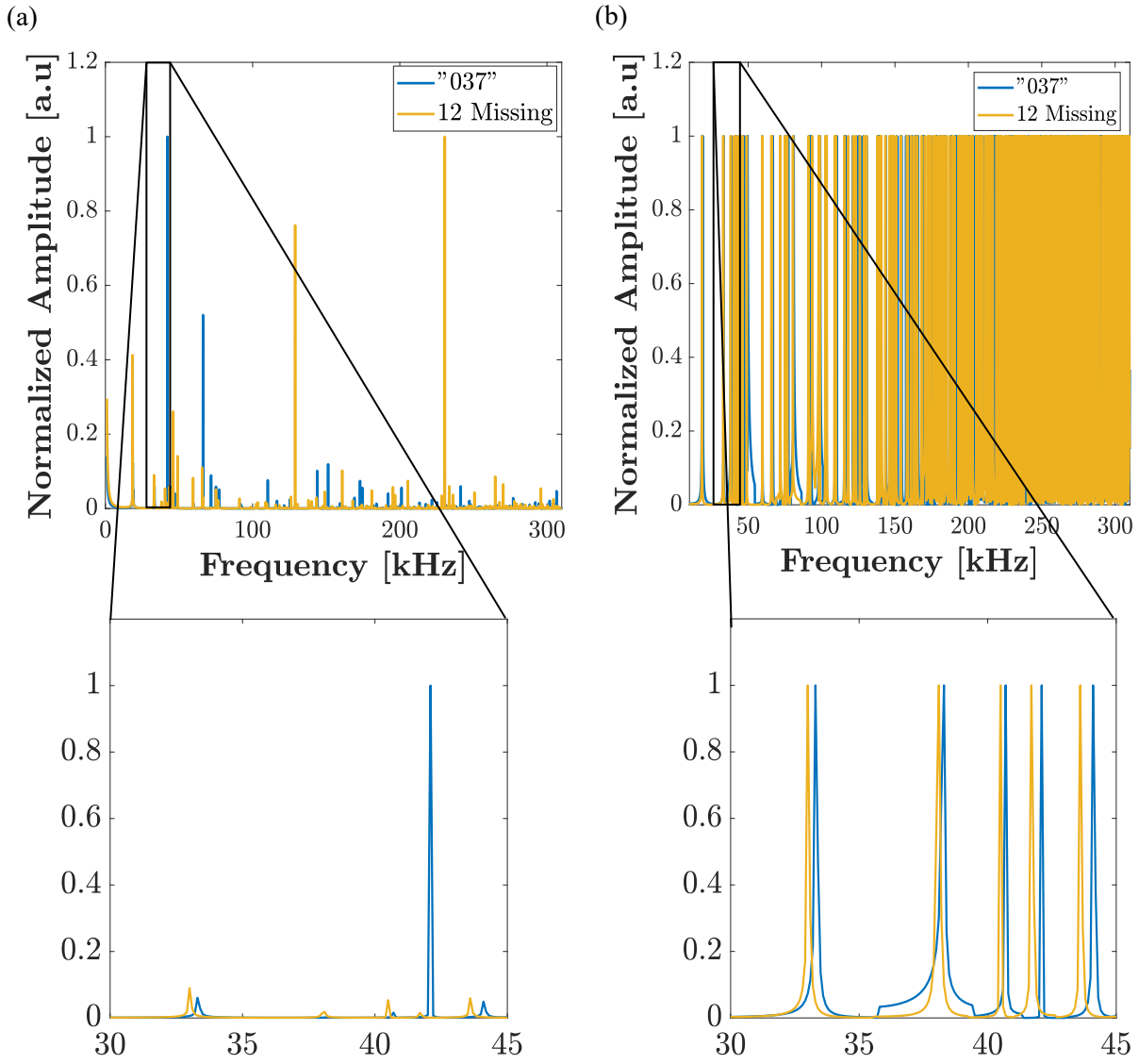

Figure 17: A comparison between the spectra of pristine Sample “037” and defective Sample“140” with 12 missing struts when the amplitudes are: (a) globally normalized by the maximum amplitude and (b) locally normalized to equate the amplitudes for all peaks.

Finally, we compare the spectra of the pristine and defective samples by calculating the maximum correlation coefficients between every two spectra. The calculated correlation coefficients are summarized in Table 3 and Table 4, for globally and locally normalized spectra, respectively.

Figure 18(a) and (b) depict the same data graphically. The correlation study results for the globally normalized spectra do not show a clear trend and do not provide concrete distinction between pristine and defective lattices. In this case, the maximum correlation coefficients across pristine samples range from 0.566 to 0.847 with one of the lowest correlations calculated between the two pristine samples “024” and “037”. Also, the correlation between pristine lattices and the defective lattice with twelve missing struts range from 0.409 to 0.671, which is akin to the variations observed across pristine samples. We attribute these inconsistencies to the large variations in the spectral amplitudes of the three samples as reported in Figure 16. When we locally normalize the spectra, the correlation coefficients depicted in Figure 18(b), show a clear distinction between pristine and defective lattices. A gradient from light to dark colors, corresponding to a decrease in correlation coefficient, is observed as the number of missing struts increases. The correlation across pristine samples ranges from 0.774 to 0.889 and the correlation between pristine lattices and the lattice with twelve missing struts drops to 0.263-0.277. This analysis suggest that the maximum cross correlation coefficient is an appropriate metric for comparing the spectra after applying local normalization. In the next section, we use this analysis procedure to investigate whether this same metric can be used to distinguish intact and defective lattices from their experimental spectra.

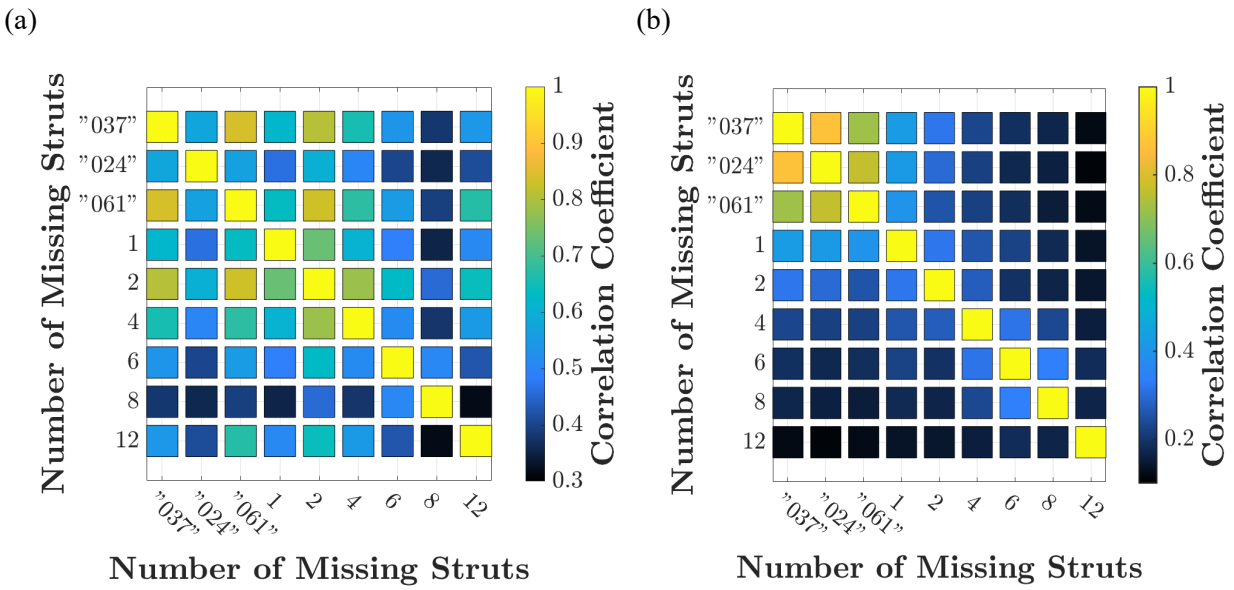

Figure 18: (a) The maximum cross-correlation coefficient between spectra of all samples with amplitudes normalized by the maximum amplitude; (b) The maximum cross-correlation coefficient between spectra of all samples with peak amplitudes normalized to one.

Table 3: The maximum cross-correlation coefficient calculated between every two spectra with globally normalized amplitudes.

	Number of Missing Struts								
	"037"	**"024"**	**"061"**	**1**	**2**	**4**	**6**	**8**	**12**
"037"	1.000	0.576	0.837	0.619	0.806	0.657	0.573	0.381	0.543
"024"	0.577	1.00	0.566	0.463	0.598	0.500	0.402	0.359	0.409
"061"	0.837	0.566	1.000	0.637	0.830	0.676	0.553	0.390	0.672
1	0.619	0.463	0.637	1.000	0.735	0.608	0.485	0.354	0.509
2	0.806	0.598	0.830	0.735	1.000	0.782	0.629	0.454	0.644
4	0.657	0.500	0.676	0.608	0.782	1.000	0.515	0.377	0.549
6	0.537	0.402	0.553	0.485	0.629	0.515	1.000	0.507	0.425
8	0.381	0.359	0.390	0.354	0.454	0.377	0.506	1.000	0.319
12	0.543	0.409	0.671	0.509	0.644	0.549	0.425	0.319	1.000

Table 4: The maximum cross-correlation coefficient calculated between every two spectra with locally normalized amplitudes.

	Number of Missing Struts								
	"037"	**"024"**	**"061"**	**1**	**2**	**4**	**6**	**8**	**12**
"037"	1.000	0.889	0.774	0.524	0.429	0.365	0.338	0.318	0.276
"024"	0.889	1.00	0.809	0.519	0.413	0.3569	0.327	0.307	0.263
"061"	0.774	0.809	1.000	0.504	0.379	0.358	0.338	0.303	0.277
1	0.524	0.519	0.504	1.000	0.4237	0.379	0.358	0.315	0.277
2	0.429	0.413	0.379	0.423	1.000	0.388	0.328	0.299	0.278
4	0.365	0.356	0.358	0.379	0.388	1.000	0.437	0.364	0.300
6	0.338	0.327	0.338	0.358	0.328	0.437	1.000	0.459	0.328
8	0.318	0.307	0.303	0.315	0.299	0.364	0.459	1.000	0.309
12	0.276	0.263	0.277	0.277	0.278	0.300	0.328	0.309	1.000

3.3 EXPERIMENTAL VALIDATION

Nine lattice structures analogous to those studied in the numerical simulations are experimentally tested for validation: three pristine and six with one or more missing struts. Each sample is tested five times to investigate repeatability of the measurements. The measured frequency spectra are normalized following the same procedure used for the simulated spectra and the maximum pairwise correlation coefficient for the nine samples is calculated. Finally, the experimental results are compared with the numerical results to determine the feasibility of RUS for identifying defects in complex lattice structures. A discussion on the observed discrepancies between the numerical and experimental results is provided.

3.3.1 SAMPLE DESCRIPTION

The National Institute of Standards and Technology (NIST) additively manufactured lattice geometries through powder bed fusion (PBF) using EOS CobaltChrome (CoCr) MP1, a CoCrMo-based superalloy powder specifically adjusted for processing on EOSINT M systems. As-built structures of this material yield a chemical composition of UNS R31538, a high-carbon CoCrMo

alloy. According to the EOS datasheet, the modulus of elasticity and the density of the material are 190-220 GPa and 8.3 g/cm^3, respectively [46]. The datasheet does not provide the Poisson's ratio; thus, a value of 0.30 is used when appropriate [47]. The same material properties were used for numerical simulations, as given in Table 1, Sec. 3.2.1. Three samples are pristine and six feature one or more missing struts, confirmed by visual inspection. Figure 19(a)-(d) depict CAD models of the lattices with one, two, four, and six missing strut(s), where all the missing elements are located on the exterior and marked in red. Figure 19(e) and (f) depict lattices with eight and twelve missing struts where the *external* missing struts are marked in red and the approximate location of the *internal* missing struts are marked in blue. The physical lattices have identical dimensions but different engraved sample numbers, specified in Table 5. Due to build failure midway through the manufacturing process, each lattice contains a visible ridge midway through the length depicted in Figure 20.

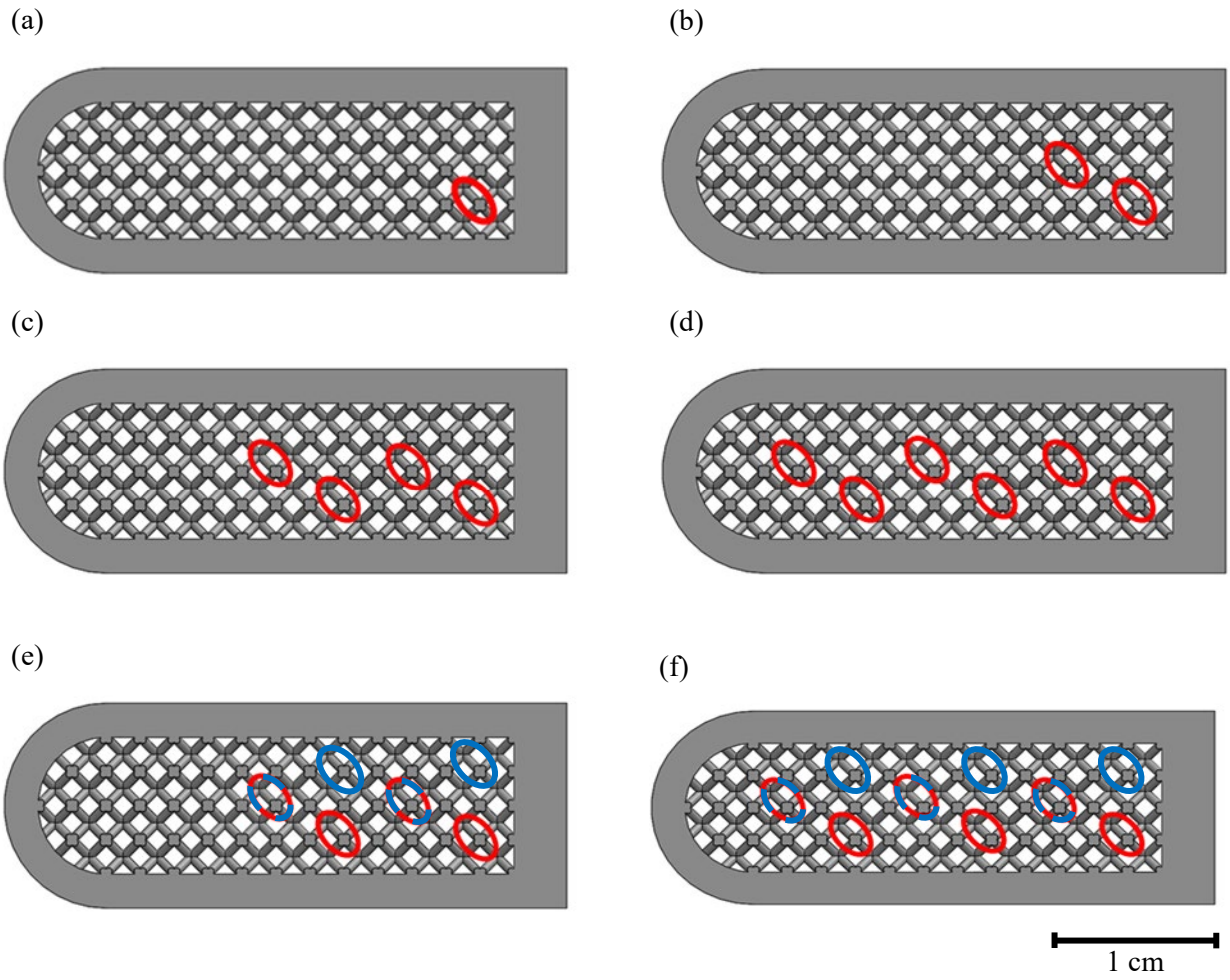

Figure 19: Locations of the missing struts for the physical lattice samples with (a) one, (b) two, (c) four, (d) six, (e) eight, and (f) twelve missing strut(s). The external missing strut locations are marked in red. The lattices with eight and twelve missing struts contain internal missing struts depicted in blue.

Table 5: Number engraved at the bottom of each lattice.

Number of Missing Struts	Engraved Number
0	037, 024, or 061
1	205
2	199
4	191
6	117
8	185
12	140

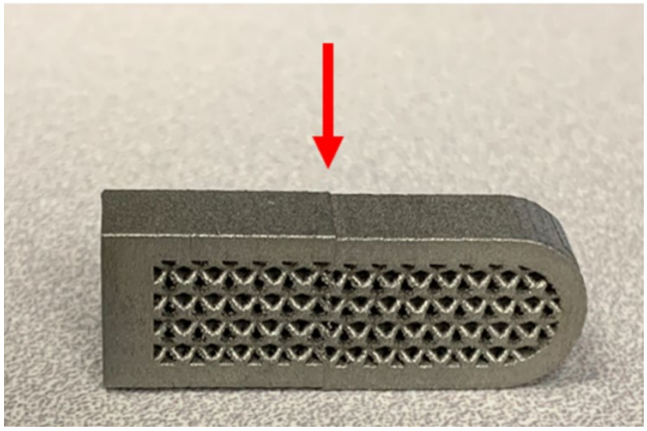

Figure 20: Due to stoppage during sample printing, every sample has a visible ridge at the same approximate location indicated by the red arrow.

3.3.2 EXPERIMENTAL SETUP AND DATA ANALYSIS

The experimental validation is conducted using an ACE RUS008 Resonant Ultrasound Spectrometer system by Alamo Creek Engineering [48]. The sample is placed between two identical lead-zirconate-titanate (PZT) ferroelectric transducers with radii of 2.5 mm, encapsulated in aluminum tubes with radii of 4.0 mm. The sample is positioned to have minimal support in order to mimic traction-free boundary conditions, as seen in Figure 21(a). The transducers and sample are held in place using a 3D printed stage (ABS with 20% fill), depicted in Figure 21(b); the design and material of the stage reduce acoustic transmission from one transducer to the other [49]. The system consists of three main components: (1) a power amplifier, (2) a charge amplifier, and (3) a Red Pitaya microcomputer with a Field Programmable Gate Array (FPGA). The charge amplifier is used to maintain the gain over a broad frequency range and to increase the signal-to-noise ratio in the receiving transducer. The power amplifier is an op-amp-based inverting amplifier used to achieve a 24 V output peak-to-peak. The Red Pitaya microcomputer contains a low-noise FPGA, designed to both generate a high frequency excitation and record the response with direct high-speed digitization. The digital-to-analog converter synthesizes a 125 MSPS sinusoidal sweep, while the analog-to-digital converter records and digitizes the voltage of the transducer preamp

output at 125 MSPS. Data acquisition is fully automated with a LabVIEW user interface. A complete description of the hardware and software can be found in Ref. [49].

(a)

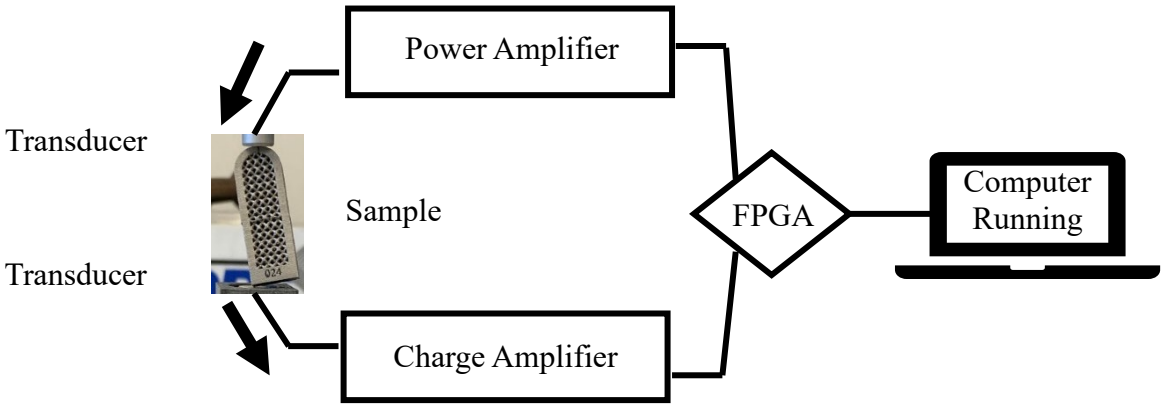

(b)

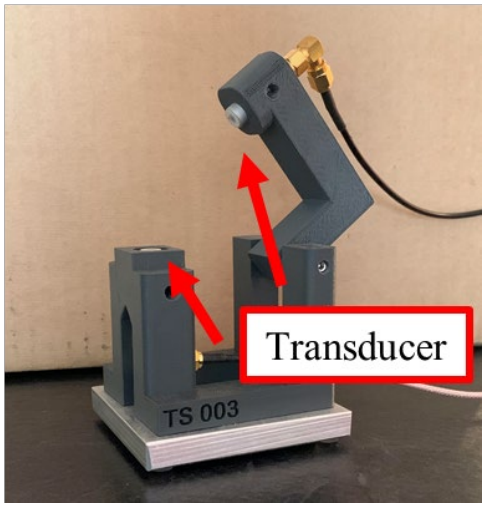

Figure 21: (a) A schematic of the RUS experimental setup adapted from Ref. [48] pictured with the lattice sample between two identical transducers; (b) Alamo Creek Engineering 3D printed stage (ABS with 20% fill) showing the location of the transducers.

For the experiments described in this section, each sample is insonified by a 10 – 310 kHz frequency sweep with a uniform 10 Hz step size, a 25 ms step duration, and an amplitude of 500 mV. The output is the total displacement spectrum of the sample recorded by the receiving transducer. Each sample is tested five consecutive times, with the sample being removed from in

between the two transducers and placed in the exact same position between tests. The transducer-sample contact locations are marked on the sample to ensure consistent placement. Testing the sample multiple times provides the opportunity to investigate the repeatability of the recorded spectra.

Post-processing and data analysis are accomplished in MATLAB R2020a and involve plotting the frequency spectrum and identifying the resonance frequencies. Each spectrum is first globally normalized to have a unit maximum amplitude and then smoothed using the *smooth* function in MATLAB, which applies a moving average filter with a selected span of five data points. Frequency peaks are found using *peakfinder* – a function available through the MATLAB file exchange – after setting a normalized amplitude threshold of 0.00025. Visual inspection of the identified peaks is conducted to categorize similar peaks across the five spectra according to closeness in peak frequencies and Q-factors. During this process, false peak indications resulting from limited frequency resolution are also removed. Repeatability is assessed by comparing the frequency and amplitudes of similar peaks. Feasibility of the method to identify the presence of missing struts is evaluated by calculating pairwise correlation coefficients across all samples using MATLAB's *xcorr* function on locally normalized spectra.

3.3.3 RESULTS

Measurement repeatability is assessed by comparing similar peaks across the five measurements. Table 6 provides a summary of the number of peaks found in each set for all nine samples. The results show that 79.9% or more peaks are found in three or more spectra for all samples, with at least 59.9% observed in all five spectra. For example, in sample "037", 210 peaks are found, out of which 21 (10.0%), 21 (10.0%), 16 (7.6%), 28 (13.3%), and 124 (59.0%) are found in one, two, three, four, and all five spectra, respectively. The peaks that are identified in only one or two of

the five spectra are likely a result of inconsistencies in sample placement and thus, applied contact pressure to the sample; in other words, since the amplitudes of excited modes can vary greatly based on specimen placement [49], some peaks may not rise above the selected threshold in different testing iterations.

The repeatability is further assessed by calculating the average and standard deviations for the frequency and amplitude of similar peaks, depicted graphically in Figure 22(a) for the pristine sample "037". Figure 22(b) shows a sample spectrum after global amplitude normalization and smoothing; Figure 22(c) depicts a zoomed in region of the five spectra denoting peaks considered *similar.* The variations in amplitude and frequency of similar peaks for all nine samples are summarized in Table 7. The standard deviations in resonance frequency of similar peaks range from 0 to 0.797 kHz, averaging 0.035 kHz, which is acceptable given the expected differences between resonance frequencies for defective and pristine samples. The standard deviations in amplitudes of similar peaks range from 0 to 0.455 a.u, averaging 0.053 a.u. Though this average appears small, the graphical depiction in Figure 22(a) and the range of maxima given in Table 7 suggest the need for a normalization technique that reduces the impact of amplitude differences across measurements. Hence, the frequency spectra are locally normalized following the procedure used for the numerical simulations, described in Sec. 3.2.1. This procedure enables more direct comparison of the resonance frequencies, which are deemed repeatable, while eliminating amplitude effects.

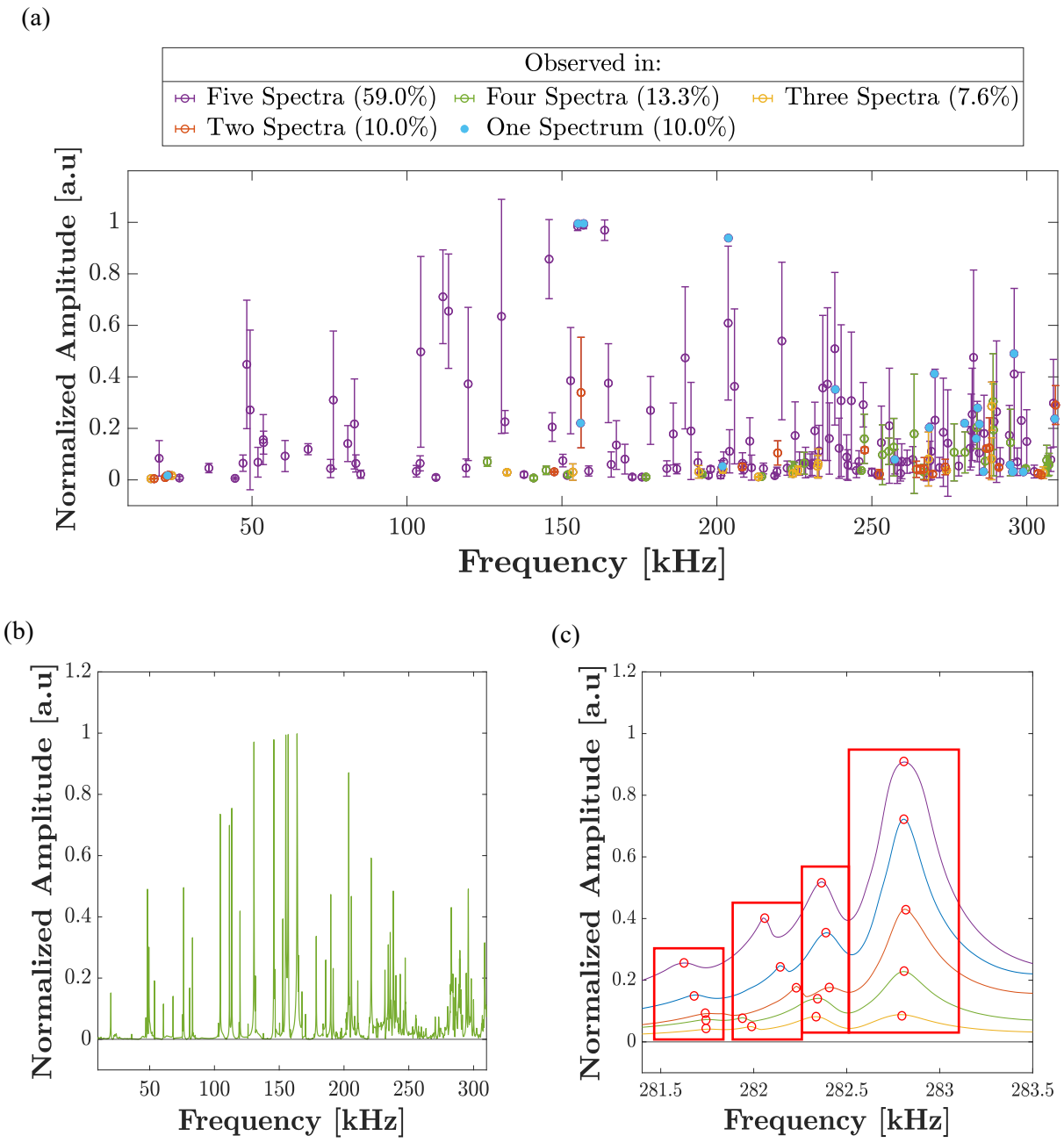

Figure 22: (a) Means and standard deviations for similar resonance frequency peaks in five experimentally measured spectra for sample "037"; (b) single spectrum for sample "037" after global amplitude normalization and smoothing; and (c) zoomed in region of the five spectra for sample "037" denoting peaks considered similar.

Table 6: Number of spectra containing similar peaks for each of the nine samples.

Number of Missing Struts	Total Number of Identified Peaks	Number of Peaks Identified in:				
		Five Spectra	Four Spectra	Three Spectra	Two Spectra	One Spectrum
"037"	210	124 (59.0%)	28 (13.3%)	16 (7.6%)	21 (10.0%)	21 (10.0%)
"024"	202	126 (62.4%)	21 (10.4%)	22 (10.9%)	19 (9.4%)	14 (6.9%)
"061"	183	126 (68.9%)	18 (9.8%)	12 (6.6%)	12 (6.6%)	15 (8.2%)
1	185	130 (70.3%)	15 (8.1%)	16 (8.6%)	13 (7.0%)	11 (5.9%)
2	204	150 (73.5%)	17 (8.3%)	16 (7.8%)	12 (5.9%)	9 (4.4%)
4	190	129 (67.9%)	20 (10.5%)	24 (12.6%)	11 (5.8%)	6 (3.2%)
6	216	129 (59.7%)	28 (12.9%)	20 (9.3%)	20 (9.3%)	19 (8.8%)
8	221	162 (73.3%)	20 (9.0%)	15 (6.8%)	14 (6.3%)	10 (4.5%)
12	223	159 (71.3%)	18 (8.1%)	15 (6.7%)	19 (8.5%)	12 (5.4%)

Table 7: Average and maximum standard deviations for the frequency and amplitude of similar peaks for each of the nine samples.

Number of Missing Struts	Standard Deviation Between Similar Peaks in Two or More Spectra			
	Average		Maximum	
	Frequency [kHz]	Amplitude [a.u]	Frequency [kHz]	Amplitude [a.u]
"037"	0.042	0.077	0.296	0.455
"024"	0.026	0.057	0.350	0.308
"061"	0.050	0.052	0.247	0.392
1	0.026	0.027	0.234	0.211
2	0.031	0.059	0.195	0.419
4	0.029	0.039	0.251	0.225
6	0.041	0.038	0.797	0.317
8	0.030	0.043	0.359	0.230
12	0.039	0.085	0.516	0.319

Next, we use a pairwise cross-correlation analysis to compare the experimentally measured spectra. For the five repeated measurements per sample, we report the mean and standard deviations of the calculated correlation coefficients. Specifically, the maximum correlation coefficient is determined for the five spectra of every two samples yielding 25 correlation coefficients values for every pair. The mean and standard deviation of each 25-correlation coefficient set for all nine samples are depicted in Figure 23, and the numerical values are listed in Table 8.

As expected, the largest correlation coefficient corresponds to the five repeated spectra for each sample with values ranging from 0.716 to 0.902. We attribute these low correlation coefficients to inconsistencies in sample positioning when repeating the measurements, which results in the amplitudes of some resonance modes not rising above the selected threshold, as previously described. The largest correlation coefficient between any two distinct samples is 0.448, corresponding to two pristine lattices “061” and “024”. The smallest is between lattices with two missing and twelve missing struts at 0.370. Examining Figure 23, a gradient of colors – as observed in the numerical *frequency domain* analysis (Sec. 3.2.3) – is not present. Therefore, unlike in the numerical simulations, it is not possible to clearly distinguish samples with and without missing struts. We note that the results of other similarity analyses such as dynamic time warping [44, 45], magnitude-squared coherence [46–50], different hypothesis testing [57], and energy calculations [58] yield a similar conclusion. We only report the cross-correlation analysis results here as they are among the most familiar and easiest to interpret among all the metrics used to differentiate between the samples.

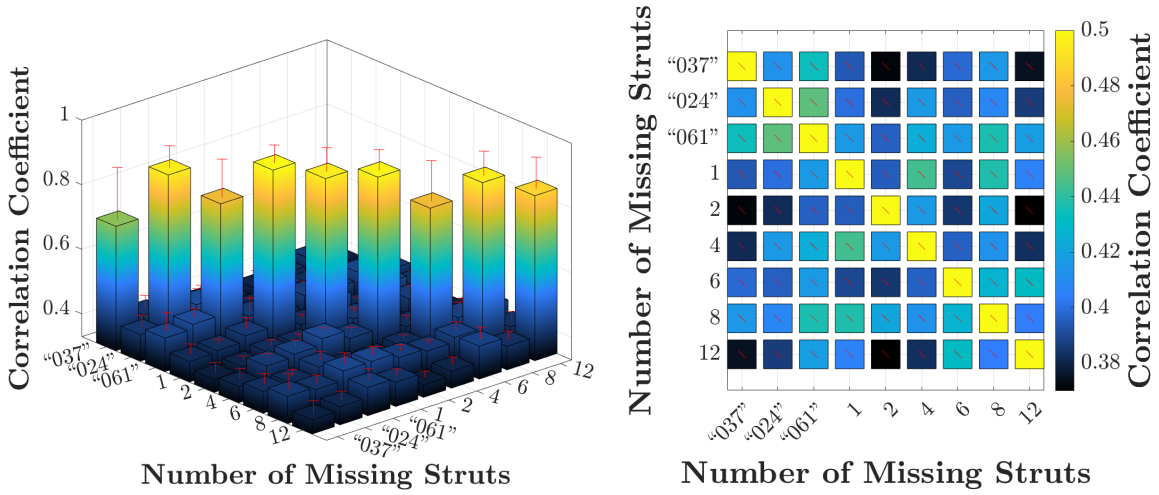

Figure 23: The mean and standard deviation of the maximum pairwise cross-correlation coefficients of the locally normalized frequency spectra from all samples.

Table 8: The mean and standard deviation of the maximum correlation coefficient of the locally normalized frequency spectra from all samples.

Number of Missing Struts									
	“037”	**“024”**	**“061”**	**1**	**2**	**4**	**6**	**8**	**12**
“037”	0.716 ±0.158	0.413 ±0.036	0.434 ±0.056	0.394 ±0.030	0.371 ±0.027	0.382 ±0.032	0.398 ±0.032	0.415 ±0.046	0.375 ±0.035
“024”	0.413 ±0.036	0.879 ±0.067	0.448 ±0.026	0.400 ±0.011	0.382 ±0.009	0.416 ±0.014	0.395 ±0.018	0.408 ±0.021	0.386 ±0.024
“061”	0.434 ±0.056	0.448 ±0.026	0.794 ±0.114	0.417 ±0.032	0.396 ±0.017	0.424 ±0.019	0.416 ±0.024	0.437 ±0.032	0.418 ±0.034
1	0.394 ±0.030	0.400 ±0.011	0.417 ±0.032	0.902 ±0.054	0.395 ±0.008	0.444 ±0.010	0.390 ±0.009	0.438 ±0.022	0.406 ±0.017
2	0.371 ±0.027	0.382 ±0.009	0.396 ±0.017	0.395 ±0.008	0.879 ±0.072	0.416 ±0.010	0.385 ±0.015	0.421 ±0.017	0.370 ±0.019
4	0.382 ±0.032	0.416 ±0.014	0.424 ±0.020	0.444 ±0.010	0.416 ±0.010	0.888 ±0.061	0.396 ±0.011	0.413 ±0.012	0.383 ±0.021
6	0.398 ±0.032	0.395 ±0.018	0.416 ±0.024	0.390 ±0.009	0.385 ±0.015	0.396 ±0.011	0.795 ±0.123	0.428 ±0.024	0.432 ±0.035
8	0.415 ±0.046	0.408 ±0.021	0.437 ±0.032	0.438 ±0.022	0.421 ±0.017	0.413 ±0.012	0.428 ±0.024	0.878 ±0.073	0.404 ±0.023
12	0.375 ±0.035	0.386 ±0.024	0.418 ±0.034	0.406 ±0.017	0.370 ±0.019	0.383 ±0.021	0.432 ±0.035	0.404 ±0.023	0.842 ±0.095

3.4 DISCUSSION: SIMLUATED VS. EXPERIMENTAL RESULTS

While simulated data clearly suggest the feasibility of RUS for differentiating pristine lattices from those with few missing struts, the experimental data is overall less encouraging. Although some of the observed correlations seem reasonable, some are counterintuitive. For example, the cross correlation of any of the pristine samples compared to a sample with twelve missing struts are near the lowest correlation values (coefficients = 0.375, 0.386, 0.418). On the other hand, the cross-correlation analysis shows that samples “024” and “037” are less similar (coefficient = 0.413) than sample “024” and the lattice with four missing struts (coefficient = 0.416) as well as sample “037” and the lattice with eight missing struts (coefficient = 0.415). This is surprising because both samples “024” and “037” are pristine samples.

A comparison between the simulated and experimental spectra for the same sample reveals that the corresponding spectra can be quite different. Figure 24 presents a comparison for sample “037”. The first peaks excited for the simulated spectrum and the experimental spectrum occur at 18.6 kHz and 19.81 kHz, respectively, a clearly identifiable difference of 1.20 kHz. In higher frequency ranges, such as 290 – 310 kHz, identifying similar peaks of the two spectra becomes much more challenging. The specific cause of the mismatch between simulated and experimental responses is unclear; however, the literature suggests a few potential sources of error. Some studies suggest strut dimensions in lattices can deviate from the CAD model: struts having ellipsoidal cross-sections as opposed to circular [53–56]; over- or under-sized strut diameters [53,57–60] depending on the orientation of the struts [53,57]; ‘strut waviness’, where the strut axes are not straight [61,62]; and increased diameter near the nodes of the lattices due to accumulated excess material [63,64]. Further, our specific samples have known geometrical discrepancies from the CAD model due to build failure, depicted in Figure 20. Porosity has also been reported on lattice

structures, a defect dependent on the inclination angle of the struts [71]. These seemingly small changes in the lattice geometries can cause shifts in resonance frequencies, leading to the inability to differentiate between lattices with a different number of missing struts.

Besides deviations from the design geometry, the material properties of as-printed lattices may differ from the material properties provided by the supplier [46], which are used for our numerical simulations. In a study conducted by NIST, sixteen CoCr disks – the same material of our printed lattices – were printed using the same hatch spacing and different hatch speeds. The densities of the resulting CoCr disks ranged from 7.00 to 8.21 g/cm^3, compared to the supplier reported density of 8.3 g/cm^3 [72]. Longitudinal wave speeds, estimated using pulse-echo time-of-flight measurements with a contact transducer, ranged from 4035 to 6123 m/s [72]. The corresponding Young's modulus, estimated from a range of Poisson's ratio of 0.25 – 0.35, ranges from 71 to 257 GPa. The material property sheet reports a Young's modulus of 190 – 220 GPa [46]. These discrepancies in material properties, if present in our lattice structures, would significantly impact the resonance response. We estimate the effect by conducting *eigenfrequency* analyses on a pristine lattice sample using the extreme values of elastic modulus and density reported by NIST for the CoCr disks. The first two resonance frequencies for each density-elastic modulus set relative to the values used in our numerical study are given in Table 9. A shift greater than 8 kHz is observed between the two extreme values.

Another potential source of error is the anisotropy of as-built parts when using powder bed fusion (PBF) and CoCr. The microstructure of as-built CoCr may contain cellular dendrites [73] – formed by fast cooling rates during the solidification process [67–69] – leading to the formation of unbalanced crystal phases [75]. In addition, samples built at a 45° angle with selective laser melting (SLM), a form of PBF, have shown poor mechanical properties (ultimate tensile strength,

yield strength, and elongation) when compared with samples built at a 0° and 90° angles [76]; the lattice structures in the current study have struts built at +/- 45°. Other reports link temperature gradients during the cooling process and residual stresses to anisotropy in the mechanical properties of as-built SLM CoCr structures [77]. Given the extent of research conducted on lattice samples, CoCr, and PBF, it is likely that the lattices in this study have undesirable features that obfuscate the differences in lattices with a varying number of missing struts.

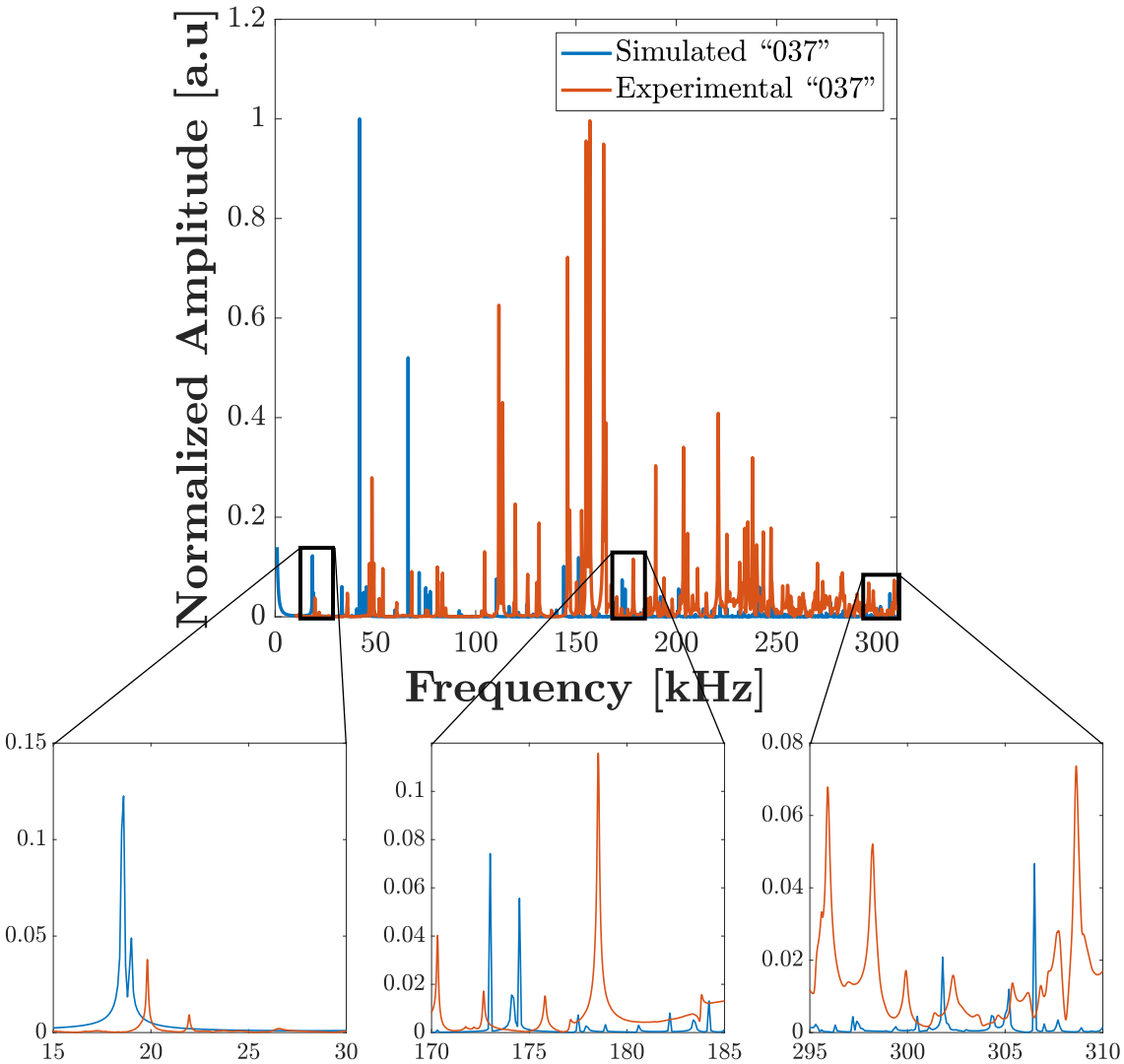

Figure 24: Globally normalized simulated spectrum of sample "037" from *frequency domain* analysis superimposed on the globally normalized experimental spectrum.

Table 9: Range of material properties estimated from densities and longitudinal wave velocities reported by NIST [72] and the corresponding first two resonance frequencies.

	Modulus of Elasticity [GPa]	Density [g/cm^3]	Poisson's Ratio	1st Resonance Frequency [kHz]	2nd Resonance Frequency [kHz]
Material Property Sheet	190	8.30	0.3	18.54	18.99
Lower Extreme	71	7.00	0.35	12.33	12.53
Upper Extreme	257	8.21	0.25	21.70	22.40

3.5 CONCLUSION

The analysis presented herein yielded mixed results regarding the feasibility of RUS to identify defects in complex lattice structures under traction-free BCs. Numerical simulations denote a clear distinction between pristine and defective lattices when the spectral amplitudes are normalized. However, experimentally, the method is less effective. A distinction cannot be made between pristine and defective lattices, even after local normalization of amplitudes. Multiple factors are hypothesized to affect the experimental results, which include but are not limited to, anisotropy of mechanical properties, deviations from the original design, and fluctuations in material properties. The promising nature of the numerical results suggests the technique should be validated on more reliable experimental samples.

CHAPTER 4 FIXED-FREE RESONANCE ULTRASOUND SPECTROSCOPY

This chapter investigates the suitability of an experimental configuration that employs a fixed-free boundary condition (BC) to identify the eigenfrequencies of lattices with a varying number of missing struts. First, one sample is tested three consecutive times to establish a baseline on the repeatability of the results. Then, a sensitivity analysis is carried out in both experimental and numerical simulation settings to determine sources of error that may cause variability in the experimental results (e.g., sample placement and probing positions). Finally, results are interpreted to determine whether a fixed-free BC is suitable for resonance frequency testing of lattice samples.

4.1 EXPERIMENTAL SETUP AND DATA ANALYSIS APPROACH

A piezoelectric ceramic disk (American Piezo Ceramics with a radius of 15.0 mm and a height of 12.0 mm) is glued (Phenyl Salicylate, 99%) to the bottom of each sample as the excitation source. The other side of the piezoelectric ceramic is epoxy glued to a cylindrical, steel backload approximately eight times heavier than the sample. This arrangement provides fixed-free BCs during testing. Figure 25(a) depicts one of the samples (together with the piezoelectric ceramic and the backload) used during experimentation and Figure 25(b) depicts how the sample configuration is recreated in numerical simulations.

(a) (b)

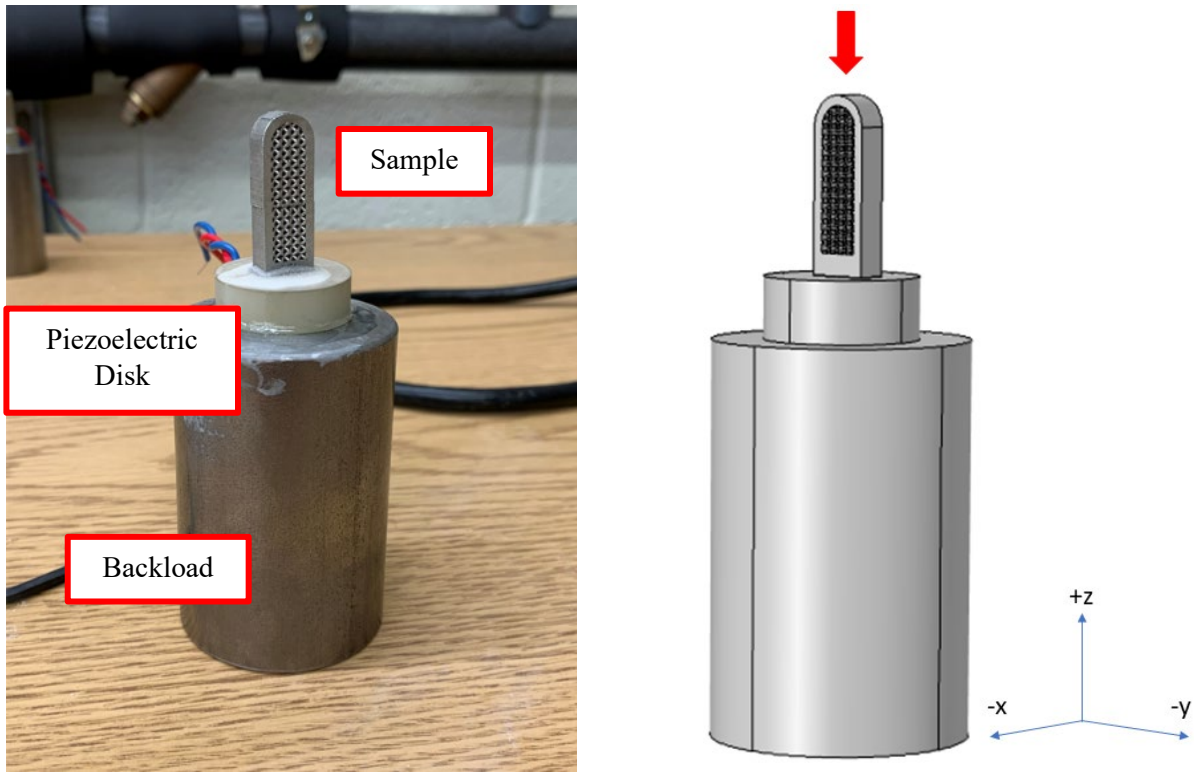

Figure 25: (a) Picture showing a lattice sample glued on a piezoelectric disk that is itself glued on a heavy steel backload; (b) CAD model of lattice used in numerical simulation including a piezoelectric disk and a heavy backload. The red arrow indicates the position where the particle velocity is typically tracked.

A schematic of the experimental setup is shown in Figure 26. The piezoelectric disk is driven by a single sinusoidal chirp that is generated by NI PXI 5422 arbitrary waveform generator and then amplified (50x) by a Tabor 9400 high-voltage amplifier. The frequency range varies from 1-100 and 1-200 kHz with a resolution of 10^{-4} kHz. The input driving amplitude is 0.1 V (or 5.0 V after amplification). The particle velocity is tracked using a Polytec OFV-525 laser Doppler vibrometer (LDV) with a sensitivity of 40 mm/s/V and digitized at 2 MHz using an NI PXIe-5170R acquisition card. The data acquisition process is fully automated using LabVIEW.

Post-processing and data analysis take place in MATLAB R2020a by first calculating the frequency spectrum of the recorded velocity using a fast Fourier transform. The spectra are

normalized by the maximum amplitude and smoothed using a Savitzky-Golay filter of polynomial order 3 and window length 501. Resonance peaks are identified using *peakfinder*, a peak detection function available through the MATLAB file exchange. The function identifies the frequency and amplitude of each peak by finding locations in the spectra with a zero slope; here, the amplitude threshold for peaks of interest in the normalized spectra is set at 0.002 a.u. The detected resonance peaks are then manually lined up with each other based on the shape of the peaks to calculate the mean and standard deviations of the frequency and amplitude of similar peaks. A detailed outline discussing how the peaks are manually lined up is discussed in Sec. 3.2.1.

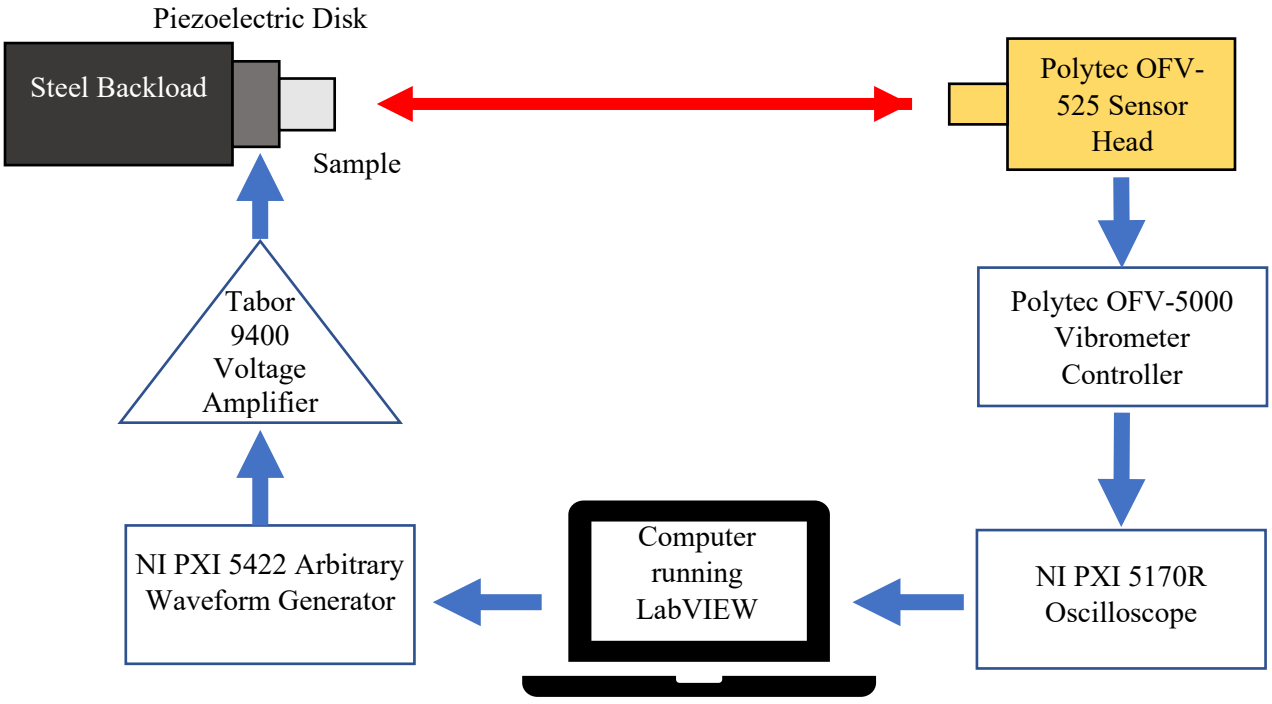

Figure 26: Schematic test setup of the fixed-free boundary condition.

4.2 BASELINE EXPERIMENTS AND RESULTS

In order to establish a baseline for repeatability of the results, a pristine lattice sample with the number “061” engraved at the bottom is tested three times using the configuration described in Sec. 4.1. Each experimental iteration entailed gluing and ungluing the lattice from the piezoelectric ceramic. The resonance frequency data for three LDV illumination positions are compared in Figure 27. The blue line corresponds with an arbitrary frequency spectrum from the set of three. Solid green markers indicate a peak that is observed in only one of the tests, hollow markers with horizontal and vertical error bars indicate the mean and standard deviation of a peak that was identified in at least two of the three spectra. Table 10 provides a summary of the number of peaks found in multiple spectra and the corresponding maximum shifts in resonance frequency. For tracking Position 1, which is at the top of the sample as depicted in Figure 27(a), 42 resonance peaks are detected, 11 of which are observed in only one of the three spectra (26.2%). The largest standard deviation in frequency when comparing similar peaks is 0.97 kHz. Position 2, depicted in Figure 27(b), is horizontally centered on a flat side of the sample, 25 mm from the bottom. In this position, there are 55 observable peaks, with 26 of the peaks (49.1%) appearing in only one of the three spectra. The largest standard deviation for this tracking position is 0.84 kHz. For Position 3, depicted in Figure 27(c), the illumination point is horizontally and vertically centered on a flat side of the sample. For this case, there are 40 observable peaks, where 10 of the peaks (25.0%) appear in only one of the three spectra. The largest standard deviation in frequency for similar peaks is 1.27 kHz.

The discrepancies in the number of detected peaks and in the resonance frequencies for similar peaks suggest variabilities in the experimental setup that must be quantified. Two potential sources of error are identified: (1) the placement of the sample on the piezoelectric disk and (2)

the position of LDV illumination point on the sample, i.e., the specific position on the sample that is being tracked by the LDV. The experimental setup requires that the sample be placed at the center of the piezoelectric disk; however, the baseline measurements did not employ a repeatability metric for sample placement. We hypothesize that off-center placement of the sample leads to nonuniform excitation, which disturbs the resonance modes. Furthermore, given the geometric complexity of the lattice samples, the particle velocity may significantly vary from point to point, which amplifies the importance of precise LDV placement. In the next section, a sensitivity analysis is conducted to evaluate the relative impact of these two sources of error through numerical simulations and controlled experimental testing. Subsequent sections consider only Position 1 given the similar conclusions drawn from the data at Positions 2 and 3.

(a)

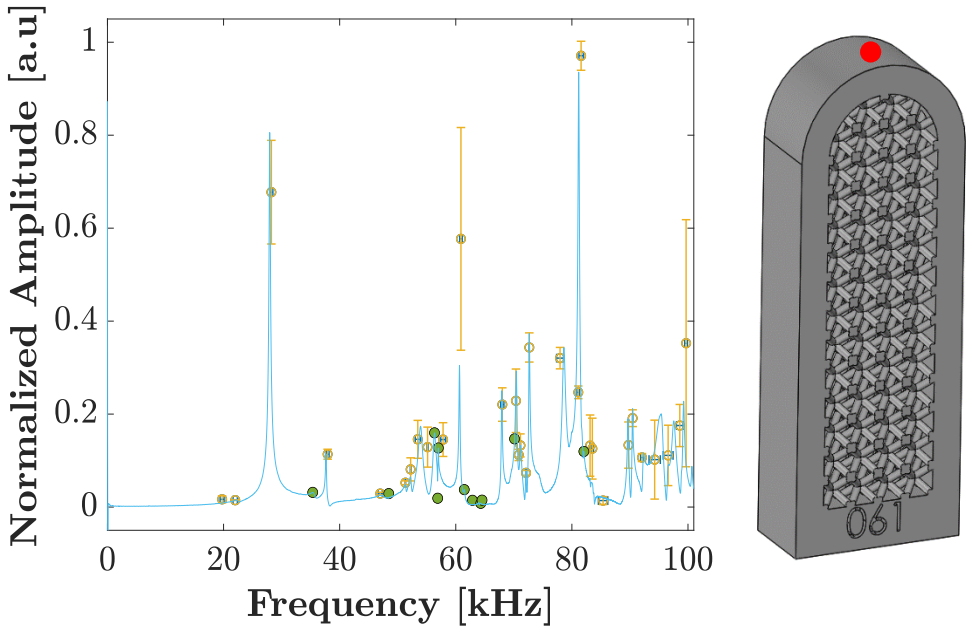

(b)

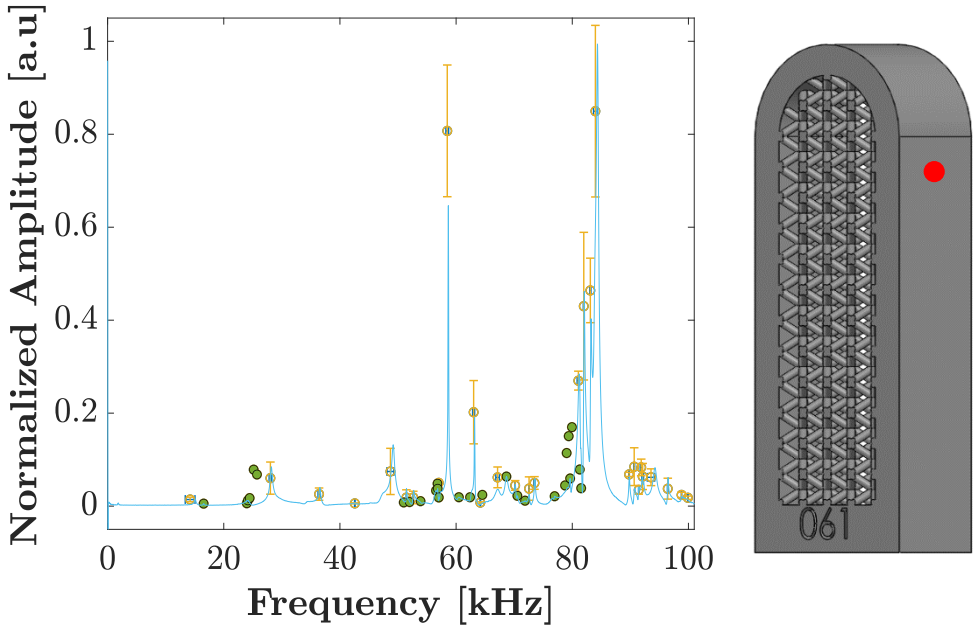

(c)

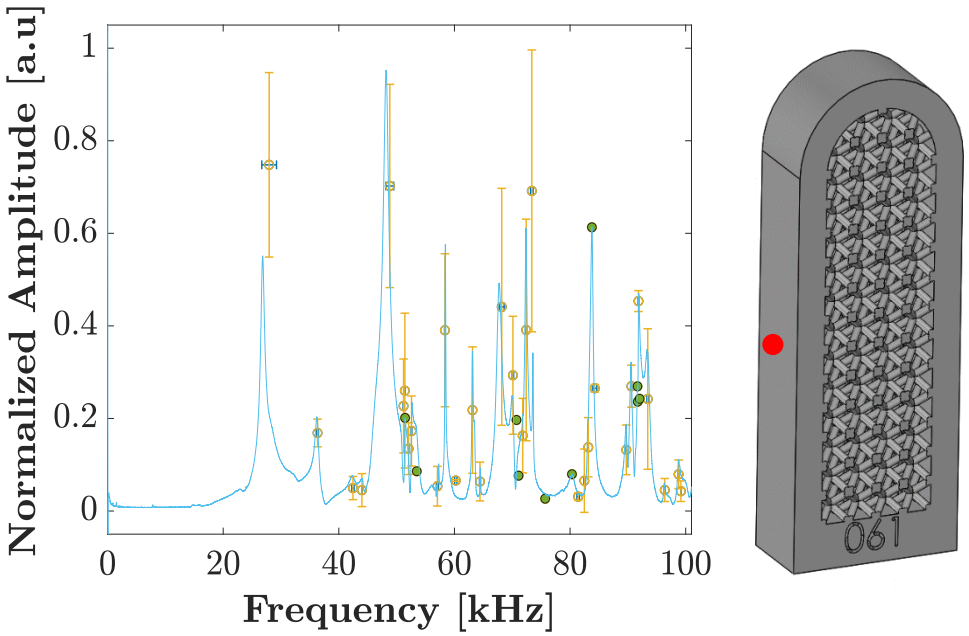

Figure 27: (a) Position 1, (b) Position 2, and (c) Position 3 where the particle velocity is tracked on the lattice sample during experimentation with a comparison of one of the corresponding spectra and the mean and standard deviation of similar peaks of three spectra.

Table 10: The number of spectra containing similar resonance peaks for each position in the baseline experiments and the largest standard deviation of frequencies for similar resonance peaks.

	Total Number of Peaks Observed	Number of Peaks Observed in Three Spectra	Number of Peaks Observed in Two Spectra	Number of Peaks Observed in One Spectrum	Largest Standard Deviation Between Similar Peaks [kHz]	Frequency Range for Largest Standard Deviation [kHz]
Position 1	42	23	8	11	0.97	93.56 – 95.37
Position 2	55	20	8	27	0.84	13.41 – 15.07
Position 3	40	17	13	10	1.27	26.83 – 29.33

4.3 NUMERICAL SIMULATIONS

Numerical simulations are conducted using COMSOL Multiphysics® 5.4, a finite element software. Section 3.2.1 provides a detailed explanation of the lattice samples used in the numerical simulations. In order to simulate the experimental setup for the fixed-free BC, we use a heavy steel backload and a piezoelectric disk for excitation, as depicted in Figure 25(b). The piezoelectric disk and backload are constructed within COMSOL after importing the corresponding lattices from SolidWorks. In order to effectively model the assembly, we take advantage of *Piezoelectric Device Physics* which implements the Solid Mechanics, Electrostatics, and Multiphysics interfaces into the numerical simulations. The piezoelectric disk is made of Lead Zirconate Titanate (PZT-5H), while the backload is assumed to be made of steel AISI 4340. The material properties used for the simulations are given in Table 11.

The mesh is created automatically using the 'physics-controlled mesh' option in COMSOL. Two different mesh sizes are used: a "fine" mesh size for the sample and a "coarser" mesh for the piezoelectric disk and backload. The coarser mesh size reduces simulation run time while maintaining the accuracy of the resonance response of the lattice, for which the meshing convergence is discussed in Sec. 3.2.1. We conduct a *Frequency Domain* analysis and simulate an

excitation in the z-direction, as depicted in Figure 25, using a sinusoidal electric potential with an amplitude of 100 V applied to the side of the piezoelectric disk that the sample is glued to, while the other side is grounded (0 V). The analysis is performed for a frequency range of 1 to 100 kHz with a step size of 0.1 kHz. The output is saved as velocity amplitudes for each of the frequency steps at the specified location (Position 1 in Figure 27(a)).

Table 11: Material properties for each of the geometries used in the numerical simulations.

Material Property	**Lattice (Cobalt Chrome)**	**Backload (Steel)**	**Piezoelectric Disk (PZT-5H)**
Density (g/cm^3)	8.3	7.85	7.5
Poisson's Ratio	0.3	0.28	-
Young's Modulus (GPa)	190	205	-
Elasticity Matrix (Pa)	-	-	127.2 80.2 84.7 0 0 0 127.2 84.7 0 0 0 117.4 0 0 0 23.0 0 0 SYM 23.0 0 23.5
Coupling Matrix (C/m^2)	-	-	0 0 0 0 17 0 0 0 0 17 0 0 -6.6 -6.6 23.2 0 0 0
Relative Permittivity	-	-	1704 0 0 0 1704 0 0 0 1434

4.3.1 INFLUENCE OF PARTICLE VELOCITY TRACKING POSITION

Four different LDV illumination points are considered on a pristine sample without engraving to study the effect of tracking position on the recorded frequency spectra. The selected probe positions, as shown in Figure 28, vary by at least +/- 1 mm in the x- or y-direction to simulate shifts in the tracking position that may result from human error during experimentation. The XY coordinates of the positions relative to Position 1 are provided in Table 12.

Unlike the experimental data, the simulated data can be directly plotted in the frequency domain and no smoothing or filtering is necessary. The mean and standard deviation of the amplitude and frequency of similar peaks in the four spectra are given Figure 29, where the frequency spectrum for position 1 if denoted with a blue solid line. As in Figure 27, a hollow marker indicates a peak that is observed in more than one spectrum and a solid marker indicates a peak that is observed in only one spectrum. For all peaks present in at least two of the spectra, the standard deviation of the resonance frequency is zero. However, out of the 111 detected resonance peaks, 29 (26.1%) are observed in only one out of the four spectra, as summarized in Table 13. This result confirms that the tracking position affects the recorded frequency spectrum, indicating that the LDV must be carefully placed during experimental testing. A controlled experiment to evaluate the minimum human error attainable in LDV placement is discussed in Sec. 4.4.2.

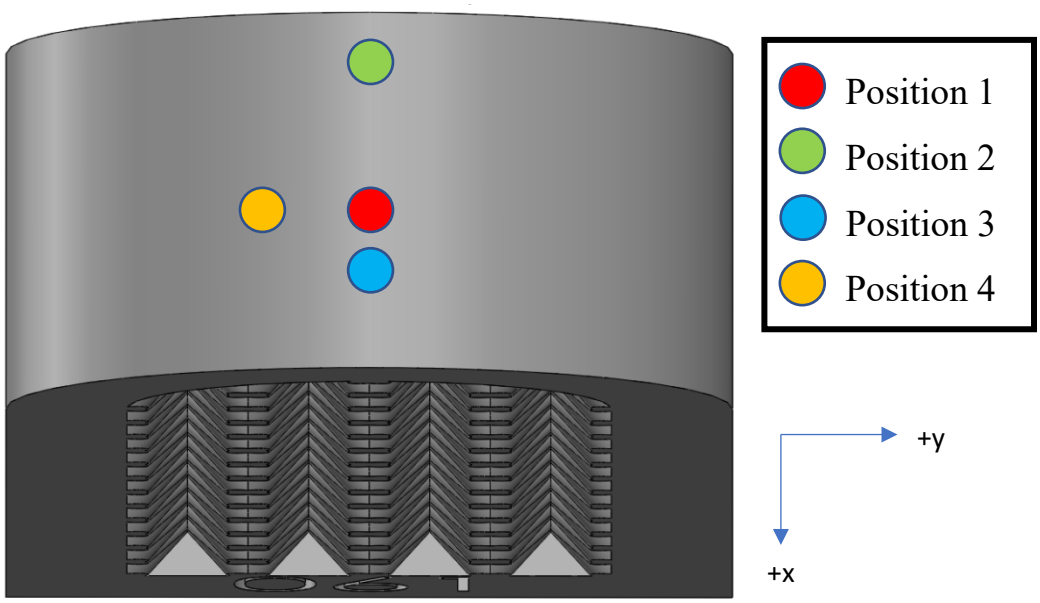

Figure 28: Top-down view of sample with indications of the four different particle velocity tracking positions tested during numerical simulations.

Table 12: XY coordinates for each of the particle velocity tracking positions as indicated by Figure 10.

	X coordinate [mm]	Y coordinate [mm]
Position 1	0	0
Position 2	-2.2273	0
Position 3	1	0
Position 4	0	-2

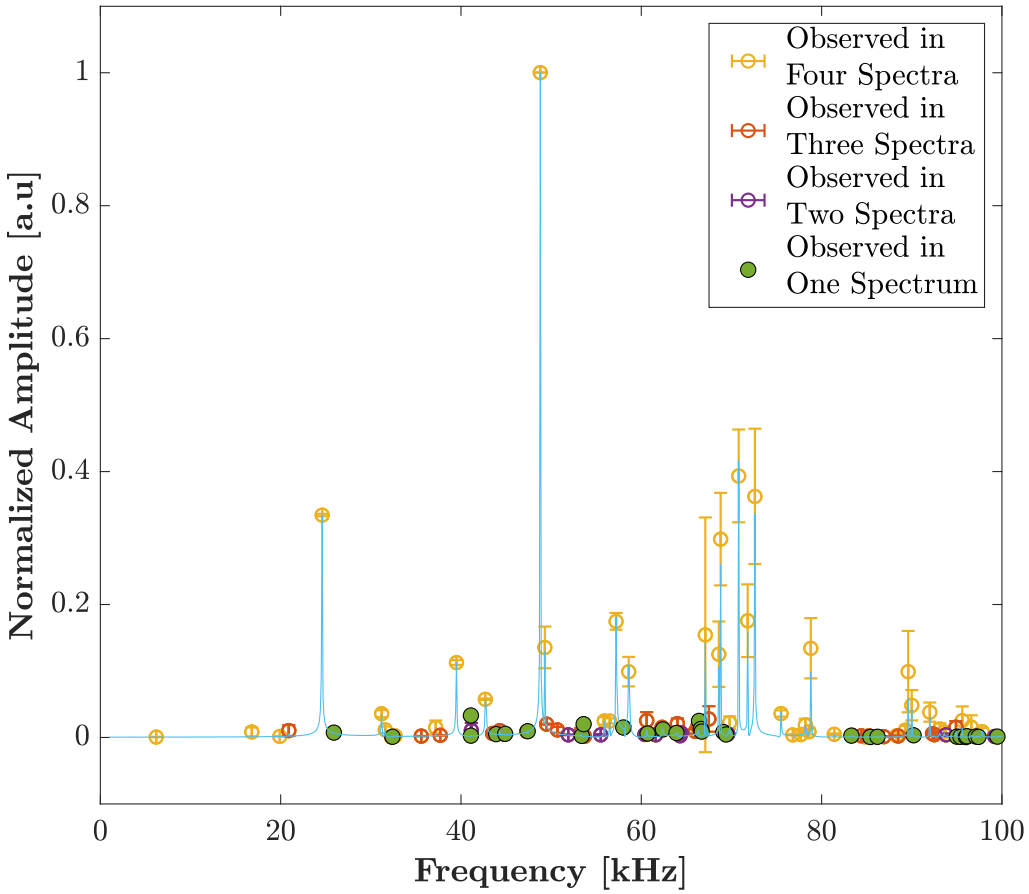

Figure 29: The mean and standard deviation for observed resonance peaks of the four particle velocity tracking positions as compared to the spectrum of Position 1.

Table 13: The number of spectra containing similar resonance peaks from evaluation of the influence of the particle velocity position on frequency spectra.

	Total Observed	Observed in Four Spectra	Observed in Three Spectra	Observed in Two Spectra	Observed in One Spectrum
Number of Peaks	111	42	29	11	29

4.3.2 INFLUENCE OF SAMPLE POSITION ON THE RECORDED FREQUENCY SPECTRA

Two different sample positions on the piezoelectric disk are numerically simulated to determine the influence of this factor on the observed response. The sample positions are given graphically in Figure 30 and the coordinates are specified in Table 14; the two selected positions differ by at least 2 mm in the x- and y-directions. The particle velocity tracking position on the sample is held constant for the two simulations.

The mean and standard deviation of the frequency and amplitude of each peak in the two recorded spectra are shown in Figure 31. As before, a solid marker (black) represents a peak that is observed in only one of the two simulations, and a hollow marker with error bars indicates a peak that is observed in both positions. Negligible shift in the resonance frequency is observed when comparing peaks present in both positions, with a maximum standard deviation of 0.14 kHz. However, out of the 107 peaks detected between the two spectra, only 21 (19.6%) are observed in both, as summarized in Table 15. Given the number of peaks that only occur in one test, it is apparent that shifting the sample position by even 2 mm results in a measurably distinct response.

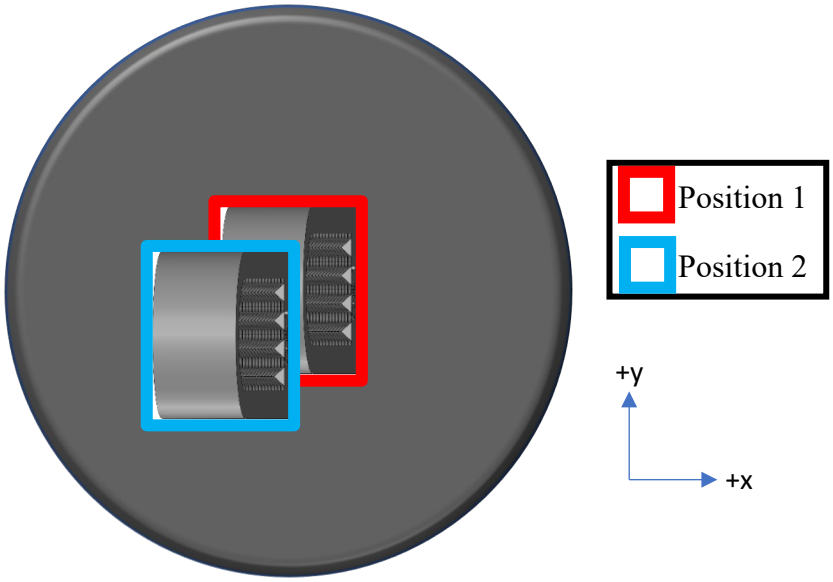

Figure 30: Sample positions on the piezoelectric disk tested during numerical simulations.

Table 14: XY coordinates for each of the sample positions indicated in Figure 12.

	X Coordinate [mm]	Y Coordinate [mm]
Position 1	0	0
Position 2	-2.0	-2.5

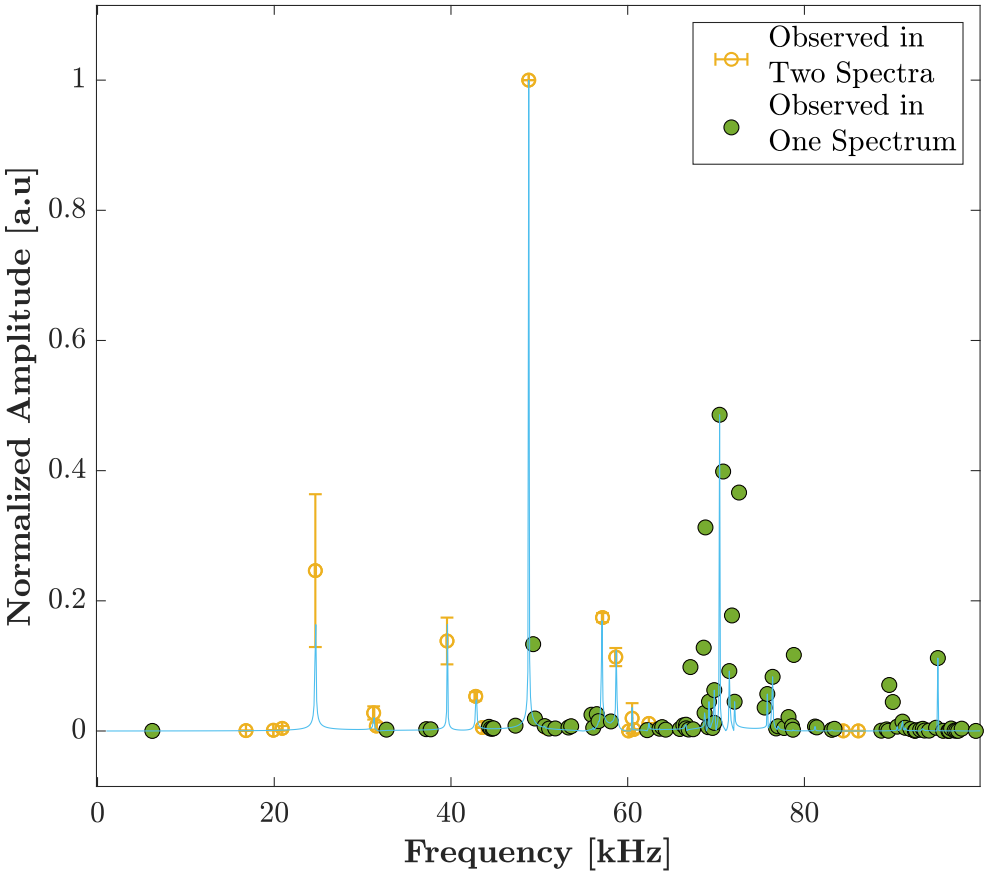

Figure 31: The mean and standard deviation of frequencies and amplitudes for observed resonance peaks of two different sample positions compared with the spectrum obtained from Position 1.

In order to elucidate the mechanisms that dictate the dissimilar response from a part placed in neighboring positions on the piezoelectric disk, we consider the vibrational modes of the disk at the excitation frequencies of interest. Generally, in disks with large diameter-to-thickness (d/t) ratio, the thickness extensional (TE) resonance mode dominates. As d/t decreases, the frequencies of the radial mode increase and eventually approach the disk's center frequency, negatively affecting the performance [40–43]. For small enough d/t (d/t < 20), the TE mode is completely

lost, resulting in more complicated modes that are strongly dependent on d/t [40–43]. The d/t ratio of the piezoelectric disk used here is 2.5, so complex modes near the center frequencies (71.0 kHz for the radial mode and 167.0 kHz for the TE mode) are expected. As depicted in Figure 32, at 24.7 kHz, the piezoelectric disk acts as a piston, whereas at 146.1 kHz, the piezoelectric disk displays more complex vibrational modes. The complexity in the mode shapes shows that small variations in the sample positioning on the disk will considerably affect the recorded resonance response. Based on these numerical results, Sec. 4.4 presents a controlled experiment to evaluate the minimum attainable error when implementing procedures that ensure repeatability in sample position.

Table 15: The number of spectra containing similar resonance peaks from evaluation of the influence of the sample position on frequency spectra.

	Total Observed	Observed in Two Spectra	Observed in One Spectrum
Number of Peaks	107	21	86

(a) (b)

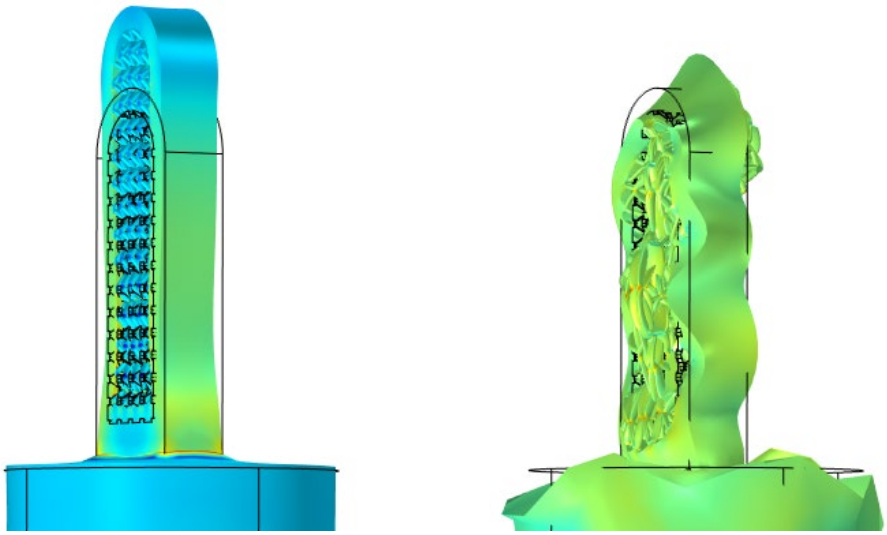

Figure 32: Numerically simulated mode shape of lattice sample and piezoelectric disk at (a) 24.7 kHz and (b) 146.1 kHz.

4.4 EXPERIMENTAL REPEATABILITY ANALYSIS

A lattice sample with six internal missing struts and six external missing struts with the engraving "140" is used to evaluate the repeatability of measurements under controlled conditions. First, we quantify the system error by repeating the measurements four times using identical test conditions. The subsequent sections evaluate human error effects on repeatability of LDV illumination point position and sample position on the piezoelectric disk. Each testing condition is evaluated four times with a frequency sweep from 1 to 200 kHz, split into 50 kHz sweeps.

4.4.1 BASELINE SYSTEM ERROR

A control experiment to quantify the system error is conducted by collecting data four consecutive times under identical test conditions. For these tests, the sample and position of the LDV illumination point are kept constant. The mean and standard deviation of the frequency and amplitudes of similar peaks in the resulting frequency spectra are plotted in Figure 33. 58 peaks are detected between the four spectra, with only one peak found in a single spectrum. Table 16 provides an overview of the number of peaks observed in one, two, three, and four spectra. For similar peaks, the largest standard deviation in frequency is 0.2 kHz, which will serve as the baseline for error quantification in subsequent measurements.

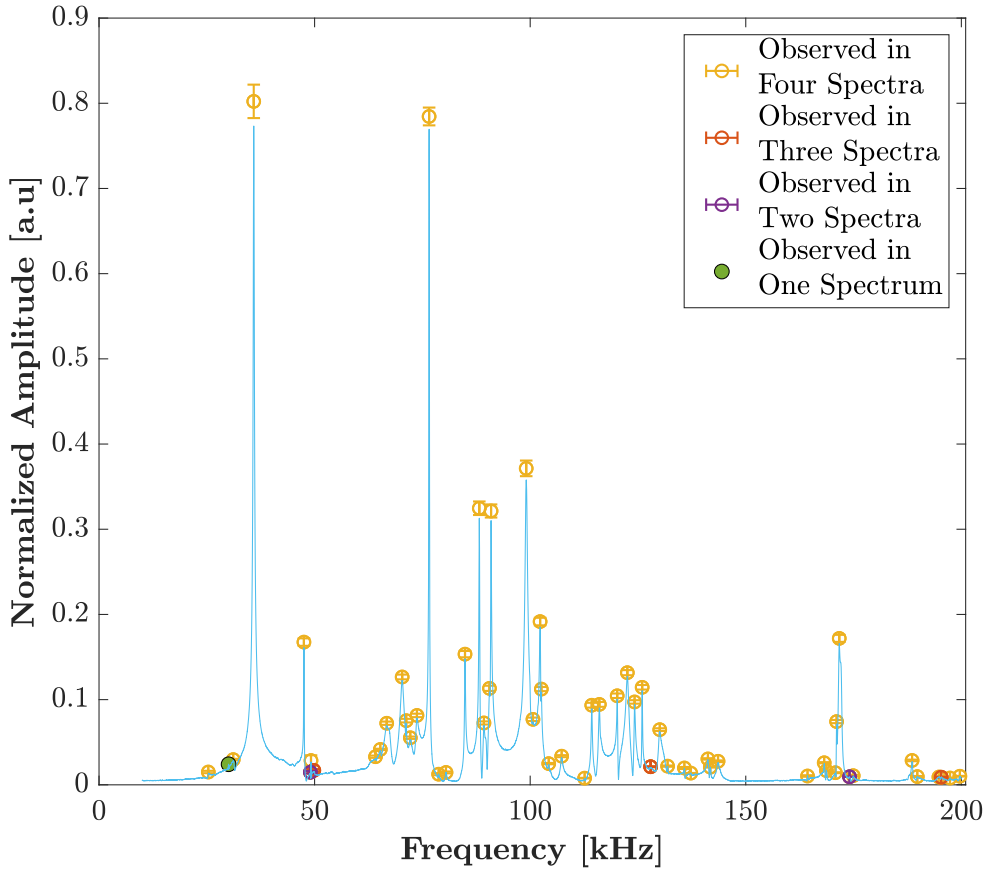

Figure 33: Mean and standard deviation of amplitudes and frequencies of similar peaks compared with one of the collected spectra to quantify the system error in a fixed-free experimental setup from 1 to 200kHz.

Table 16: The number of spectra containing similar resonance peaks in the control experiment.

	Total Observed	Observed in Four Spectrum	Observed in Three Spectrum	Observed in Two Spectrum	Observed in One Spectrum
Number of Peaks	58	52	3	2	1

4.4.2 REPEATBILITY OF THE LASER ILLUMINATION POINT POSITION

Experiments are conducted to quantify the minimum attainable error when attempting to place the LDV illumination point in the same position for four consecutive tests. A cross is marked with a pencil at the top of the sample and the LDV illumination point is manually aligned with the cross prior to each test. After each test, the LDV is turned off and the sample/disk/backload assembly is

removed from its testing position. The remaining components of the experimental setup remain constant across measurements. The mean and standard deviation of the frequencies and amplitudes of similar peaks observed in the four collected spectra are plotted in Figure 34. There are 106 identifiable peaks total, five of which are only found in one of the four spectra; a summary is given in Table 17.

The largest standard deviation for the recorded frequencies is 0.47 kHz, which exceeds the system error discussed in Sec. 4.4.1 (0.2 kHz). The number of peaks observed in a single spectrum (5 peaks) also exceeds the system error, where only one such peak is present. When these metrics are compared to the baseline test (Sec. 4.2), a smaller standard deviation (0.47 kHz vs. 0.84-1.27 kHz) and less peaks observed in only one spectrum (5 vs. 10-27 peaks) are attained, which can be attributed to the systematic placement of the LDV illumination point proposed in this section. Note that the baseline measurements were performed over a smaller frequency range. In summary, providing a guideline for repeatable placement of the LDV illumination point reduces the measurement error, though the minimum attainable error is still larger than that of the system.

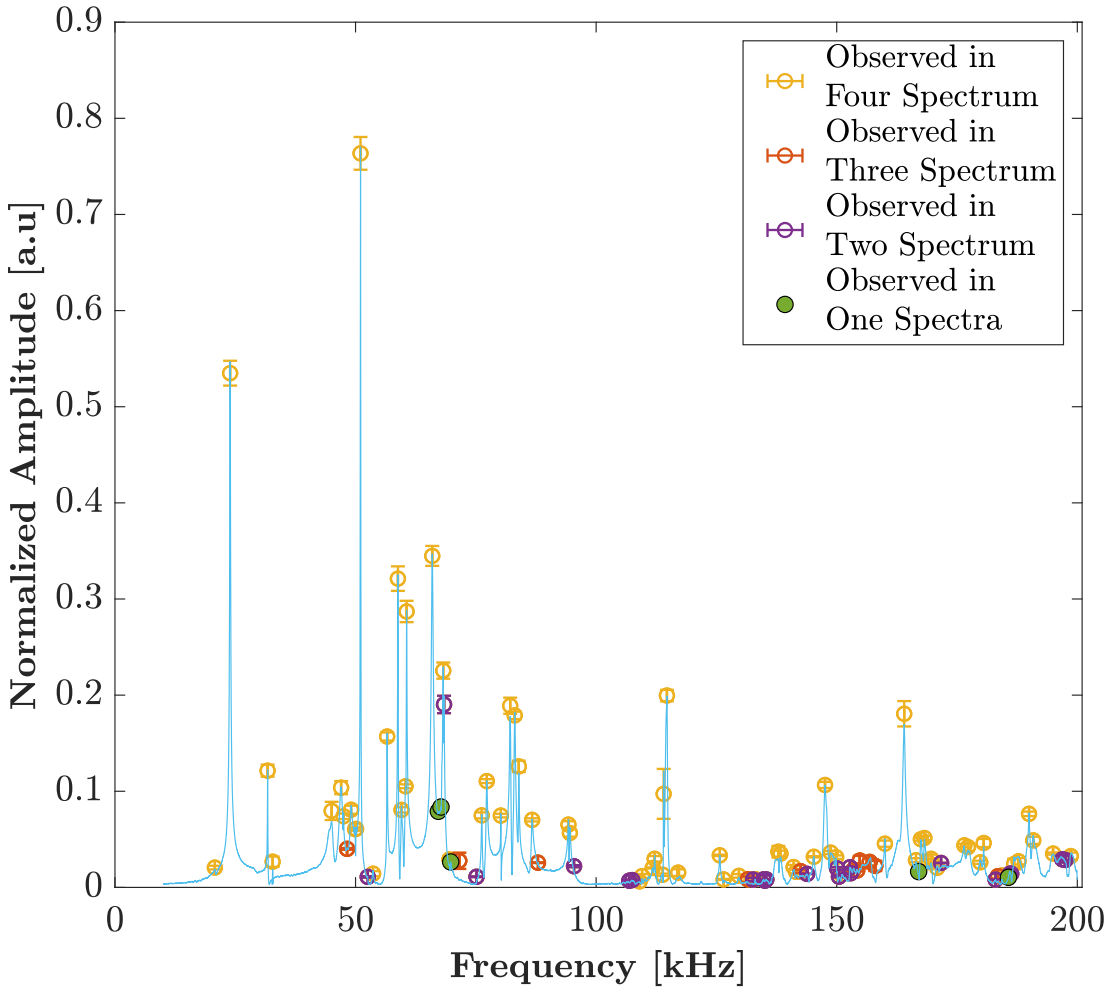

Figure 34: Mean and standard deviation of amplitudes and frequencies of similar peaks from four spectra, compared with one of the collected spectra, to test the repeatability of placing the LDV illumination point in the same position for 1 to 200 kHz.

Table 17: The number of spectra containing similar peaks in the repeatability testing of the LDV illumination point on the sample.

	Total Observed	Observed in Four Spectrum	Observed in Three Spectrum	Observed in Two Spectrum	Observed in One Spectrum
Number of Peaks	106	69	11	21	5

4.4.3 REPEATABILITY OF THE SAMPLE PLACEMENT ON THE PIEZOELECTRIC DISK

The results in this section quantify the repeatability of sample placement on the piezoelectric disk for four consecutive measurements. The lattice sample is glued to the piezoelectric disk, tested, un-glued, and then re-glued prior to the next round of testing. The drying time of the glue is one hour and maintained constant across measurements. To maximize repeatability, a template is used to mark the desired sample position, as shown in Figure 35. The means and standard deviations of the frequencies and amplitudes of similar peaks for the four recorded spectra are plotted in Figure 36. Table 18 provides a summary of the number of spectra that contain similar peaks. One key observation is that out of the 133 peaks detected across all four frequency spectra, 35 are found in only one of the four spectra (vs. 1 peak in the control experiment). The largest standard deviation in frequency for similar peaks is 0.34 kHz (vs. 0.2 kHz in the control experiment).

When comparing these results to the baseline testing, providing a template for sample placement reduces the standard deviation between similar peaks (0.34 kHz vs. 0.84-1.27 kHz). The baseline testing, however, has less peaks that are only observed in one spectrum (10-27 peaks) than this analysis for the sample placement (35 peaks). This result may relate to the extended frequency range employed in this section (1-200 kHz) compared to the baseline testing (1-100 kHz). Relative to the LDV illumination point placement, the minimum attainable error in sample placement on the piezoelectric disk results in more peaks that are observed in only one spectrum (35 vs. 5 peaks), but lower standard deviation for similar peaks (0.34 kHz vs. 0.47 kHz).

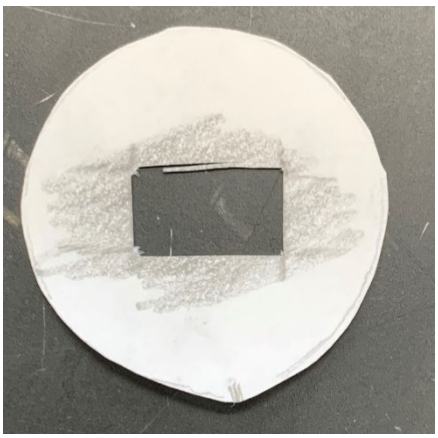

Figure 35: Template used to minimize the amount of movement of the sample on the piezoelectric disk in between tests.

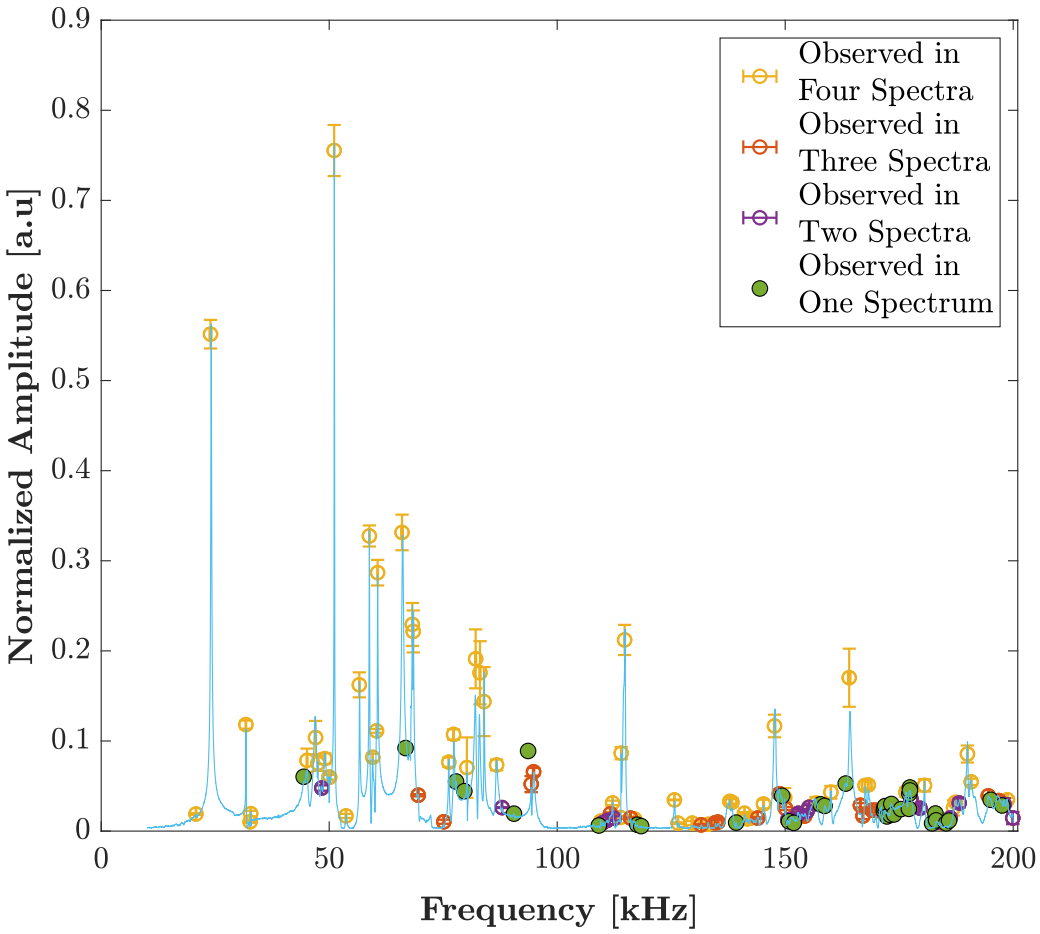

Figure 36: Mean and standard deviation of amplitudes and frequencies of similar peaks from four spectra, compared with one of the collected spectra, to test the repeatability of placing the sample in the same position for 1 to 200 kHz.

Table 18: The number of spectra containing similar resonance peaks in the repeatability testing of the sample position on the piezoelectric disk.

	Total Observed	Observed in Four Spectrum	Observed in Three Spectrum	Observed in Two Spectrum	Observed in One Spectrum
Number of Peaks	133	59	22	17	35

4.5 CONCLUSION

The sensitivity analysis presented illustrates the challenges associated with accurately obtaining the resonant response of a sample under fixed-free BCs. Numerical simulations indicate that shifts in the position of the sample on the piezoelectric disk and in the position of the LDV illumination point will result in differing responses for the same sample. Although providing guidelines for repeatable placement of the sample and the LDV illumination point reduces the error in measurement repeatability, the error magnitudes remain above the expected differences between pristine and defective lattices. Furthermore, with a fixed-free BC, certain resonance frequencies are not excited which may hinder the detectability of specific geometric variations (i.e., missing struts in certain locations). Lastly, a fixed-free BC was considered given the availability of the experimental set up during the testing period; however, subsequent measurements using the free-free BC setup proved more efficient and repeatable.

CHAPTER 5 CONCLUSIONS AND RECOMMENDATIONS

The goal of this work was to determine the feasibility of using RUS to identify defects in additively manufactured lattice structures in the form of missing struts. Numerical simulations provided promising results which suggested samples can be distinguished based on the number of missing struts. The *eigenfrequency* analysis, corresponding to the free vibration of the samples, differentiated between a pristine lattice and lattices with an increasing number of missing struts. Though the locations of the missing struts impacted the absolute differences in eigenfrequencies, aggregate data from five sets of locations suggested a linear increase in the range of eigenfrequency differences for 0-12 missing struts across all cases. Through this analysis, critical modes were identified at which eigenfrequency differences start to more significantly increase. Although these findings are specific to the lattice geometry studied here, similar analysis to identify critical modes could generally provide a useful guide in experimental design. Analysis also shows that the engraved numbers used for sample tracking were found to have a negligible effect on the eigenfrequency differences relative to the changes observed due to missing struts; thus, subsequent analysis was conducted on samples identical to the physical lattices with engraved numbers.

The *eigenfrequency* analysis was computationally efficient and provided encouraging results pertaining the ability of RUS to identify missing struts. Hence, we followed with a *frequency domain* analysis with forced vibration conditions to mimic the experimental configuration more closely. Preliminary inspection of the frequency spectra for simulated pristine lattices with different number engravings revealed negligible differences in resonance frequencies, as expected from the *eigenfrequency* analysis. However, amplitude differences were observed for each peak. Thus, any correlation metric used to compare the frequency spectra of the nine simulated samples had to eliminate the impact of amplitude variations. As such, a local

normalization technique was proposed. Then, the pairwise cross correlation coefficients for the nine samples were calculated. The results showed a clear distinction between pristine and defective lattices, with a gradual decrease in correlation coefficient as the number of missing struts increased.

Although the numerical simulations were promising, the corresponding traction-free BC experiments fell short. A distinction could not be made between the samples, even after the local normalization technique was applied. The shortcomings in experimental testing are hypothesized to result from differences in the mechanical and geometrical properties of the lattices relative to those used in the numerical simulations. These properties include, but are not limited to, micro- and macroscopic anisotropy, geometrical deviations from the CAD model, and changes in material properties, all of which are widely reported in the literature for the material studied herein when used in powder bed fusion processes.

Finally, we evaluated the feasibility of an alternative experimental configuration with fixed-free boundary conditions. This approach proved ineffective in both numerical simulations and experimental validation. A sensitivity analysis was numerically conducted to evaluate the impact of repeatability in the location of the sample on the piezoelectric disk and the LDV illumination point, both of which were shown to measurably impact the frequency response. The corresponding experimental validation of the sensitivity analysis showed that human error in placing both the sample on the piezoelectric disk and the LDV illumination point on the sample will lead to unrepeatable results and the inability to distinguish between the pristine and defective lattices.

The results presented in this thesis are encouraging and provide a baseline for feasibility of RUS in detecting geometrical defects in geometrically complex lattice structures. In order to

improve the robustness of the method, and further verify the validity of the numerical results, the following recommendations are provided for future work:

- Numerical Simulations
    - Consider the implications of the linear-elastic, homogeneous model by increasing the complexity of the material system simulated. For example, including anisotropy in the mechanical properties or evaluating the impact of porosity throughout the volume.
- Experimental Testing
    - Perform experimental validation on additively manufactured samples with simpler geometries.
    - Consider complex geometries with more reliable, or otherwise verified, mechanical properties.

APPENDIX: LOCATIONS OF MISSING LATTICE STRUTS

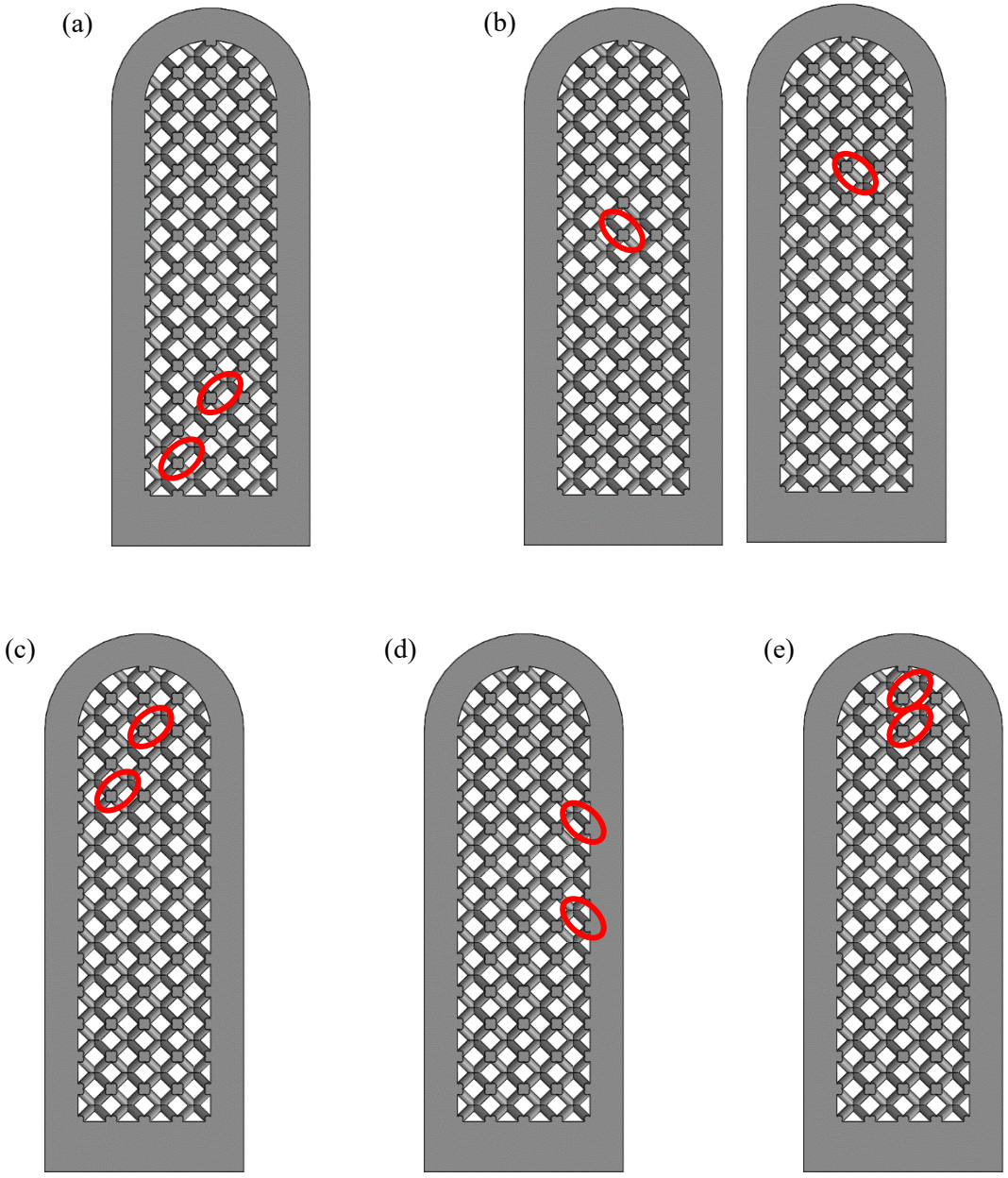

Figure 37: A lattice with two missing struts at the locations depicted in (a)-(e) sequentially labeled case 1-5. Missing struts are located on the outer layer of the lattice structure for all cases. Note that (b) case 2 has one missing strut on each side of the sample.

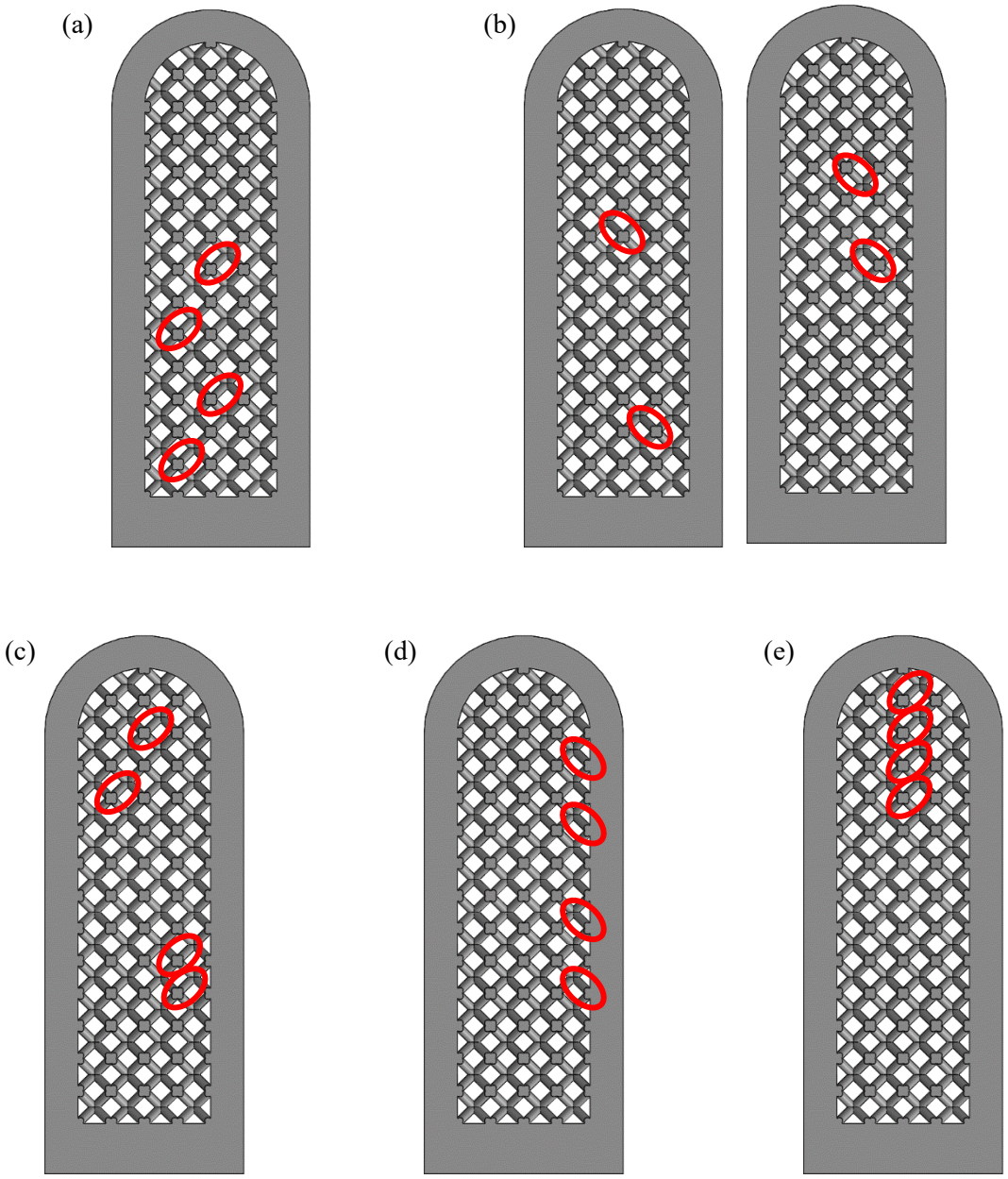

Figure 38: A lattice with four missing struts at the locations depicted in (a)-(e) sequentially labeled case 1-5. Missing struts are located on the outer layer of the lattice structure for all cases. Note that (b) case 2 has two missing struts on each side of the sample.

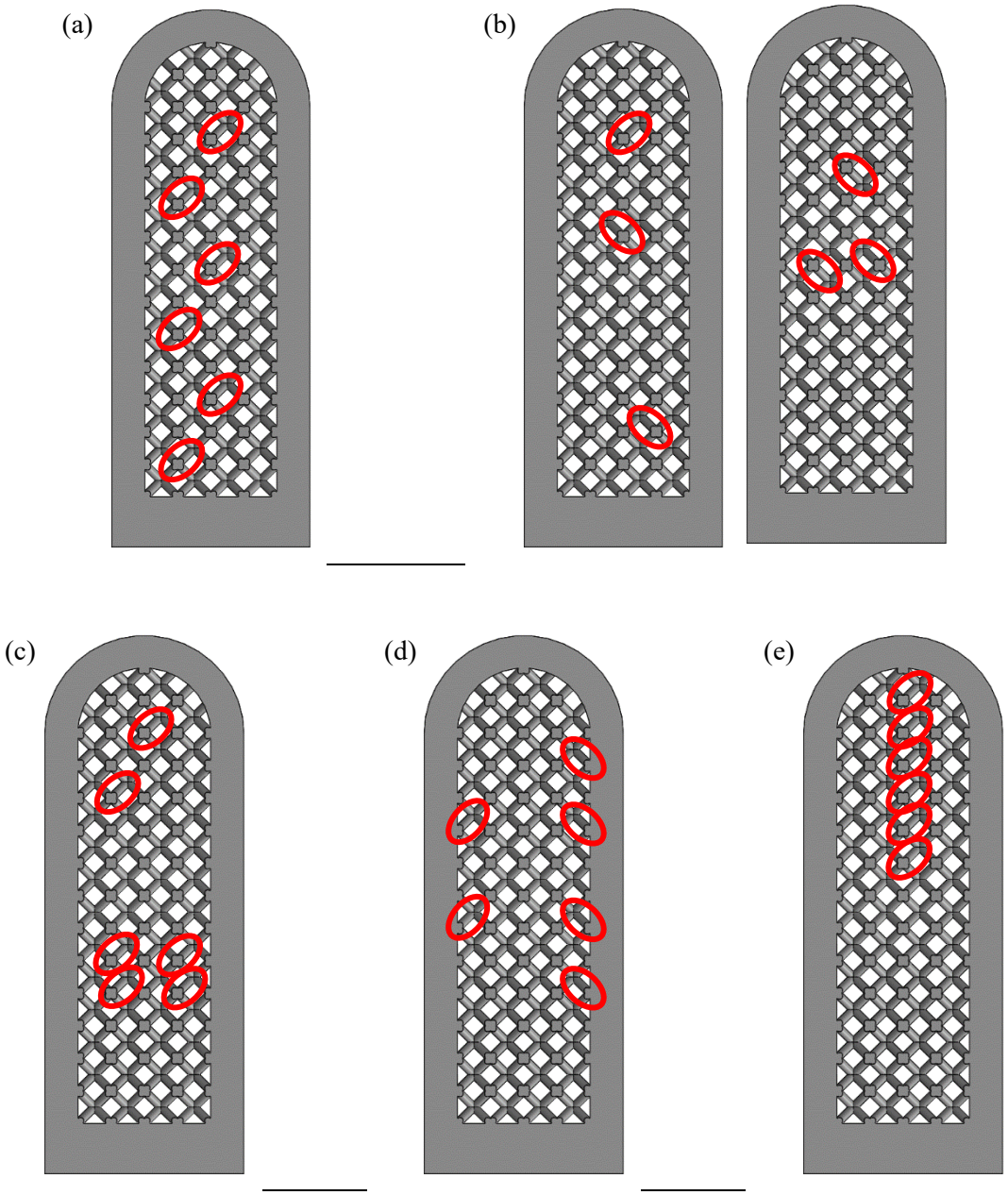

Figure 39: A lattice with six missing struts at the locations depicted in (a)-(e) sequentially labeled case 1-5. Missing struts are located on the outer layer of the lattice structure for all cases. Note that (b) case 2 has three missing struts on each side of the sample.

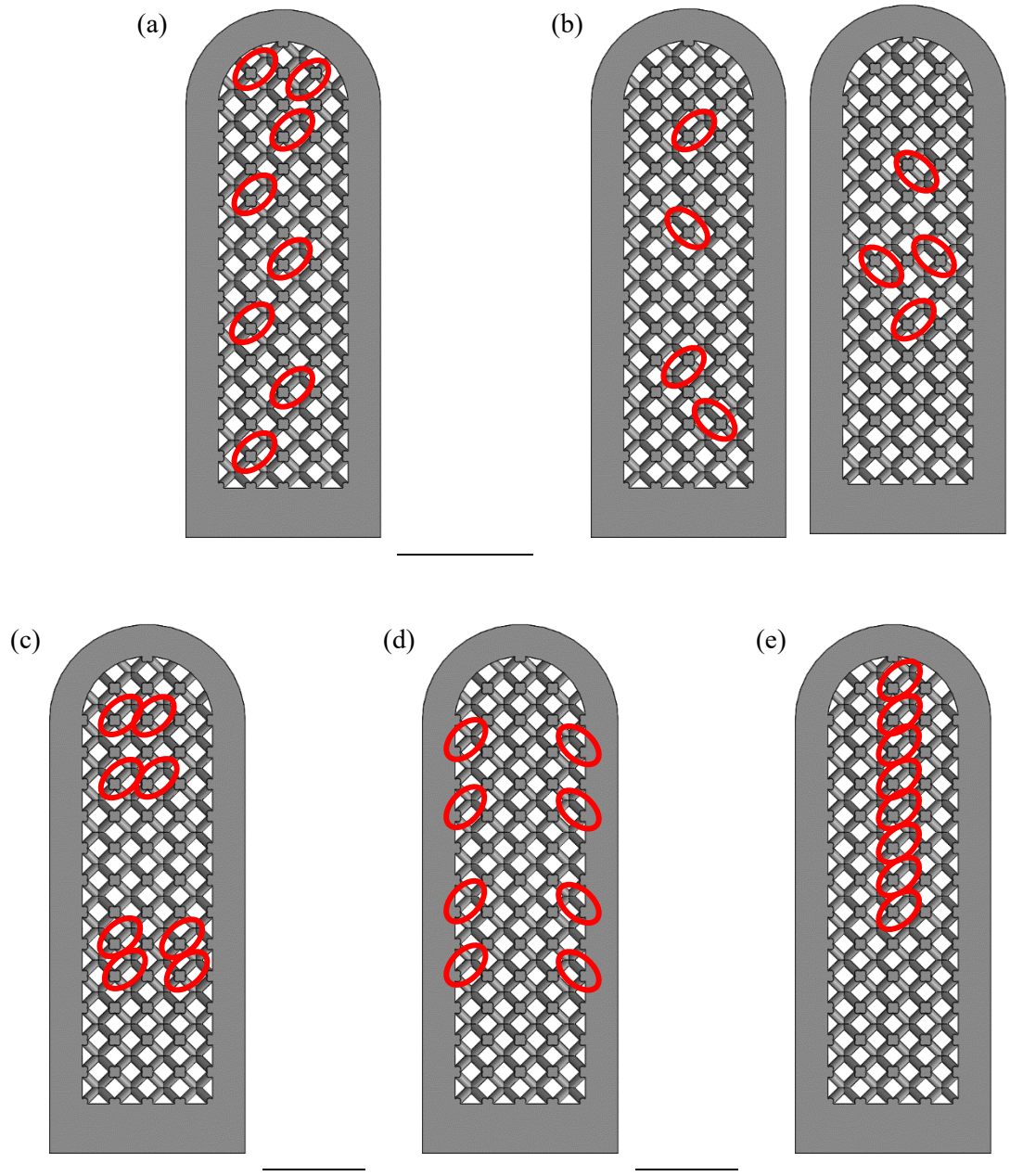

Figure 40: A lattice with eight missing struts at the locations depicted in (a)-(e) sequentially labeled case 1-5. Missing struts are located on the outer layer of the lattice structure for all cases. Note that (b) case 2 has four missing struts on each side of the sample.

BIBLIOGRAPHY

[1] M. Seifi *et al.*, "Progress Towards Metal Additive Manufacturing Standardization to Support Qualification and Certification," *JOM*, vol. 69, no. 3, pp. 439–455, 2017, doi: 10.1007/s11837-017-2265-2.

[2] L. Koester, H. Taheri, L. J. Bond, D. Barnard, and J. Gray, "Additive manufacturing metrology: State of the art and needs assessment," *AIP Conf. Proc.*, vol. 1706, no. February, 2016, doi: 10.1063/1.4940604.

[3] S. A. M. Tofail, E. P. Koumoulos, A. Bandyopadhyay, S. Bose, L. O'Donoghue, and C. Charitidis, "Additive manufacturing: scientific and technological challenges, market uptake and opportunities," *Mater. Today*, vol. 21, no. 1, pp. 22–37, 2018, doi: 10.1016/j.mattod.2017.07.001.

[4] B. M. Sharratt, "Non-Destructive Techniques and Technologies for Qualification of Additive Manufactured Parts and Processes: A Literature Review," Sharratt Research & Consulting Inc., Contract Report DRDC-RDDC-2015-C035, 2015.

[5] C. Mandache, "Overview of non-destructive evaluation techniques for metal-based additive manufacturing," *Mater. Sci. Technol.*, vol. 35, no. 9, pp. 1007–1015, 2019, doi: 10.1080/02670836.2019.1596370.

[6] E. Todorov, R. Spencer, S. Gleeson, M. Jamshidinia, and S. M. Kelly, "America Makes: National Additive Manufacturing Innovation Institute (NAMII)," Defense Technical Information Center, Fort Belvoir, VA, AFRL-RX-WP-TR-2014-0162, Jun. 2014. doi: 10.21236/ADA612775.

[7] J.-W. Kim and S. Park, "Magnetic flux leakage–based local damage detection and quantification for steel wire rope non-destructive evaluation," *J. Intell. Mater. Syst. Struct.*, vol. 29, no. 17, pp. 3396–3410, Oct. 2018, doi: 10.1177/1045389X17721038.

[8] Q. Y. Lu and C. H. Wong, "Additive manufacturing process monitoring and control by non-destructive testing techniques: challenges and in-process monitoring," *Virtual Phys. Prototyp.*, vol. 13, no. 2, pp. 39–48, Apr. 2018, doi: 10.1080/17452759.2017.1351201.

[9] I. Ohno, "Free vibration of a rectangular parallelepiped crystal and its application to determination of elastic constants of orthorhombic crystals," *J. Phys. Earth*, vol. 24, no. 4, 1976, Accessed: Jan. 25, 2020. [Online]. Available: https://www.jstage.jst.go.jp/article/jpe1952/24/4/24_4_355/_pdf/-char/en.

[10] H. H. Demarest, "Cube-Resonance Method to Determine the Elastic Constants of Solids," *J. Acoust. Soc. Am.*, vol. 49, no. 3B, pp. 768–775, Mar. 1971, doi: 10.1121/1.1912415.

[11] H. Li *et al.*, "Characterizing elastic and piezoelectric constants of piezoelectric materials from one sample using resonant ultrasound spectroscopy," *J. Mater. Sci.*, vol. 54, no. 9, pp. 6786–6798, May 2019, doi: 10.1007/s10853-019-03386-y.

[12] H. Ogi, K. Sato, T. Asada, and M. Hirao, "Complete mode identification for resonance ultrasound spectroscopy," *J. Acoust. Soc. Am.*, vol. 112, no. 6, pp. 2553–2557, 2002, doi: 10.1121/1.1512700.

[13] G. Liu and J. D. Maynard, "Measuring elastic constants of arbitrarily shaped samples using resonant ultrasound spectroscopy," *J. Acoust. Soc. Am.*, vol. 131, no. 3, pp. 2068–2078, Mar. 2012, doi: 10.1121/1.3677259.

[14] Z. Chen *et al.*, "Data Fusion Method and Probabilistic Pairing Approach in Elastic Constants Measurement by Resonance Ultrasound Spectroscopy," *IEEE Trans. Instrum. Meas.*, vol. 69, no. 6, pp. 2948–2958, 2019, doi: 10.1109/TIM.2019.2925409.

[15] Q. Zhang, F. Fan, R. Wang, H. Niu, and P. Laugier, "A resonant frequency retrieving method for low Q-factor materials based on resonant ultrasound spectroscopy," *Ultrasonics*, vol. 99, no. 10597, 2019, doi: 10.1016/j.ultras.2019.105971.

[16] H. Niu *et al.*, "Elastic properties measurement of human enamel based on resonant ultrasound spectroscopy," *J. Mech. Behav. Biomed. Mater.*, vol. 89, pp. 48–53, Jan. 2019, doi: 10.1016/j.jmbbm.2018.09.014.

[17] R. Wang, F. Fan, Q. Zhang, X. Li, H. Niu, and P. Laugier, “Elastic constants identification of irregular hard biological tissue materials using FEM-based resonant ultrasound spectroscopy,” *J. Mech. Behav. Biomed. Mater.*, vol. 96, pp. 20–26, 2019, doi: 10.1016/j.jmbbm.2019.04.031.
[18] R. Longo, D. Laux, S. Pagano, T. Delaunay, E. Le Clézio, and O. Arnould, “Elastic characterization of wood by Resonant Ultrasound Spectroscopy (RUS): a comprehensive study,” *Wood Sci. Technol.*, vol. 52, no. 2, pp. 383–402, Mar. 2018, doi: 10.1007/s00226-017-0980-z.
[19] A. Karunarathne, K. S. Jodha, G. Priyadarshan, J. A. Griggs, and J. R. Gladden, “Low pressure dependent elasticity of porous ceramics,” *J. Am. Ceram. Soc.*, vol. 103, no. 2, pp. 1312–1320, 2020, doi: 10.1111/jace.16751.
[20] W. Peng *et al.*, “Lattice hardening due to vacancy diffusion in (GeTe)mSb2Te3 alloys,” *J. Appl. Phys.*, vol. 126, no. 5, Aug. 2019, doi: 10.1063/1.5108659.
[21] G. Singh *et al.*, “Elastic moduli reduction in SiC-SiC tubular specimen after high heat flux neutron irradiation measured by resonant ultrasound spectroscopy,” *J. Nucl. Mater.*, vol. 523, pp. 391–401, Sep. 2019, doi: 10.1016/j.jnucmat.2019.06.026.
[22] U. Carvajal-Nunez, T. A. Saleh, T. J. White, B. Maiorov, and A. T. Nelson, “Determination of elastic properties of polycrystalline U3Si2 using resonant ultrasound spectroscopy,” *J. Nucl. Mater.*, vol. 498, pp. 438–444, 2018, doi: 10.1016/j.jnucmat.2017.11.008.
[23] S. Ghosh *et al.*, “Thermodynamic Evidence for a Two-Component Superconducting Order Parameter in Sr$_2$RuO$_4$,” *ArXiv200206130 Cond-Mat*, Feb. 2020, Accessed: Feb. 22, 2020. [Online]. Available: http://arxiv.org/abs/2002.06130.
[24] C. Hirschle, J. Schreuer, S. Ganschow, and I. Schulze-Jonack, “Thermoelastic properties of rare-earth scandates $SmScO_3$, $TbScO_3$ and $DyScO_3$,” *J. Appl. Phys.*, vol. 126, no. 16, p. 165103, Oct. 2019, doi: 10.1063/1.5108584.
[25] M. Zhuang, L. Tang, R. Zhu, and G. Xu, “Nondestructive evaluation of homogeneity of Mn-doped 0.23Pb(In1/2Nb1/2)O3–0.48Pb(Mg1/3Nb2/3)O3–0.29PbTiO3 single crystals via resonant ultrasound spectroscopy,” *J. Phys. Appl. Phys.*, vol. 53, no. 3, p. 035303, Nov. 2019, doi: 10.1088/1361-6463/ab4e67.
[26] M. I. Latypov *et al.*, “Computational homogenization for multiscale forward modeling of resonant ultrasound spectroscopy of heterogeneous materials,” *Mater. Charact.*, vol. 158, p. 109945, Dec. 2019, doi: 10.1016/j.matchar.2019.109945.
[27] J. Plesek, R. Kolman, and M. Landa, “Using finite element method for the determination of elastic moduli by resonant ultrasound spectroscopy,” *J. Acoust. Soc. Am.*, vol. 116, no. 1, pp. 282–287, Jul. 2004, doi: 10.1121/1.1760800.
[28] K. Flynn and M. Radovic, “Evaluation of defects in materials using resonant ultrasound spectroscopy,” *J. Mater. Sci.*, vol. 46, no. 8, pp. 2548–2556, 2011, doi: 10.1007/s10853-010-5107-y.
[29] I. Solodov, J. Bai, and G. Busse, “Resonant ultrasound spectroscopy of defects: Case study of flat-bottomed holes,” *J. Appl. Phys.*, vol. 113, no. 22, 2013, doi: 10.1063/1.4810926.
[30] F. H. Kim, S. P. Moylan, E. J. Garboczi, and J. A. Slotwinski, “Investigation of pore structure in cobalt chrome additively manufactured parts using X-ray computed tomography and three-dimensional image analysis | Elsevier Enhanced Reader,” *Addit. Manuf.*, vol. 17, pp. 23–38, Oct. 2017, doi: 10.1016/j.addma.2017.06.011.
[31] Y. Ibrahim, Z. Li, C. M. Davies, C. Maharaj, J. P. Dear, and P. A. Hooper, “Acoustic resonance testing of additive manufactured lattice structures,” *Addit. Manuf.*, vol. 24, no. July, pp. 566–576, 2018, doi: 10.1016/j.addma.2018.10.034.
[32] S.-I. Park, D. W. Rosen, S. Choi, and C. E. Duty, “Effective mechanical properties of lattice material fabricated by material extrusion additive manufacturing,” *Addit. Manuf.*, vol. 1–4, pp. 12–23, Oct. 2014, doi: 10.1016/j.addma.2014.07.002.
[33] E. Garlea *et al.*, “Variation of elastic mechanical properties with texture , porosity , and defect characteristics in laser powder bed fusion 316L stainless steel,” *Mater. Sci. Eng. A*, vol. 763, no. June, p. 138032, 2019, doi: 10.1016/j.msea.2019.138032.

[34] Z. Chen, X. Wu, D. Tomus, and C. H. J. Davies, “Surface roughness of Selective Laser Melted Ti-6Al-4V alloy components,” *Addit. Manuf.*, vol. 21, pp. 91–103, May 2018, doi: 10.1016/j.addma.2018.02.009.
[35] B. K. Foster, E. W. Reutzel, A. R. Nassar, B. T. Hall, S. W. Brown, and C. J. Dickman, “Optical, layerwise monitoring of powder bed fusion,” presented at the Solid freeform fabrication symposium, Austin, Texas, Aug. 2015, Accessed: Feb. 08, 2020. [Online]. Available: https://sffsymposium.engr.utexas.edu/sites/default/files/2015/2015-24-Foster.pdf.
[36] C. Meier, R. Weissbach, J. Weinberg, W. A. Wall, and A. J. Hart, “Critical influences of particle size and adhesion on the powder layer uniformity in metal additive manufacturing,” *J. Mater. Process. Technol.*, vol. 266, pp. 484–501, Apr. 2019, doi: 10.1016/j.jmatprotec.2018.10.037.
[37] M. M. (ORCID:0000000330626234) Francois *et al.*, “Modeling of additive manufacturing processes for metals: Challenges and opportunities,” *Curr. Opin. Solid State Mater. Sci.*, vol. 21, no. 4, Jan. 2017, doi: 10.1016/j.cossms.2016.12.001.
[38] J. C. Steuben, A. P. Iliopoulos, and J. G. Michopoulos, “Discrete element modeling of particle-based additive manufacturing processes,” *Comput. Methods Appl. Mech. Eng.*, vol. 305, pp. 537–561, Jun. 2016, doi: 10.1016/j.cma.2016.02.023.
[39] M. A. Todd, J. Hunt, and I. Todd, “Investigation into using resonant frequency measurements to predict the mechanical properties of Ti-6Al-4V manufactured by selective laser melting,” *Sci. Rep.*, vol. 9, no. 9278, 2019, doi: 10.1038/s41598-019-45696-w.
[40] J. D. Maynard, “Resonant ultrasound spectroscopy,” *Med. Imaging 1998 Ultrason. Transducer Eng.*, vol. 3341, no. May 1998, pp. 132–142, 1998, doi: 10.1117/12.307994.
[41] R. G. Leisure and F. A. Willis, “Resonant ultrasound spectroscopy,” *Phys. Today*, vol. 9, no. 28, 1997, doi: 10.1063/1.881483.
[42] F. R. Drymiotis, “Resonant ultrasound spectroscopy: overview and applications,” *Int. J. Mod. Phys. B*, vol. 24, no. 09, pp. 1047–1065, Apr. 2010, doi: 10.1142/S0217979210055561.
[43] A. Migliori *et al.*, “Resonant ultrasound spectroscopic techniques for measurement of the elastic moduli of solids,” *Phys. B Condens. Matter*, vol. 183, no. 1–2, pp. 1–24, Jan. 1993, doi: 10.1016/0921-4526(93)90048-B.
[44] W. H. Press, S. A. Teukolsky, W. T. Vetterling, and B. P. Flannery, *Numerical Recipes*, Third. Cambridge University Press, 1985.
[45] “COMSOL Multiphysics Modeling Software,” *COMSOL Multiphysics Modeling Software*. .
[46] “Cobalt Chrome MP1.” Accessed: Jan. 06, 2020. [Online]. Available: www.eos.info.
[47] “Cobalt Chrome Molybdenum Bar Stock - Chrome Moly Steel - ASTM F1537 Alloy 1.” https://www.upmet.com/products/cobalt/cobalt-chrome-moly (accessed Jan. 06, 2020).
[48] “Alamo Creek Engineering,” *Alamo Creek Engineering*. http://rusalamocreek.com/.
[49] F. F. Balakirev, S. M. Ennaceur, R. J. Migliori, B. Maiorov, and A. Migliori, “Resonant ultrasound spectroscopy: The essential toolbox,” *Rev. Sci. Instrum.*, vol. 90, no. 12, p. 121401, Dec. 2019, doi: 10.1063/1.5123165.
[50] H. Sakoe, “Dynamic Programming Algorithm Optimization for Spoken Word Recognition.”
[51] K. K. Paliwal, A. Agarwal, and S. S. Sinha, “A Modification over Sakoe and Chiba’s dynamic time warping algorithm for isolated word recognition,” in *IEEE International Conference on ICASSP*, 1982, vol. 7, pp. 1259–1261.
[52] A. Gómez González, J. Rodríguez, X. Sagartzazu, A. Schumacher, and I. Isasa, “Multiple Coherence Method in Time Domain for the Analysis of the Transmission Paths of Noise and Vibrations with Non-Stationary Signals,” in *Proceedings of the 2010 International Conference of Noise and Vibration Engineering*, 2010, pp. 3927–3941.
[53] S. M. Kay, *Modern Spectral Estimation*. Englewood Cliffs, NJ: Prentice-Hall, 1988.
[54] L. R. Rabiner and B. Gold, *Theory and Application of Digital Signal Processing*. Englewood Cliffs, NJ: Prentice-Hall, 1975.
[55] P. Stocia and R. Moses, *Spectral Analysis of Signals*. Upper Saddle River, NJ: Prentice-Hall, 2005.

[56] P. D. Welch, "The Use of Fast Fourier Transform for the Estimation of Power Spectra: A Method Based on Time Averaging Over Short, Modified Periodograms," *IEEE® Trans. Audio Electroacoustics*, vol. AU-15, 1967.
[57] "Hypothesis Tests," *MathWorks*. https://www.mathworks.com/help/stats/hypothesis-tests-1.html?s_tid=CRUX_lftnav.
[58] A. V. Oppenheim, *Signals, Systems, and Inference*. Boston: Pearson.
[59] S. Arabnejad, R. Burnett Johnston, J. A. Pura, B. Singh, M. Tanzer, and D. Pasini, "High-strength porous biomaterials for bone replacement: A strategy to assess the interplay between cell morphology, mechanical properties, bone ingrowth and manufacturing constraints," *Acta Biomater.*, vol. 30, pp. 345–356, Jan. 2016, doi: 10.1016/j.actbio.2015.10.048.
[60] L. Zhang *et al.*, "Energy absorption characteristics of metallic triply periodic minimal surface sheet structures under compressive loading," *Addit. Manuf.*, vol. 23, pp. 505–515, Oct. 2018, doi: 10.1016/j.addma.2018.08.007.
[61] A. Ataee, Y. Li, D. Fraser, G. Song, and C. Wen, "Anisotropic Ti-6Al-4V gyroid scaffolds manufactured by electron beam melting (EBM) for bone implant applications," *Mater. Des.*, vol. 137, pp. 345–354, Jan. 2018, doi: 10.1016/j.matdes.2017.10.040.
[62] B. Lozanovski *et al.*, "Computational modelling of strut defects in SLM manufactured lattice structures," *Mater. Des.*, vol. 171, p. 107671, Jun. 2019, doi: 10.1016/j.matdes.2019.107671.
[63] A. Cuadrado, A. Yánez, O. Martel, S. Deviaene, and D. Monopoli, "Influence of load orientation and of types of loads on the mechanical properties of porous Ti6Al4V biomaterials," *Mater. Des.*, vol. 135, pp. 309–318, Dec. 2017, doi: 10.1016/j.matdes.2017.09.045.
[64] T. Tancogne-Dejean, A. B. Spierings, and D. Mohr, "Additively-manufactured metallic micro-lattice materials for high specific energy absorption under static and dynamic loading," *Acta Mater.*, vol. 116, pp. 14–28, Sep. 2016, doi: 10.1016/j.actamat.2016.05.054.
[65] S. L. Sing, W. Y. Yeong, F. E. Wiria, and B. Y. Tay, "Characterization of Titanium Lattice Structures Fabricated by Selective Laser Melting Using an Adapted Compressive Test Method," *Exp. Mech.*, vol. 56, no. 5, pp. 735–748, Jun. 2016, doi: 10.1007/s11340-015-0117-y.
[66] S. Y. Choy, C.-N. Sun, K. F. Leong, and J. Wei, "Compressive properties of functionally graded lattice structures manufactured by selective laser melting," *Mater. Des.*, vol. 131, pp. 112–120, Oct. 2017, doi: 10.1016/j.matdes.2017.06.006.
[67] D. Melancon, Z. S. Bagheri, R. B. Johnston, L. Liu, M. Tanzer, and D. Pasini, "Mechanical characterization of structurally porous biomaterials built via additive manufacturing: experiments, predictive models, and design maps for load-bearing bone replacement implants," *Acta Biomater.*, vol. 63, pp. 350–368, Nov. 2017, doi: 10.1016/j.actbio.2017.09.013.
[68] L. Liu, P. Kamm, F. García-Moreno, J. Banhart, and D. Pasini, "Elastic and failure response of imperfect three-dimensional metallic lattices: the role of geometric defects induced by Selective Laser Melting," *J. Mech. Phys. Solids*, vol. 107, pp. 160–184, Oct. 2017, doi: 10.1016/j.jmps.2017.07.003.
[69] R. Gümrük, R. A. W. Mines, and S. Karadeniz, "Static mechanical behaviours of stainless steel micro-lattice structures under different loading conditions," *Mater. Sci. Eng. A*, vol. 586, pp. 392–406, Dec. 2013, doi: 10.1016/j.msea.2013.07.070.
[70] S. Li, H. Hassanin, M. M. Attallah, N. J. E. Adkins, and K. Essa, "The development of TiNi-based negative Poisson's ratio structure using selective laser melting," *Acta Mater.*, vol. 105, pp. 75–83, Feb. 2016, doi: 10.1016/j.actamat.2015.12.017.
[71] Z. Dong, Y. Liu, W. Li, and J. Liang, "Orientation dependency for microstructure, geometric accuracy and mechanical properties of selective laser melting AlSi10Mg lattices," *J. Alloys Compd.*, vol. 791, pp. 490–500, Jun. 2019, doi: 10.1016/j.jallcom.2019.03.344.
[72] J. A. Slotwinski, E. J. Garboczi, and K. M. Hebenstreit, "Porosity Measurements and Analysis for Metal Additive Manufacturing Process Control," *J. Res. Natl. Inst. Stand. Technol.*, vol. 119, pp. 494–528, Sep. 2014, doi: 10.6028/jres.119.019.

[73] A. Takaichi *et al.*, “Microstructures and mechanical properties of Co–29Cr–6Mo alloy fabricated by selective laser melting process for dental applications,” *J. Mech. Behav. Biomed. Mater.*, vol. 21, pp. 67–76, May 2013, doi: 10.1016/j.jmbbm.2013.01.021.
[74] H. L. Wei, J. Mazumder, and T. DebRoy, “Evolution of solidification texture during additive manufacturing,” *Sci. Rep.*, vol. 5, no. 1, Art. no. 1, Nov. 2015, doi: 10.1038/srep16446.
[75] P. Hanzl, M. Zetek, T. Bakša, and T. Kroupa, “The Influence of Processing Parameters on the Mechanical Properties of SLM Parts,” *Procedia Eng.*, vol. 100, pp. 1405–1413, 2015, doi: 10.1016/j.proeng.2015.01.510.
[76] R. Goodall *et al.*, “The effects of defects and damage in the mechanical behavior of Ti6Al4V lattices,” *Front. Mater.*, vol. 6, Jul. 2019, Accessed: Jun. 08, 2020. [Online]. Available: http://eprints.whiterose.ac.uk/148396/.
[77] C. Song, Y. Yang, Y. Wang, D. Wang, and J. Yu, “Research on rapid manufacturing of CoCrMo alloy femoral component based on selective laser melting,” *Int. J. Adv. Manuf. Technol.*, vol. 75, no. 1–4, pp. 445–453, Oct. 2014, doi: 10.1007/s00170-014-6150-7.
[78] N. Guo, P. Cawley, and D. Hitchings, “The finite element analysis of the vibration characteristics of piezoelectric discs,” *J. Sound Vib.*, vol. 159, no. 1, pp. 115–138, Nov. 1992, doi: 10.1016/0022-460X(92)90454-6.
[79] H. A. Kunkel, S. Locke, and B. Pikeroen, “Finite-Element Analysis of Vibrational Modes in Piezoelectric Ceramic Disks,” *IEEE Trans. Ultrason. Ferroelectr. Freq. Control*, vol. 37, no. 4, pp. 316–328, 1990, doi: 10.1109/58.56492.
[80] R. Lerch, “Simulation of Piezoelectric Devices by Two- and Three-Dimensional Finite Elements,” *IEEE Trans. Ultrason. Ferroelectr. Freq. Control*, vol. 37, no. 3, pp. 233–247, 1990, doi: 10.1109/58.55314.
[81] N. Pérez, F. Buiochi, M. A. Brizzotti Andrade, and J. C. Adamowski, “Numerical Characterization of Piezoceramics Using Resonance Curves,” *Materials*, vol. 9, no. 2, Art. no. 2, Feb. 2016, doi: 10.3390/ma9020071.